

**DESIGN AND ANALYSIS OF SINGLE MODE POLYMER  
PHOTONIC CRYSTAL FIBER FOR SUPERCONTINUUM  
GENERATION**

A K M AHOSAN HABIB

Roll No.: 1014062203 P

MASTER OF SCIENCE IN ELECTRICAL AND ELECTRONIC ENGINEERING





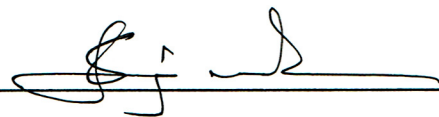

Department of Electrical and Electronic Engineering

BANGLADESH UNIVERSITY OF ENGINEERING AND TECHNOLOGY

February 2020

The thesis titled “DESIGN AND ANALYSIS OF SINGLE MODE POLYMER PHOTONIC CRYSTAL FIBER FOR SUPERCONTINUUM GENERATION” submitted by A K M Ahsan Habib, Roll No.: 1014062203 P, Session: October, 2014, has been accepted as satisfactory in partial fulfillment of the requirements for the degree of MASTER OF SCIENCE IN ELECTRICAL AND ELECTRONIC ENGINEERING on February 26, 2020.

### BOARD OF EXAMINERS

1.   
\_\_\_\_\_
- Dr. Md. Shah Alam  
Professor  
Department of Electrical and Electronic Engineering  
Bangladesh University of Engineering and Technology  
Dhaka.  
Chairman  
(Supervisor)
2.   
\_\_\_\_\_
- Dr. Md. Shafiqul Islam  
Professor and Head  
Department of Electrical and Electronic Engineering  
Bangladesh University of Engineering and Technology  
Dhaka.  
Member  
(Ex-officio)
3.   
\_\_\_\_\_
- Dr. Satya Prasad Majumder  
Professor  
Department of Electrical and Electronic Engineering  
Bangladesh University of Engineering and Technology  
Dhaka.  
Member
4.   
\_\_\_\_\_
- Dr. A.K.M Akther Hossain  
Professor  
Department of Physics  
Bangladesh University of Engineering and Technology  
Dhaka.  
Member  
(External)

## **DECLARATION**

It is hereby declared that this thesis or any part of it has not been submitted elsewhere for the award of any degree or diploma and that all sources are acknowledged.

Signature

---

A K M Ahsan Habib  
Roll No.: 1014062203 P

## **Dedication**

*To my Wife*

## **Acknowledgement**

First of all, I would like to thank Allah, the almighty, for giving me the ability to complete this thesis work.

I would like to express my sincere gratitude to my supervisor, Dr. Md. Shah Alam. This thesis would not have been completed without his support and guidance. His constant encouragement gave me the confidence to carry out my work.

I would like to thank all my teachers. They gave the knowledge and directions that have helped me throughout my life. I express my gratitude to my teachers from Bangladesh University of Engineering and Technology. The knowledge I learned from the classes in my M.Sc. level were essential for this thesis.

I want to thank my friends for providing me support and encouragement. Their suggestions helped me in countless ways.

Last but not the least; I would like to thank my parents and family members. Their optimism and encouragement have allowed me to overcome any obstacle that I faced. Their unconditional support made it possible for me to complete this thesis.

## ABSTRACT

The main aim of this thesis is to design a polymer photonic crystal fiber for supercontinuum generation. A new hybrid polymer PCF having triangular lattice structure and cyclic olefin copolymer Topas as background material is proposed due to its broad transparency window and mature fabrication technology. We report a non-linear hybrid polymer PCF with integrated silica glass layers of few nanometers at the outer surface of the air holes. This air-silica-polymer combination makes the PCF highly nonlinear i.e. exhibits an extremely high nonlinear parameter. By tailoring zero-dispersion wavelength supercontinuum obtained in the proposed photonic crystal fiber in the anomalous dispersion regime. We simulated the evolution of the transverse intensity distribution, the nonlinear parameter  $\gamma$ , and the group velocity dispersion (GVD) of the fiber. Using a split-step Fourier method, the nonlinear Schrödinger equation is solved to simulate the spectral and temporal properties of the supercontinuum. Simulation shows that spectrum generated by this new nonlinear fiber ranges from 500 nm to more than 2166 nm which will be useful in the field of high performance optical coherence tomography (OCT) imaging systems, where a broad-band light source with high penetration depth and high degree of coherence with sufficient brightness are required for spatial resolution. The effects on supercontinuum spectra by varying peak power, pulse duration, length of PCF, higher order dispersion parameters are studied. The findings are with the increase of input power supercontinuum becomes broader, supercontinuum becomes broader as the pulse duration increases and the longer the fiber length the broader the supercontinuum generated. Besides, the effect of higher order dispersion parameters up to 12<sup>th</sup> order is analyzed.

## CONTENTS

|  |            |
|--|------------|
| <b>LIST OF TABLES.....</b>                                   | <b>x</b>   |
| <b>LIST OF FIGURES.....</b>                                  | <b>x</b>   |
| <b>LIST OF ABBRAVIATIONS.....</b>                            | <b>xiv</b> |
| <b>LIST OF SYMBOLS.....</b>                                  | <b>xvi</b> |
| <br>   |            |
| <b>1 INTRODUCTION.....</b>                                   | <b>1</b>   |
| 1.1 Guidance Mechanism in Index-Guided PCF                   | 1          |
| 1.2 Photonic Band-gap Fiber                                  | 2          |
| 1.3 Guidance Mechanism in Photonic Band-gap Fiber            | 3          |
| 1.4 Properties and Applications of Photonic Crystal Fiber    | 4          |
| 1.4.1 Solid Core Fibers                                      | 4          |
| 1.4.2 Highly Birefringent Fibers                             | 5          |
| 1.4.3 Dispersion Tailoring                                   | 5          |
| 1.4.4 Ultrahigh Non-linearities                              | 6          |
| 1.4.5 Large Mode Area Fibers                                 | 6          |
| 1.4.6 Hollow Core Fibers                                     | 7          |
| 1.5 Fabrication Technology of PCFs                           | 7          |
| 1.5.1 Stack and Draw (SaD) Technique                         | 7          |
| 1.5.2 Extrusion Fabrication Process                          | 8          |
| 1.5.3 Filling Technology                                     | 9          |
| 1.5.4 Sol-gel Technique for Irregular Shaped PCF Fabrication | 9          |
| 1.6 Literature Review  | 11         |
| 1.7 Objectives of the Thesis                                 | 13         |
| 1.8 Organization of the Thesis                               | 13         |
| <br>   |            |
| <b>2 POLYMER PHOTONIC CRYSTAL FIBER.....</b>                 | <b>15</b>  |
| 2.1 Terahertz Radiation: Opportunities and Development       | 15         |
| 2.2 Photonic Crystal Fiber (PCF) as THz Waveguide            | 16         |

|          |  |           |
|----------|--|-----------|
| 2.3      | Materials for THz Transmission                       | 17        |
| 2.4      | Fabrication of Polymer Microstructured Fibers        | 18        |
| 2.5      | THz Fiber Characteristics                            | 19        |
| 2.5.1    | Computation of Fundamental Space-filling Mode (FSM)  | 19        |
| 2.5.2    | Dispersion   | 20        |
| 2.5.3    | Endlessly Single-mode Fiber (ESMF)                   | 22        |
| 2.5.4    | Effective Mode Area                                  | 23        |
| 2.5.5    | Non-linearity  | 24        |
| 2.5.6    | Bending Loss   | 24        |
| 2.5.7    | Power Fraction                                       | 25        |
| <b>3</b> | <b>MODAL ANALYSIS OF POLYMER PCF.....</b>            | <b>26</b> |
| 3.1      | Structural Details                                   | 26        |
| 3.2      | Methods Adopted                                      | 26        |
| 3.3      | Mode Details and Properties                          | 27        |
| 3.3.1    | Field Distribution of Core Mode                      | 27        |
| 3.3.2    | Fundamental Space Filling mode (FSM)                 | 29        |
| 3.3.3    | Structural Dependence of Modal Properties            | 30        |
| <b>4</b> | <b>THEORIES OF SUPERCONTINUUM GENERATION.....</b>    | <b>39</b> |
| 4.1      | Conventional Light Source and Supercontinuum Source  | 40        |
| 4.2      | Applications of Supercontinuum Source                | 40        |
| 4.3      | Physics of Spectral Broadening                       | 42        |
| 4.4      | Mechanisms Responsible for Supercontinuum Generation | 43        |
| 4.4.1    | Self-Phase Modulation                                | 43        |
| 4.4.2    | Soliton Formation                                    | 44        |
| 4.4.2.1  | Fundamental Soliton                                  | 44        |
| 4.4.2.2  | Higher-Order Soliton                                 | 45        |
| 4.4.3    | Stimulated Raman Scattering                          | 46        |
| 4.4.4    | Four Wave-mixing (FWM)                               | 46        |
| 4.4.5    | Higher Order Dispersion Parameter                    | 47        |



|          |  |           |
|----------|--|-----------|
| 4.4.6    | Nonlinearity Coefficient   | 50        |
| 4.5      | Numerical Model of Supercontinuum  | 51        |
| 4.6      | Solution of Generalized Nonlinear Schrodinger Equation (GNLSE) Using Split Step Fourier Method | 54        |
| <b>5</b> | <b>SUPERCONTINUUM GENERATION IN HYBRID POLYMER PCF.....</b>                                    | <b>57</b> |
| 5.1      | Design of Hybrid Polymer PCF   | 57        |
| 5.2      | Results and Discussions  | 58        |
| <b>6</b> | <b>CONCLUSIONS.....</b>  | <b>77</b> |
| 6.1      | Conclusion of the Work   | 77        |
| 6.2      | Future Scope of Work   | 78        |
|          | <b>REFERENCES.....</b>   | <b>79</b> |

## LIST OF TABLES

|           |   |    |
|-----------|---|----|
| Table 2.1 | Boundary conditions used to compute $n_{FSM}$   | 20 |
| Table 4.1 | Parameters of Silica PCF  | 52 |
| Table 4.2 | Main processes affecting supercontinuum generation with short and long input pulses in the normal and anomalous GVD regimes | 53 |
| Table 5.1 | Simulation parameters for proposed hybrid polymer PCF   | 65 |
| Table 5.2 | Higher order dispersion coefficients for proposed hybrid polymer PCF at pumping wavelength, $\lambda=1100$ nm               | 66 |
| Table 5.3 | Summary of Simulation Results   | 71 |
| Table 5.4 | Summary of effects of higher order dispersion coefficients on pulse broadening  | 76 |

## LIST OF FIGURES

|          |  |    |
|----------|--|----|
| Fig. 1.1 | Triangular lattice solid-core PCF  | 2  |
| Fig. 1.2 | Photonic band-gap fiber  | 3  |
| Fig. 1.3 | Cross-section of first photonic band-gap PCF with honey-comb lattice structure   | 4  |
| Fig. 1.4 | (a) the cross-section and (b) the core region of a highly birefringent triangular PCF  | 5  |
| Fig. 1.5 | (a) Sketch of extrusion process and (b) extrusion die concepts with equal and different size feed holes for a target preform structure   | 8  |
| Fig. 1.6 | SEM image of a germanium-filled endlessly single-mode PCF  | 9  |
| Fig. 1.7 | Cross-sectional images of sol-gel derived microstructured fibers. a) endlessly single moded design, b) high delta, highly nonlinear fiber, c) dual core structure and d) circular core microstructured fiber | 11 |
| Fig. 1.8 | Schematic representation of sol gel fabrication technique  | 11 |
| Fig. 2.1 | Elementary piece of cladding used to compute $n_{FSM}$   | 20 |

|           |   |    |
|-----------|---|----|
| Fig. 3.1  | Cross sectional view THz PCF  | 26 |
| Fig. 3.2  | Electric field distribution of the fundamental mode of the THz PCF for $d/\Lambda = 0.4$ , (a) for 1 THz (b) for 0.6 THz                | 27 |
| Fig. 3.3  | Contour plot of the electric field pattern of the fundamental mode of the THz PCF for $d/\Lambda = 0.4$ , (a) for 1 THz (b) for 0.6 THz | 27 |
| Fig. 3.4  | Contour plot of the electric field pattern of the fundamental mode of the THz PCF for $d/\Lambda = 0.8$ at 10 THz                       | 28 |
| Fig. 3.5  | Transverse electric field vector distributions of fundamental of the THz PCF for $d/\Lambda = 0.4$ , (a) for 1 THz (b) 0.6 THz          | 28 |
| Fig. 3.6  | Transverse magnetic field vector distributions of fundamental of the THz PCF for $d/\Lambda = 0.4$ , (a) for 1 THz (b) 0.6 THz          | 29 |
| Fig. 3.7  | Element division of the elementary piece  | 29 |
| Fig. 3.8  | Simulated normalized electric field for fundamental space-filling mode at 2 THz and filling factor, $f = 0.55$ .                        | 30 |
| Fig. 3.9  | Effective mode indices as a function of frequency for filling factor, $f = 0.4$ .   | 30 |
| Fig. 3.10 | $n_{eff}$ and $n_{FSM}$ for different filling factors, $f$  | 31 |
| Fig. 3.11 | Effective index of the Fundamental space filling mode for the THz PCF with different filling factors, $f$                               | 31 |
| Fig. 3.12 | Dispersion as a function of frequency for various filling factors, $f$  | 32 |
| Fig. 3.13 | Dispersion profile for the THz PCF with $\Lambda = 500 \mu\text{m}$ and filling factor, $f = 0.4$                                       | 32 |
| Fig. 3.14 | Effective Area as a function of frequency for different filling factors, $f$  | 33 |
| Fig. 3.15 | Effective area as a function of wavelength for different filling factors, $f$   | 33 |
| Fig. 3.16 | Nonlinearity parameter as a function of frequency for various filling factors, $f$  | 34 |
| Fig. 3.17 | Bending Loss as a function of frequency for filling factor, $f = 0.55$  | 35 |
| Fig. 3.18 | Bending loss as a function of bending radius for different filling factors, $f$ when frequency is restricted to 1 THz                   | 35 |
| Fig. 3.19 | Normalized V parameters of the THz PCF for various filling factors $f$  | 36 |
| Fig. 3.20 | Power fraction in cladding air-holes as a function of frequency for different filling factors, $f$                                      | 37 |

|           |   |    |
|-----------|---|----|
| Fig. 3.21 | Power fraction in HDPE as a function of frequency for various filling factors $f$   | 37 |
| Fig. 3.22 | Power fraction in both HDPE, and cladding air-holes as a function of frequency for various filling factors $f$  | 38 |
| Fig. 5.1  | (a) Cross sectional view of hybrid polymer PCF and (b) A single air hole with silica glass layer  | 58 |
| Fig. 5.2  | Dispersion as a function of wavelength for different filling factors, $f$   | 59 |
| Fig. 5.3  | Electric filed distributions at 1100 nm when filling factor (a) 0.5 (b) 0.6 (c) 0.7   | 59 |
| Fig. 5.4  | Effective area as a function of wavelength for different filling factors, $f$   | 60 |
| Fig. 5.5  | Nonlinearity parameter as a function of wavelength for different filling factors, $f$   | 60 |
| Fig.5.6   | 2 <sup>nd</sup> order dispersion (GVD) parameter  | 61 |
| Fig.5.7   | 3 <sup>rd</sup> order dispersion parameter  | 61 |
| Fig.5.8   | 4 <sup>th</sup> order dispersion parameter  | 62 |
| Fig.5.9   | 5 <sup>th</sup> order dispersion parameter  | 62 |
| Fig.5.10  | 6 <sup>th</sup> order dispersion parameter  | 62 |
| Fig.5.11  | 7 <sup>th</sup> order dispersion parameter  | 63 |
| Fig.5.12  | 8 <sup>th</sup> order dispersion parameter  | 63 |
| Fig.5.13  | 9 <sup>th</sup> order dispersion parameter  | 63 |
| Fig.5.14  | 10 <sup>th</sup> order dispersion parameter   | 64 |
| Fig.5.15  | 11 <sup>th</sup> order dispersion parameter.  | 64 |
| Fig.5.16  | 12 <sup>th</sup> order dispersion parameter.  | 64 |
| Fig.5.17  | Spectral and temporal broadening in 15 cm long HP-PCF with $T_{FWHM}$ as 28.4 fs, and peak power (a) 1 kW (b) 5 kW (c) 10 kW (d) 20 kW                          | 67 |
| Fig.5.18  | Spectral and temporal broadening in 15 cm long PCF using peak power as 10 kW and (a) $T_{FWHM} = 50$ fs (b) $T_{FWHM} = 100$ fs (c) 150 fs                      | 68 |
| Fig.5.19  | Spectral and temporal broadening using peak power as 10 kW, $T_{FWHM}$ as 28.4 fs and (a) fiber length = 5 cm (b) fiber length = 10 cm (c) fiber length = 30 cm | 69 |

- Fig.5.20 Spectral and temporal broadening using peak power as 1 kW,  $T_{FWHM}$  as 28.4 fs, fiber length 5 cm and dispersion coefficients including (a) 2<sup>nd</sup> and 3<sup>rd</sup> order (b) 2<sup>nd</sup> order to 6<sup>th</sup> order (c) 2<sup>nd</sup> order to 12<sup>th</sup> order. 72
- Fig.5.21 Spectral and temporal broadening using peak power as 10 kW,  $T_{FWHM}$  as 28.4 fs, fiber length 5 cm and dispersion coefficients including (a) 2<sup>nd</sup> and 3<sup>rd</sup> order (b) 2<sup>nd</sup> order to 6<sup>th</sup> order (c) 2<sup>nd</sup> order to 12<sup>th</sup> order. 73
- Fig.5.22 Spectral and temporal broadening using peak power as 1 kW,  $T_{FWHM}$  as 28.4 fs, fiber length 15 cm and dispersion coefficients including (a) 2<sup>nd</sup> and 3<sup>rd</sup> order (b) 2<sup>nd</sup> order to 6<sup>th</sup> order (c) 2<sup>nd</sup> order to 12<sup>th</sup> order. 74
- Fig.5.23 Spectral and temporal broadening using peak power as 10 kW,  $T_{FWHM}$  as 28.4 fs, fiber length 15 cm and dispersion coefficients including (a) 2<sup>nd</sup> and 3<sup>rd</sup> order (b) 2<sup>nd</sup> order to 6<sup>th</sup> order (c) 2<sup>nd</sup> order to 12<sup>th</sup> order. 75

## LIST OF ABBRAVIATIONS

|       |   |  |
|-------|---|--|
| CW    | : | Continuous Wave                            |
| ESMF  | : | Endlessly Single-Mode fiber                |
| FEM   | : | Finite Element Method                      |
| FSM   | : | Fundamental Space Filling Mode             |
| FWM   | : | Four Wave Mixing                           |
| FWHM  | : | Full Width Half Maximum                    |
| GNLS  | : | Generalized Nonlinear Schrödinger Equation |
| GVD   | : | Group Velocity Dispersion                  |
| HDPE  | : | High Density Polyethylene                  |
| HOD   | : | Higher Order Dispersion                    |
| H-PCF | : | Hybrid Photonic Crystal Fiber              |
| IG    | : | Index Guided                               |
| LMA   | : | Large Mode Area                            |
| MI    | : | Modulation Instability                     |
| MOF   | : | Microstructured Optical Fiber              |
| mPOF  | : | Microstructured Polymer Optical Fibers     |
| mTIR  | : | Modified Total Internal Reflection         |
| NLSE  | : | Nonlinear Schrödinger Equation             |
| OCT   | : | Optical Coherence Tomography               |
| OTDM  | : | Optical Time Domain Multiplexing           |
| PBG   | : | Photonic Band Gap                          |
| PC    | : | Polycarbonate                              |
| PCF   | : | Photonic Crystal Fiber                     |
| PE    | : | Polyethylene                               |
| PEC   | : | Perfectly Electric Conductor               |
| PMC   | : | Perfectly Magnetic Conductor               |
| PML   | : | Perfectly Matched Layer                    |
| PoCF  | : | Porous Core Fiber                          |

|      |   |                                  |
|------|---|----------------------------------|
| SaD  | : | Stack And Draw                   |
| SC   | : | Supercontinuum                   |
| SCG  | : | Supercontinuum Generation        |
| SEM  | : | Scanning Electron Microscope     |
| SMA  | : | Small Mode Area                  |
| SPM  | : | Self-Phase Modulation            |
| SRS  | : | Stimulated Raman Scattering      |
| SSFM | : | Split Step Fourier Method        |
| SSFS | : | Soliton Self-Frequency Shift     |
| TOD  | : | third order dispersion           |
| THz  | : | Terahertz                        |
| UV   | : | Ultraviolet                      |
| WDM  | : | Wavelength Division Multiplexing |
| XPM  | : | Cross-Phase Modulation           |
| ZDF  | : | Zero Dispersion                  |
| ZDW  | : | Zero Dispersion Wavelength       |

## LIST OF SYMBOLS

|               |   |   |
|---------------|---|---|
| $\beta$       | : | propagation constant                        |
| $n_{eff}$     | : | Effective refractive index                  |
| $n_{FSM}$     | : | Fundamental Space Filling Mode              |
| $k$           | : | vacuum wave vector                          |
| $\Lambda$     | : | Pitch of a PCF                              |
| $d$           | : | Air hole diameter in a PCF                  |
| $n_{mat}$     | : | Refractive Index of the background material |
| $n_{CL}$      | : | Refractive Index of the cladding            |
| $n_{core}$    | : | Refractive Index of the core                |
| $\alpha$      | : | Attenuation Constant                        |
| $v_g$         | : | group velocity                              |
| $n_g$         | : | Group refractive index                      |
| $V$           | : | Normalized Frequency                        |
| $a$           | : | core radius                                 |
| $a_{eff}$     | : | Effective core radius                       |
| $\gamma$      | : | Nonlinear coefficient                       |
| $n_2$         | : | nonlinear refractive index                  |
| $R$           | : | bending radius                              |
| $f$           | : | filling factor                              |
| $\beta_2$     | : | dispersion parameter                        |
| $I$           | : | intensity                                   |
| $L$           | : | propagating a distance                      |
| $P_0$         | : | peak power                                  |
| $T_0$         | : | Pulse width                                 |
| $L_D$         | : | Dispersive length                           |
| $L_{NL}$      | : | nonlinear length                            |
| $\omega_{as}$ | : | frequency of anti-Stokes photons            |



|               |   |  |
|---------------|---|--|
| $\omega_{st}$ | : | frequency of Stokes photons  |
| $\omega_p$    | : | frequency of the pump photons                                      |
| $\lambda$     | : | wavelength   |
| $c$           | : | speed of light   |
| $\omega_0$    | : | carrier frequency  |
| $\tau_1$      | : | Raman period   |
| $\tau_2$      | : | Raman lifetime   |
| $N$           | : | Order of soliton   |
| $\hat{D}$     | : | differential operator that accounts for dispersion and absorption  |
| $\hat{N}$     | : | nonlinear operator that governs the effect of fiber nonlinearities |
| $F_T$         | : | Fourier-transform  |

# CHAPTER 1

## INTRODUCTION

The term Photonic Crystal Fiber was first pioneered by Philip St. J. Russell in the 1990's [1]. Photonic Crystal Fiber (PCF) is a kind of fiber which has a number of microscopic air holes throughout its entire length. Its structure is such that there is periodic refractive index or structural variation along its axis which makes it different from conventional fibers and the exploration of the great variety of possible applications have attracted huge interest. PCFs guide light by two mechanisms. Photonic Band-Gap Fibers follows Photonic Band Gap mechanism and here the light is guided in air holes. Whereas in case of Holey Fiber (also called the index- guided fiber) light is guided in the solid core made of pure silica by modified Total Internal Reflection (mTIR) mechanism [2]. Optical fibers have a very broad range of applications, where they serve many purposes, such as simply transporting light from a source to some other device, transmitting optically encoded data, sensing temperature or strain in some environment, generating and amplifying laser light. These properties can be more easily achieved in PCFs as these fibers offer many degrees of freedom in their design than those of conventional optical fibers. The numerous structural parameters can be tailored to obtain desirable values of dispersion, birefringence, confinement loss bending loss etc. for particular applications. This phenomenon has made this one of the most active fields of current optics research.

### 1.1 Guidance Mechanism in Index-Guided PCF

It is possible to use a two-dimensional photonic crystal as a fiber cladding, by choosing a core material with a higher refractive index than the cladding effective index. An example of this kind of structures is the PCF with a silica solid core surrounded by a photonic crystal cladding with a triangular lattice of air-holes, shown in Fig. 1.1. These fibers, also known as index-guiding PCFs, guide light through a form of total internal reflection (TIR), called modified TIR. To simplify, the idea is that in a high-index core microstructured optical fiber (MOF), the average refractive index of the cladding is lower than that of the core refractive index, leading to an equivalent geometry similar to those

of conventional step-index fibers. The idea behind mTIR, however, is deeper, and more rigorous, than this simple approach of looking at average refractive indices. We know that light propagating in a step-index fiber can be decomposed into modes, each of which is characterized by a propagation constant  $\beta$ , which is the component of the wave vector along the direction of the fiber. We saw that, depending on the magnitude of  $\beta$ , waves are radially propagative in the core and in the cladding. The same analysis can be applied to the different regions of a PCF. From our discussion of a step-index fiber we already know that in the core, which is a homogeneous region of refractive index  $n_{core} = n_{mat}$ , fields with  $n_{eff} = \beta/k_0 < n_{core}$  are propagative in the radial direction, and fields with  $n_{eff} > n_{core}$  are evanescent. In case of PCF, in the cladding region, one has to solve Maxwell's equations for a periodic medium. However, an important point is that all solutions for Maxwell's equations in the photonic crystal are either propagative or evanescent along the radial direction. The propagative solution to Maxwell's equations with the largest  $n_{eff}$  is called the fundamental space-filling mode (FSM), and the associated value of  $n_{eff}$  is  $n_{FSM}$ . By definition, no propagative fields having  $n_{eff} > n_{FSM}$  exist in the cladding, which is similar to the situation of a homogeneous cladding for which no propagative fields having  $n_{eff} > n_{CL}$  exist. For the range  $n_{FSM} < n_{eff} < n_{mat}$  propagative fields exist in the core region, which is exactly the same situation as we had for a step-index fiber.

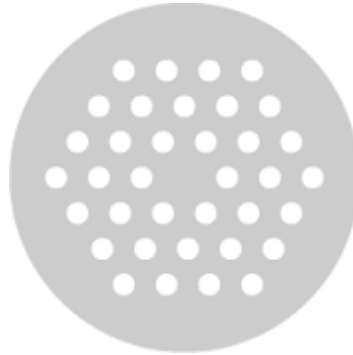


**Fig. 1.1** Triangular lattice solid-core PCF.

## 1.2 Photonic Band-gap Fiber

If the central part of the array of air holes is replaced by a bigger hole of much larger diameter in comparison to the surrounding holes, then the fiber so obtained is called the Photonic band-gap fiber. Since here the periodicity of the structure is broken, the defect

so introduced causes a change in its optical properties [3]. The phenomenon that guides light in the fiber is photonic band-gap according to which if the frequency of the external light matches the band-gap frequency, the light gets trapped in the hole and thus is guided throughout the length of the fiber. Therefore there is no need of having a greater refractive index of the core. Fig. 1.2 illustrates the Photonic Band Gap Fiber showing a large air hole in the center surrounded by an array of air holes.

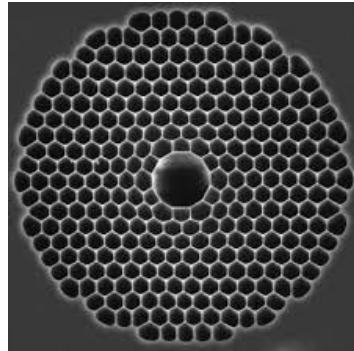


**Fig. 1.2** Photonic band-gap fiber.

### **1.3 Guidance Mechanism in Photonic Band-gap Fiber**

Photonic band-gap fibers guide light at a low-index “defect” site within the photonic crystal lattice which forms the cladding. At a given frequency, the band gaps appear in a range of values of the propagation constant  $\beta$  in which one would normally expect propagating modes, and they are surrounded at both higher and lower values of  $\beta$  by propagating modes. Band gaps can occur for values of  $\beta < k$  ( $k$  is the vacuum wave vector), and so can be used to trap light in an air core. However, the range of  $\beta > k$  for which bandgaps occur is limited. This means that in a photonic bandgap fiber only a limited range of wavelengths can be expected to be guided in the hollow core. It is important to underline that gaps can appear for values of modal index both greater and smaller than unity, enabling the formation of hollow-core fibers with bandgap material as a cladding. These fibers, which cannot be made using conventional optics, are related to Bragg fibers, since they do not rely on TIR to guide light. In fact, in order to guide light by TIR, it is necessary a lower-index cladding material surrounding the core, but there are no suitable low-loss materials with a refractive index lower than air at optical frequencies [1]. The first PCF which exploited the PBG effect to guide light was reported in 1998 [2, 4], and it is shown in Fig. 1.3. Notice that its core is formed by an additional air-hole in a

honeycomb lattice. This PCF could only guide light in silica that is in the higher-index material.

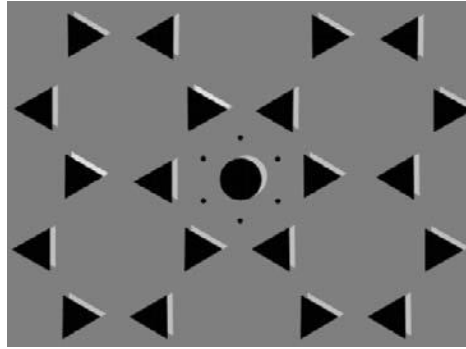


**Fig. 1.3** Cross-section of first photonic bandgap PCF with honey-comb lattice structure.

Hollow-core guidance had to wait until 1999, when the PCF fabrication technology had advanced to the point where larger air-filling fractions, required to achieve a PBG for air guiding, became possible [2]. Notice that an air-guided mode must have  $\beta/k < 1$ , since this condition guarantees that light is free to propagate and form a mode within the hollow core, while being unable to escape into the cladding. The first hollow-core PCF, reported in Fig. 1.2, had a simple triangular lattice of air-holes, and the core was formed by removing seven capillaries in the center of the fiber cross-section. By producing a relatively large core, the chances of finding a guided mode were improved. When white light is launched into the fiber core, colored modes are transmitted, thus indicating that light guiding exists only in restricted wavelength ranges, which coincide with the photonic bandgaps [2].

## **1.4 Properties and Applications of Photonic Crystal Fiber**

A huge variety of air-holes arrangements is possible in PCFs, offering a wide possibility to control the refractive index contrast between the core and the photonic crystal cladding and, as a consequence, novel and unique optical properties. Since PCFs provide new or improved features, beyond what conventional optical fibers offer, they are finding an increasing number of applications in ever-widening areas of science and technology.

### **1.4.1 Solid core Fibers**

Index-guiding PCFs, with a solid glass region within a lattice of air-holes, offer a lot of new opportunities. These opportunities are related to some special properties of the photonic crystal cladding, which are due to the large refractive index contrast and the

two-dimensional nature of the microstructure, thus affecting the birefringence, the dispersion, the smallest attainable core size, the number of guided modes and the numerical aperture and the birefringence.

### 1.4.2 Highly Birefringent Fibers

Birefringent fibers are defined as two orthogonally polarized modes carried in a single-mode fiber propagate at different rates, are used to maintain polarization states in optical devices and subsystems. The guided modes become birefringent if the core microstructure is deliberately made twofold symmetric, for example, by introducing capillaries with different wall thicknesses above and below the core. By slightly changing the air-hole geometry, it is possible to produce levels of birefringence that exceed the performance of conventional exceed the performance of conventional birefringent fiber by an order of magnitude. It is important to underline that, unlike traditional polarization maintaining fibers, such as bow tie, elliptical-core or Panda, which contain at least two different glasses, each one with a different thermal expansion coefficient, the birefringence obtainable with PCFs is highly insensitive to temperature, which is an important feature in many applications. An example of the cross-section of a highly birefringent PCF is reported in Fig. 1.4.

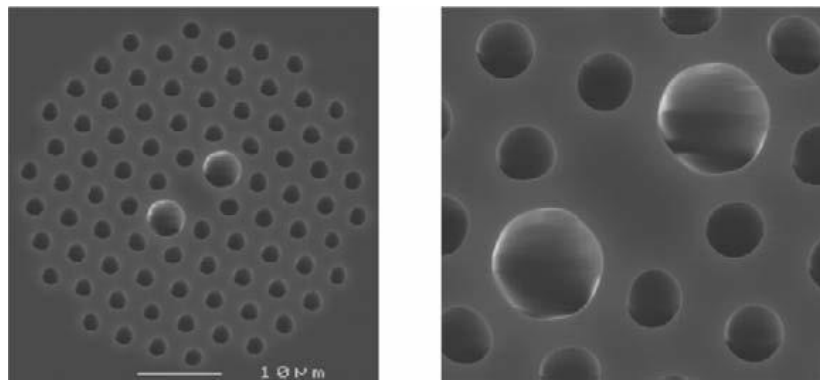


**Fig. 1.4** (a) the cross-section and (b) the core region of a highly birefringent triangular PCF.

### 1.4.3 Dispersion Tailoring

In PCFs, the dispersion can be controlled and tailored with unprecedented freedom. In fact, due to the high refractive index difference between silica and air, and to the flexibility of changing air-hole sizes and patterns, a much broader range of dispersion

behaviors can be obtained with PCFs than with standard fibers. For example, as the air-holes get larger, the PCF core becomes more and more isolated, until it resembles an isolated strand of silica glass suspended by six thin webs of glass. If the whole structure is made very small, the zero-dispersion wavelength can be shifted to the visible, since the group velocity dispersion is radically affected by pure waveguide dispersion. On the contrary, very flat dispersion curves can be obtained in certain wavelength ranges in PCFs with small air-holes, that is with low air-filling fraction. As an example, a dispersion-flattened triangular PCF with seven air hole rings, characterized by  $\Lambda = 2.5 \mu\text{m}$  and  $d = 0.5 \mu\text{m}$ , has been presented in [5].

#### **1.4.4 Ultrahigh Non-linearities**

An attractive property of solid-core PCFs is that effective index contrasts much higher than in conventional optical fibers can be obtained by making large air-holes, or by reducing the core dimension, so that the light is forced into the silica core. In this way a strong confinement of the guided-mode can be obtained, thus leading to enhanced nonlinear effects, due to the high field intensity in the core. An important example is the so-called supercontinuum generation, that is the formation of broad continuous spectra by the propagation of high power pulses through nonlinear media. The term supercontinuum does not indicate a specific phenomenon, but rather a plethora of nonlinear effects, which, in combination, lead to extreme spectral broadening. The determining factors for supercontinuum generation are the dispersion of the nonlinear medium relative to the pumping wavelength, the pulse length and the peak power. Since the nonlinear effects involved in the spectral broadening are highly dependent on the medium dispersion, a proper design of the dispersion properties can significantly reduce the power requirements. The widest spectra, in fact, can be obtained when the pump pulses are launched close to the zero dispersion wavelength of the nonlinear media.

#### **1.4.5 Large mode area Fibers**

By changing the geometric characteristics of the fiber cross-section, it is possible to design PCFs with a completely different property that is with large effective area. The typical cross-section of this kind of fibers, called large mode area (LMA) PCFs, consists of a triangular lattice of air-holes where the core is defined by a missing air-hole. LMA

PCFs are usually exploited for high-power applications, since fiber damage and nonlinear limitations are drastically reduced. In particular, LMA fibers are currently used for applications at short wavelengths, that is in ultraviolet (UV) and visible bands, like the generation and delivery of high-power optical beams for laser welding and machining, optical lasers, and amplifiers, providing significant advantages with respect to traditional optical fibers [4].

#### **1.4.6 Hollow core Fibers**

Hollow core PCFs have great potential, since they exhibit low nonlinearity [2] and high damage threshold, thanks to the air-guiding in the hollow core and the resulting small overlap between silica and the propagating mode. As a consequence, they are good candidates for future telecommunication transmission systems. Another application is the delivery of high-power continuous wave (CW), nanosecond and sub-picosecond laser beams, which are useful for marking, machining and welding, laser-Doppler velocimetry, laser surgery, and terahertz (THz) generation [6]. In fact, optical fibers would be the most suitable delivery means for many applications, but at present they are unusable, due to the fiber damage and the negative nonlinear effects caused by the high optical powers and energies, as well as to the fiber group-velocity dispersion, which disperses the short pulses [6]. These limitations can be substantially relieved by considering hollow-core fibers. Moreover, air-guiding PCFs are suitable for nonlinear optical processes in gases, which require high intensities at low power, long interaction lengths and good-quality transverse beam profiles. Finally, the delivery of solid particles down a fiber by using optical radiation pressure has been demonstrated [2].

### **1.5 Fabrication Technology of PCFs**

#### **1.5.1 Stack and Draw (SaD) Technique**

This method introduced by Birks et al. in 1996, has become the preferred fabrication technique. Since it allows relatively fast, clean, low-cost, and flexible perform manufacture. PCF preforms are formed by stacking a number of capillary silica tubes and rods to form the desired air/silica structure. This way of creating the preform allows a high level of design flexibility as both the core size and shape as well as the index profile throughout the cladding region can be controlled. When the desired preform has been



constructed, it is drawn to a fiber in a conventional high-temperature drawing tower and hair-thin photonic crystal fibers are readily produced in kilometer lengths. Through careful process control, the air holes retain their arrangement all through the drawing process and even fibers with very complex designs and high air filling can be produced. Finally, the fibers are coated to provide a protective standard jacket that allows robust handling of the fibers. The final fibers are comparable to standard fiber in both robustness and physical dimensions and can be both striped and cleaved using standard tools. Though it seems that SaD is not suitable for the fabrication of more complex PCFs (like equiangular spiral PCFs) [7] other than hexagonal lattice PCFs, a technique has been proposed in [8] to adapt the standard SaD for complex structures.

### 1.5.2 Extrusion Fabrication Process

In extrusion a material is pushed or draw through a tool called die which is use to shape materials of desired cross-section. Extrusion process is applied to the glasses other than silica which are not readily available in the form of tubes. In this fabrication process a molten glass is forced through a die containing a suitably designed pattern of holes. Extrusion allows fiber to be drawn directly from bulk glass, using a fiber-drawing tower, and almost any structure, crystalline or amorphous, can be produced. It works for many materials, including polymers, and compound glasses. The structured preform of 16 mm outer diameter and the jacket tube are extruded. The preform is reduced in scale on a fiber-drawing tower to a cane of about 1.6 mm diameter in caning process. The cane is inserted within the jacket tube. This assembly is drawn down to the final fiber. This method can also be applied to other commercial glasses, including some with higher nonlinearity and slightly lower intrinsic loss. In particular, a tellurite PCF with an outer diameter of 190  $\mu\text{m}$  and a core diameter of 7  $\mu\text{m}$  has been realized [9].

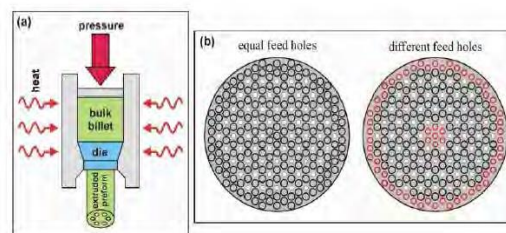


**Fig. 1.5** (a) Sketch of extrusion process and (b) extrusion die concepts with equal and different size feed holes for a target preform structure.

### 1.5.3 Filling Technology

The optical properties of silica-air photonic crystal fiber (PCF) can be radically altered by filling its hollow channels with materials such as metals, polymers or semiconductors. Various different techniques have been used previously, including high-pressure chemical vapor deposition and pumping in of molten metal at high pressure. Chemical routes have the drawback that the end products of the reaction remain in the channels, often adversely affecting the optical properties. Filling with pure molten material does not suffer from this disadvantage, so that structures of high optical quality can readily be produced. In [10], the optical properties of PCFs in which one, two or more holes, adjacent to the core, are filled with semiconductors, glasses or metals by using a pressure cell technique have been reported. In Fig. 1.6, Scanning Electron Microscope (SEM) image of fabricated a filled channel of PCF has been shown. This filling procedure allows the core mode to interact strongly with the material of the wire, leading to a strong modification of the light transmission.

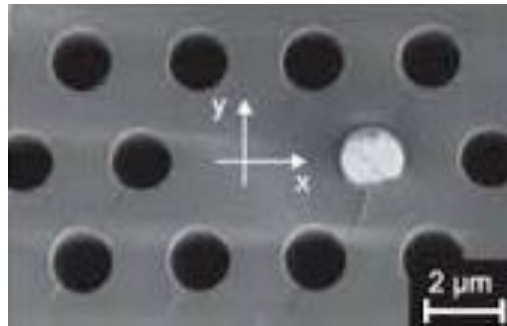


**Fig. 1.6** SEM image of a germanium-filled endlessly single-mode PCF.

### 1.5.4 Sol-gel Technique for Irregular Shaped PCF Fabrication

The sol-gel casting technique was originally developed for the production of large jacket tubes for optical fiber preforms and has been modified for the fabrication of microstructured fiber. A number of microstructured fibers fabricated using the sol-gel casting method, are shown in Fig. 1.7. A mold containing an array of mandrel elements is assembled and then filled with colloidal silica dispersed at high  $p^H$  with an average particle size of 40 nanometers. The  $p^H$  is lowered causing the sol to gel. At the wet gel stage, the mandrel elements are removed, leaving air columns within the gel body. The gel body is then treated thermo chemically to remove water, organic and transition metal

contaminants. The dried porous gel body is then sintered near 1600°C into viscous glass and subsequently drawn into fiber. The air holes are pressurized during draw to obtain the desired size and air-fill fraction. To maintain uniformity along the length of the preform, the mandrels are individually tensioned and the positioning and spacing is inspected and recorded with a digital camera.

As a casting method, the sol-gel technique can fabricate any structure, which can be assembled into a mold. The hole size, shape and spacing may all be adjusted independently. By comparison, stack and draw methods are limited to closest-packed geometries such as triangular or honeycomb lattices and cannot easily generate circular patterns. Drilling methods allow adjustment of both the hole size and spacing, but are generally limited to a small number of holes and restricted to circular shapes. Furthermore, drilling of preforms leads to roughened surfaces along the air hole so that extra steps of etching and polishing of the inner surfaces are desired. Extrusion techniques provide design freedom, but are typically limited to soft glasses for which the material loss values are exceedingly high. Several designs such as fibers for higher nonlinearity, dispersion flattened designs require independent spacing, hole size or even non circular holes. The sol-gel casting method provides additional design flexibility that will be necessary for such fibers. Sol-gel casting is not without its own set of challenges. The mandrel elements are removed during the wet gel stage, while the gel body is still fragile. Removal of the mandrels at this stage places strain on the gel and for gel bodies with air-fill fractions >25%, cracking of the gel body is common and lowers the overall yield. Numerous microstructured fiber designs such as hollow core photonic band gap fibers or highly nonlinear fibers require air-fill fractions near 90%. To fabricate fibers with high air-fill fractions, the low air-fill fraction glass preforms are etched with HF uniformly along the length of the preform. An example of using HF etching to increase the air fill-fraction of a preform is shown in Fig. 1.8. Additionally, the air-fill fraction may be increased by pressurizing the air holes during draw. The larger design freedom, low-cost starting materials, dimensional precision, low material contamination and the ability to scale up to large preforms (> 10 km of fiber) makes this fabrication method an attractive approach towards high performance, low-cost microstructured fiber.

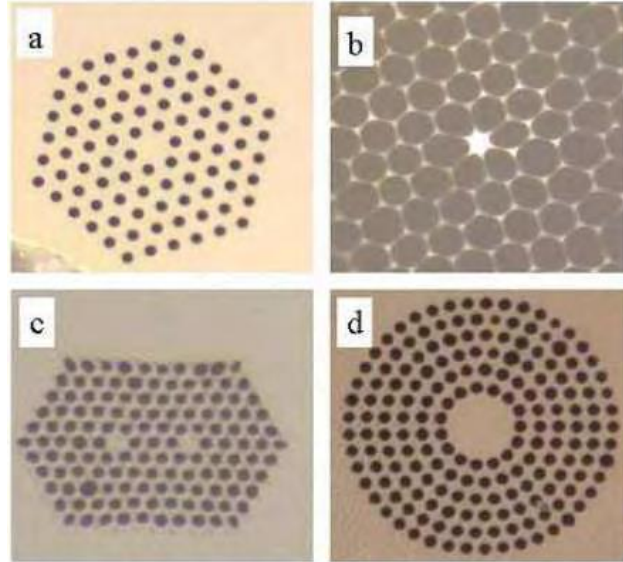


**Fig. 1.7** Cross-sectional images of sol-gel derived microstructured fibers. a) endlessly single moded design, b) high delta, highly nonlinear fiber, c) dual core structure and d) circular core microstructured fiber.

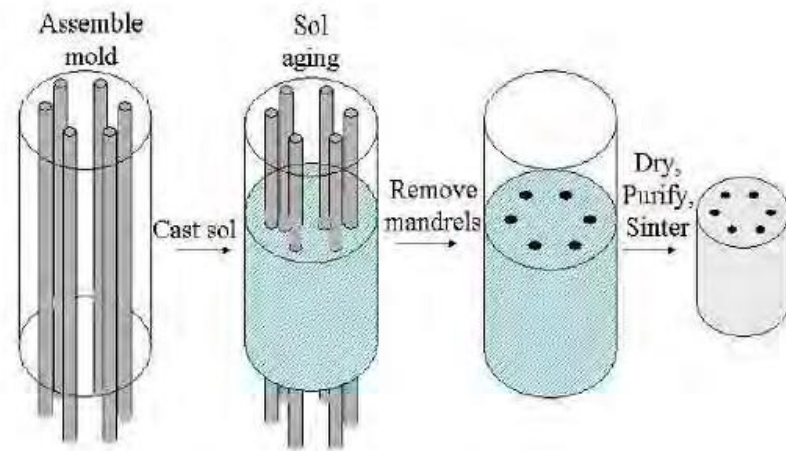


**Fig. 1.8** Schematic representation of sol gel fabrication technique.

## 1.6 Literature Review

Spectral broadening and the generation of new frequency components are inherent features of nonlinear optics, and have been studied intensively since the early 1960s. A fascinating perspective on the history of this subject has been given by Bloembergen (2000). This particular process known as supercontinuum (SC) generation occurs when narrow-band incident pulses undergo extreme spectral broadening at output. SC generation is a complex spectral broadening process where a narrow bandwidth pulse undergoes a substantial expansion through the interplay between various linear

phenomena such as dispersion and nonlinear phenomena such as self-phase modulation (SPM), cross-phase modulation (XPM), four-wave mixing (FWM), stimulated Raman scattering (SRS), and soliton dynamics at pump wavelength [11, 12] that occur during the propagation of the optical signal along the length of the waveguide. This phenomenon was first discovered by Alfano and Shapiro [13, 14]. The study of the SC generation has gained importance since the spectrum generated has high degree of optical coherence and has found useful in many applications in the fields of frequency metrology, optical coherence tomography (OCT), molecular spectroscopy, biomedical imaging, gas sensing, food quality control, and early cancer cell detection [15-19].

In the past years, numerous efforts were taken on silica fibers to produce broadband SC spectra. In 2000, Ranka obtained an ultra-broadband continuum in a silica fiber with anomalous dispersion at visible wavelengths [20]. In 2002, Dudley et al. reported SC generation in an air-silica MOF with nanosecond and femtosecond pulse pumping [21]. Thereafter, many results of SC generation in silica MOFs and photonic crystal fibers (PCFs) were presented [22-24]. The characteristics of PCFs that have led to such interest relate to their guidance properties that yield single-mode propagation over broad wavelength ranges, their enhanced modal confinement and therefore elevated nonlinearity, and the ability to engineer their group velocity dispersion [25]. The design freedom of PCFs has allowed SC generation to be observed over a much wider range than has been possible with bulk media or conventional fibers. Alternative to silica, SC generation was also demonstrated using bismuth, lead silicate, fluoride, and tellurite fibers [26-29]. Recently chalcogenide glasses have shown a number of advantages over the other materials mentioned above [30-36].

So far most of the studies on supercontinuum generation using PCFs are based on silica and other glasses as background materials due to their low material loss, tunable zero dispersion wavelength and small effective areas [20], [37-41]. In addition to glass and other solid bulk materials [42-44], supercontinuum pulses can be created in gases [45], [46] and liquids [45] also. But, the reliability of the supercontinuum source suffers from inherent brittleness of glass materials as well as high losses in bending. Some of the recent studies [47-50] show that polymer based optical medium may be the good solutions to overcome these drawbacks, though the study of nonlinear effects in polymer based PCFs has not yet been demonstrated [51]. On the other hand, the unique ability of PCFs to host functional materials in their cladding air holes have opened the window for

the development of all fiber nonlinear devices [51-53]. Also, the modal properties can be tuned by incorporating liquid crystal, high index liquids, polymers, glasses, etc., as active materials inside the holes of the PCFs [50]. Taking these facts into consideration, in this work a single mode polymer PCF with integrated silica film is used for supercontinuum generation over broad spectral range and numerical simulations is also performed

## **1.7 Objective of the Thesis**

This thesis is mainly focused on supercontinuum generation in polymer PCF in near-infrared regime. To do so, the study of nonlinear pulse propagation in polymer PCF is essential which was not studied in earlier works. Hence, the main objective is to generate a broad-band supercontinuum pulse in polymer PCF for the enhancement of reliability and all-fiber nonlinear devices. The objectives of this work are:

1. To design a model of triangular lattice polymer PCF for supercontinuum generation which will be useful in the field of high performance OCT imaging systems, where a broad-band light source with high penetration depth and high degree of coherence with sufficient brightness are required for spatial resolution.
2. To investigate the wavelength dependencies of single mode behavior, dispersion, bending loss, effective area, nonlinearity parameter, fractional power flow in different regions of the PCF with the variation of different structural parameters.
3. To study numerically simulated broadband supercontinuum pulse in the polymer PCF.
4. To evaluate the sensitivity of the generated supercontinuum varying fiber length, input power, and higher order dispersion coefficients.

## **1.8 Organization of the Thesis**

This thesis is focused on supercontinuum generation in polymer PCF in near-infrared regime. Thesis paper is divided into the following six chapters.

Chapter 1 (this chapter) describes general introduction about photonic crystal fiber and layout of this thesis. Also, the major objectives of thesis are described.

Chapter 2 constitutes a detailed study on polymer PCF. This chapter highlights the application of polymer PCF as a waveguide for terahertz pulse propagation, its fabrication process and the physics of various terahertz properties such as fundamental space-filling mode, dispersion, endlessly single mode operation, effective area, non-linearity, bending loss, power fraction etc.

Chapter 3 represents the results of numerical simulations of the polymer PCF made from High density Polyethylene (HDPE). Terahertz properties discussed in chapter 2 are presented and compared here with the experimental and reported works. At the end of the chapter, we summarize our findings.

Chapter 4 describes general introduction to supercontinuum generation and physical mechanism involved. Moreover, dispersion, different non-linear phenomenon such as self-phase modulation, self-steeping, four wave mixing, Raman scattering, soliton fission etc. are also described in this chapter. Numerical modeling of supercontinuum generation as well as solution of generalized nonlinear Schrodinger equation using split-step method are also described.

In Chapter 5 step by step design and analysis procedures to generate supercontinuum pulse in a hybrid polymer PCF are presented. Results of numerical simulations of supercontinuum generation are also presented. The effects on supercontinuum spectra by varying different parameters such as peak power, pulse duration, length of PCF are studied in this chapter.

Chapter 6 contains some remarkable conclusions regarding the present study and suggestions for the future work.

## CHAPTER 2

### POLYMER PHOTONIC CRYSTAL FIBER

Our main objective is to generate broad-band supercontinuum pulse in polymer PCF in near-infrared region. Before proceed to supercontinuum generation, a detailed study on polymer PCF is essential. Besides many other applications, polymer materials e.g. Polycarbonate (PC), Polyethylene (PE) etc. make the PCF a promising waveguide for pulse propagation in THz range due to its broad transparent window and low losses at higher frequencies. In this chapter modal characteristics of a polymer based PCF designed for THz guidance are thoroughly discussed.

#### 2.1 Terahertz Radiation: Opportunities and Development

The THz window of the electro-magnetic spectrum lies between the infrared band and the microwave band i.e. in between photonic and electronic region, and ranges in frequency from 0.1 to 10 THz (equivalently wavelength ranges from 3 mm – 30  $\mu\text{m}$ ). THz, also known as sub-millimeter waves or far-infrared radiation, bridging the gap between optics and electronics.

In mid 1980's with the development of sub-picosecond lasers experiments on coherent generation and detection of THz began. The groups at Bell laboratories and IBM successfully implemented the THz time-domain spectrometer [54]. This setup allows both amplitude and phase data to be directly obtained from the sample scans. Recent developments in the field of THz technology include optically induced THz sources and detectors [55], suitable electro-optic materials [54], and surface emitters and low-temperature THz quantum cascade lasers [55]. High-power THz sources have also been demonstrated in free-electron lasers and accelerators, while remote long distance (tens of meters) detection via THz acoustic waves enhancement has also been realized. Several important discoveries and applications in science and engineering have been highlighted as a result of the intense studies of the THz band.

Dynamic growth in research concerning generation and detection of THz radiation has contribute to understanding the physical light-matter interactions,



noninvasive biological imaging [54-55], as well as chemical substance finger printing [55] and active security scanners [56]. It has also motivated the studies of previously unexplored physical phenomena such as negative refraction in metamaterials (an artificially engineered material in which the structure influences the waves behavior resulting in unconventional properties of the material). The advent of increasingly effective techniques for nanotechnology will promote compact and portable THz systems.

## **2.2 Photonic Crystal Fiber (PCF) as THz waveguide**

The recent progress in terahertz (THz) wave generation and detection techniques has generated much interest in low loss THz waveguides which are essential for the construction of compact THz devices and measurement systems. However, most of the present THz systems rely on free space propagation and processing of THz waves due to the virtual absence of low loss waveguides at THz frequencies. The conventional guiding structures such as microstrips, coplanar striplines, and coplanar waveguides fabricated on semiconductor substrates can support only a limited bandwidth due to their excessive dispersion and loss. For example, the power absorption coefficients of coplanar striplines and coplanar waveguides are  $\alpha = 20\text{cm}^{-1}$  at 1 THz [56]. Even for metallic rectangular waveguides, the absorption coefficient is still very high,  $\alpha = 20\text{cm}^{-1}$  at 0.1 THz [56]. Recently, there have been several reports on quasi-optical techniques for the efficient and broadband coupling of free space THz radiation into low loss waveguides such as metal, sapphire fiber, and plastic ribbon waveguides [57-59].

On the other hand, the photonic crystal fiber PCF has raised growing interest over the past few years since it offers the opportunity to fabricate optical waveguides with enhanced linear and nonlinear optical properties. For example, compared to the conventional optical fibers, the PCF exhibits broadband single-mode operation [60] and air guiding for the reduced nonlinearity and dispersion [61].

A typical PCF consists of a waveguiding core and a spatially distributed periodic cladding region. The core is formed by introducing a defect into the photonic crystal structure to create a localized region with optical properties different from the surrounding cladding region. The guiding mechanism of a PCF depends on whether the effective refractive index of the core is higher or lower than that of the cladding. The

high-index core PCF can transmit broadband THz signals while the air-core PCF can be used as an ultralow loss, narrow band THz waveguide.

So far most PCFs have been fabricated from silica due to their applications in optical domain. However, the material loss of silica is prohibitively high at THz frequencies. Thus, for THz applications, low loss materials such as plastics need to be used.

### 2.3 Materials for THz Transmission

The first dielectric waveguide for THz guiding was proposed in the year 2000, where a plastic ribbon made from high density polyethylene (HDPE) of rectangular cross-section was used as the core and the surrounding air acted as the cladding [58]. Though the achieved loss was low ( $\sim 1\text{cm}^{-1}$  over 0.1 – 3.5 THz) for 10 mm length of ribbon, dispersion was too high. The first circular core dielectric step index fiber for THz guidance was proposed in 2006 [61]. It was just a simple plastic (PE) wire of sub-wavelength diameter (200  $\mu\text{m}$ ) that acted as the fiber core with the surrounding air acting as the cladding. This structure supports a single mode ( $\text{HE}_{11}$ ) at frequencies of up to 0.3 THz. However, the mode confinement is poor which limits its propagation length, and the bending loss is also quite high. In such step index structures, the dispersion management is difficult as it depends primarily on material dispersion. In this context, microstructured fibers (PCFs) are quite promising, since light guiding is not only controlled by index contrast but can be easily manipulated through multi-parameters of the wave guiding geometry, and the total dispersion becomes a strong function of waveguide dispersion [62-63].

In 2002, Han et. al. experimentally demonstrated a HDPE based solid-core microstructured fiber [56], whose cladding was formed by arranging air holes on HDPE matrix in a periodic triangular fashion. By tuning the structural parameters, both dispersion as well as mode confinement could be tuned appropriately. As a result, the structure offers single mode guidance over 0.1 – 3 THz with low loss and relatively low dispersion. A Teflon based solid-core microstructured fiber was fabricated and first demonstrated for THz guidance (over 0.1 ~ 1.3 THz) in 2004 [64]. As the Teflon is a very cost effective and flexible material, it can be drawn into a longer fiber length as compared to other polymers. Recently, COC (trade name is Topas) material based large

mode area (LMA) and small mode area (SMA) solid-core microstructured fibers have been Fabricated for THz guidance [65]. Both of the proposed fibers possess low loss ( $\sim 0.09 \text{ cm}^{-1}$ ) over 0.35 ~ 0.65 THz. Moreover, the high confinement of fiber modes makes them less bend sensitive.

In search of further loss reduction, researchers proposed that the insertion of a loss-less low-index air gap (size must be less than the decay length of the operating wavelength) inside the solid core can reduce the material absorption loss significantly [65]. In 2008, two research groups, Hassani et al. [67-68] and Atakaramians et al. [69] theoretically proposed a porous- core fiber (PoCF) structure for efficient THz guiding, where instead of one air-hole, a two-dimensional periodic array of air holes is included in the core region. In both cases, the PoCF structures are optimized to get maximum power fraction in the air holes. Recently, a plastic (Teflon)-based porous-core with a porous-cladding fiber has been proposed [70], where air holes are arranged in hexagonal periodic fashion in both the core and the cladding regions.

Apart from index guided (IG) structures, several other dielectric- based fiber geometries have been proposed and demonstrated. Unlike IG-fibers, light can be guided in the lower refractive index region of such fibers. Since the core is composed lower refractive index than the surrounding cladding, it allows the use of air (the best material for THz guidance) as the core material to further reduce the loss as well as dispersion of the transmitted THz wave. The fundamental guiding mechanisms in such fibers are, PBG-guidance, anti-resonance reflective (ARR)-guidance and sometimes simply reflective guidance.

## **2.4 Fabrication of Polymer Microstructured Fibers**

The use of polymers to create microstructured fibers allowed a wide variety of structures to be constructed, which require new method for fabrication. The best-known technique to fabricate microstructured polymer optical fibers (mPOFs) is similar to silica glass PCF manufacturing technology; although in case of polymer materials this process requires lower temperatures. Fabrication process of mPOF consists of two steps. First one is creating several centimeter width preform and the second is extrusion of previously created perform. The lower end of preform is heated to 200<sup>0</sup>C and its diameter is reduced to final diameter of created fiber. In the end the polymer coating is applied to fiber. The

extrusion process can be continuous or batch. The former process requires that a monomer, an initiator and chain transfer agent are continuously put into the reactor and fiber is continuously withdrawn from the die. The process can be different in details based on the type of manufactured fiber [71]. Different techniques to create mPOFs, other than extrusion, are: the interfacial gel polymerization technique [61], the diffusion technique [72], drilling [73], and injection moulding [74]. Fabrication processes of mPOFs have the advantage over glass fiber manufacturing. The main reason for that is, apart from lower processing temperature and cheaper materials, polymer fibers are not restricted by close packed arrangement of circular holes, which in result hole structure is not restricted to hexagonal or square package (as in PCF) and allows to create different material modification.

Apart from fabrication advantages compared to silica fibers, mPOFs have also superiority in other fiber properties. While in glass fibers possibilities for modifying the properties by doping are limited by high processing temperature, polymers can be specifically designed. Also mPOFs can be fabricated from single polymer without the use of dopants and as a result wider choices of polymers are available [75].

## 2.5 THz Fiber Characteristics

In this section, we provide a general overview of the characteristics of the THz waveguide in terms of desired optical properties. The fiber performance can be described in terms of its modal type, its propagation loss coefficient, and the mode dispersion behavior.

### 2.5.1 Computation of Fundamental Space-filling Mode (FSM)

In a photonic crystal fiber the core index is greater than the average index of the cladding because of the presence of the air holes. For this reason, the fiber can guide light by total internal reflection (TIR). If the guided light has an effective index,  $n_{eff}$ , for TIR it must satisfies the condition:

$$n_{core} > n_{eff} = \frac{\beta}{k_0} > n_{FSM} \quad (2.1)$$

where  $\beta$  is the propagation constant,  $n_{core}$  is the core index, and  $n_{FSM}$  is the effective cladding index. It is sometimes referred to as the fundamental space-filling mode of the infinite cladding of a photonic crystal. If case of a silica fiber  $n_{core}$  is reduced to the

index of silica. If the value of  $n_{eff}$  is less than  $n_{FSM}$ , light could be radiated from the core, so it is utmost important to determine the cladding effective index,  $n_{FSM}$  accurately.

Value of  $n_{FSM}$  is determined by applying the full-vector finite element method (FEM) to the so-called elementary piece of the cladding that acts like a boundless propagation medium [76]. Conditions for Perfectly Magnetic Conductor (PMC) and Perfectly Electric Conductor (PEC) are applied to the boundary of the elementary piece. The elementary piece of the cladding used to compute  $n_{FSM}$  is shown in Figure 2.1.

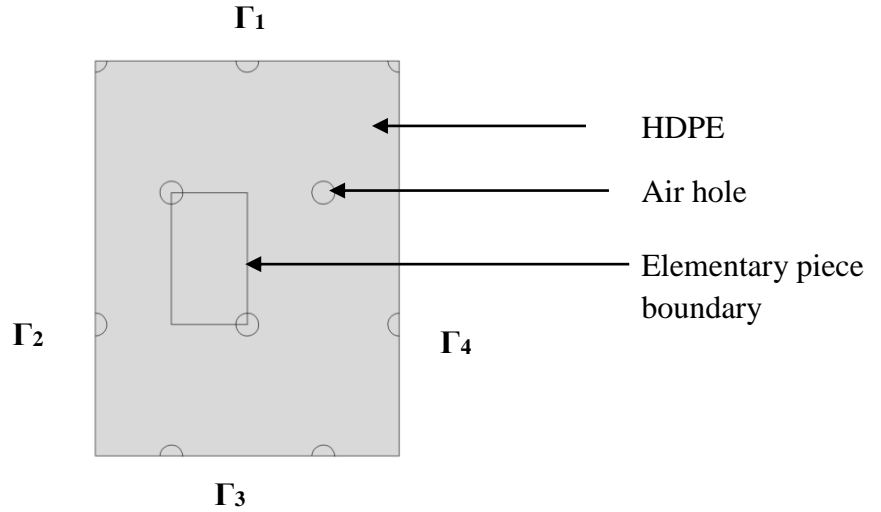


**Fig. 2.1** Elementary piece of cladding used to compute  $n_{FSM}$ .

The boundary conditions used to compute  $n_{FSM}$  are summarized in Table 2.1.

**Table 2.1**  
Boundary conditions used to compute  $n_{FSM}$ .

| Boundary                  |                           | Polarization |
|---------------------------|---------------------------|--------------|
| $\Gamma_1$ and $\Gamma_3$ | $\Gamma_2$ and $\Gamma_4$ |              |
| PMC                       | PEC                       | x            |
| PEC                       | PMC                       | y            |

### 2.5.2 Dispersion

Dispersion is due to the different propagation speeds for each of the spectral components, and this causes a pulse to spread. The temporal broadening of the pulse propagating through a fiber can cause significant signal distortions. In general, the source of dispersion in fibers is not individually determined. However, the contribution to the

dispersion in the single-mode fiber with no birefringence is set only by the fiber's material dispersion and the waveguide dispersion, as the modal and polarization mode dispersion are zero. Often, the fiber material is chosen from dielectrics with low dispersion (i.e. almost constant refractive index across the frequency range of interest).

In the THz range, a few examples of polymers with low dispersion have been measured such as ultrahigh-molecular-weight polyethylene, Zeonex, and Topas. In a high index-guiding fiber the material dispersion is unavoidable. Therefore, to further reduce the overall dispersion in this fiber, not only the fiber has to be made of a low-dispersion dielectric, the choice of the geometry of the structure of the fiber must also be optimized to minimize the waveguide dispersion over a wide frequency bandwidth. Meanwhile in a hollow core fiber, where the material dispersion is negligible, the configuration of the cladding structure plays an important role in influencing the characteristics of waveguide dispersion.

To quantify the dispersive behavior of the fundamental mode in a fiber, the propagation constant of the mode can be expanded in a Taylor series about the center frequency  $\omega_0$ ,

$$\beta(\omega) = \beta_0 + \beta_1(\omega - \omega_0) + \frac{1}{2}\beta_2(\omega - \omega_0)^2 + \dots \quad (2.2)$$

where

$$\beta_m = \left( \frac{d^m \beta}{d\omega^m} \right)_{\omega=\omega_0} \quad (m = 0, 1, 2, \dots) \quad (2.3)$$

The parameters  $\beta_1$  and  $\beta_2$  are related to the effective refractive index and its derivatives through the relations [12]

$$\beta_1 = \frac{1}{v_g} = \frac{n_g}{c} = \frac{1}{c} \left( n + \omega \frac{dn_{eff}}{d\omega} \right) \quad (2.4)$$

governs the group velocity  $v_g$ , of the pulse envelope in the waveguide, and

$$\beta_2 = \frac{d}{d\omega} (\beta_1) = \frac{1}{c} \left( 2 \frac{dn_{eff}}{d\omega} + \omega \frac{d^2 n_{eff}}{d\omega^2} \right) \quad (2.5)$$

determines the temporal broadening of the pulse, better known as the group velocity dispersion (GVD). In the optical domain, it is often quoted in unit of  $ps^2 \cdot km^{-1}$ . In this thesis, the GVD,  $\beta_2$  values for the THz fibers are quoted in  $ps \cdot THz^{-1} cm^{-1}$ .

### 2.5.3 Endlessly Single-mode Fiber (ESMF)

A photonic crystal fiber can support fundamental mode for all wavelengths or frequencies. This is known as the endlessly single-mode property of a PCF. To verify this property in the THz polymer PCF, it is important to parameterize the optical properties in terms of V parameter. The V parameter in the Step-index fiber is given by [77]

$$V = \frac{2\pi f}{c} a \sqrt{n_{co}^2 - n_{cl}^2} \quad (2.6)$$

Where  $a$  is the core radius and  $n_{co}$  and  $n_{cl}$  are core and cladding indices respectively. However, in case of PCF this equation is not valid because  $a$ ,  $n_{co}$  and  $n_{cl}$  are not clearly defined in a PCF. By introducing a modified V parameter this problem can be solved. Which is given by [77]  $V_{eff} = \frac{2\pi f}{c} a_{eff} \sqrt{n_{eff}^2 - n_{FSM}^2}$ , where  $n_{eff}$  is the effective index of the fundamental mode, and  $n_{FSM}$  is the effective cladding index known as fundamental space filling mode. Values of  $n_{FSM}$  are determined by applying the full-vector finite element method (FEM) to the so-called elementary piece in the cladding region [76]. Effective core radius  $a_{eff}$  is taken as  $\Lambda/\sqrt{3}$  [76].

Since in a PCF  $V_{eff}$  tends to a constant at high frequencies, and that the limit decreases with decreasing hole size, if the holes are sufficiently small it is in principle possible that a fiber will remain single moded even at arbitrarily high frequencies [60]. In other words, for some high-index core PCFs, however small the wavelength is compared with the core size, only a single mode is guided. For example, in this study the solid-core THz PCF shown in Figure 3. is endlessly single mode for  $d/\Lambda < 0.65$  regardless of  $n_{mat}$ . Such fibers are called endlessly single-mode fibers (ESMF), and are one of the most exciting breed of photonic crystal fibers.

The importance of ESMF is twofold. First, ESMF allow single-mode propagation over very broad wavelength ranges, and as we will see shortly this can be combined with very strong optical non-linearities, yielding the potential for non-linear interactions over broad wavelength ranges within the same spatial mode.

Second, the possibility of creating an ESMF also implies that, for a given range of wavelengths, a solid-core PCF with an arbitrarily large core can be single mode, offering unprecedented possibilities. In the field of telecommunications or high-powered fiber lasers for example, where single-mode guidance is essential, at equal operating power levels larger cores result in lower power density, and thus lower non-linearities. In large-

core fibers, light can be injected with higher power without the power density reaching levels at which non-linear effects become problematic - meaning that in telecom applications the distance between repeaters can be greatly increased, and in laser applications higher-powered lasers can be fabricated. Whilst PCFs have not so far been seriously considered for long-range telecom applications, recent demonstrations have used the fact that ESMF open up new single-moded wavelength ranges to multiplex signals across the infrared and visible spectra to yield ultra-high bandwidth transmission.

#### 2.5.4 Effective Mode Area

Effective mode area is another important parameter of PCF. It is the quantitative measure of area that a fiber mode covers in transverse dimension. Effective mode area is the effective measure of area in which fundamental mode is confined during propagation of light in fiber. The effective mode area is expressed as [78]

$$A_{eff} = \frac{(\iint |E|^2 dx dy)^2}{\iint |E|^4 dx dy} \quad (2.7)$$

where  $E$  is the electric field amplitude. The integration is done not only over the core area, but over the whole plane. For optical nonlinearities in PCF effective mode area is the major parameter that is to be considered. Undesirable nonlinear impairments can be suppressed by large mode area in PCF. Optical nonlinearities always depend on the power density inside the device. Therefore, for a fixed power, the higher the effective area, the lower will be the effect of nonlinearities. One of the ongoing challenges in PCF structure designing is the design of structures having small mode areas that lead to a high nonlinear coefficient. Various approaches are used to obtain desired effective mode area like varying the size of the air holes in the cladding region, varying hole-to-hole spacing [80]. For a fixed pitch it is possible to increase the effective area significantly by narrowing the air-holes or by enlarging the pitch for a fixed  $d/\Lambda$  value.

In the photonic crystal fiber structure by Ademgil *et al.* [80] it is clear that effective mode area increases steadily with the increases in wavelength. It can be also noted that with increasing hole to hole spacing effective mode area is increasing. This would contribute to increase the nonlinearities produced by power dependence refractive index.



### 2.5.5 Non-linearity

The nonlinear effects in optical fibers mainly originate from nonlinear refraction, which is a phenomenon that refers to the intensity dependence of the refractive index. Nonlinear coefficient ( $\gamma$ ) is directly proportional to nonlinear refractive index ( $n_2$ ) and inversely proportional to the effective area ( $A_{eff}$ ). Non-linear coefficient of the analyzed PCF is evaluated based on the following equations [81]:

$$\gamma = \frac{2\pi cn_2}{\lambda A_{eff}} \quad (2.8)$$

Thus nonlinearity decreases with wavelength while effective mode area increases with wavelength Poli *et al.* [62] and Saitoh *et al.* [81].

The high index contrast of PCFs allows the fabrication of fibers with very small cores [20] in which light can be confined within a cross-sectional area nearly two orders of magnitude smaller than in conventional PCFs. This means that for the same input power the power density is nearly two orders of magnitude higher. Highly non-linear PCFs enable the propagation of light with very strong non-linear coefficients over long propagation lengths, meaning that non-linear effects could now be achieved over shorter fiber lengths or using lower powers. But making smaller core sizes than 1  $\mu\text{m}$  in diameter i.e. when the core is much smaller than the wavelength the evanescent tail of the mode grows in size and the light is less confined, so that for a given index contrast there is an optimum core size to maximize the non-linear effects [82]. However, the unusual dispersion properties of PCFs and their ability to remain single moded over very large ranges that really opened up entirely new possibilities, such as supercontinuum (SC) generation or fiber-based broadband parametric conversion.

### 2.5.6 Bending Loss

Bending can increase the attenuation of an optical fiber by two mechanisms: macrobending and microbending. Macrobending of an optical fiber is the attenuation associated with bending or wrapping the fiber. Light can leak out from a fiber when the fiber is bent. As the bend becomes more acute, more light leaks out. However, calculation of bending loss of the THz PCF cannot be performed directly. Therefore, an approximate analytical method is used [83]

$$\alpha = \frac{1}{8} \sqrt{\frac{2\pi}{3}} \frac{\Lambda^2}{A_{eff}} \frac{1}{\beta\Lambda} \frac{1}{\sqrt{\frac{2R}{3} \frac{V^3}{\Lambda(\beta\Lambda)^2}}} \exp\left(-\frac{2R}{3} \frac{V^3}{\Lambda(\beta\Lambda)^2}\right) \quad (2.9)$$

In Equation 2.9,  $R$  is the bending radius,  $A_{eff}$  is the effective area of the fundamental mode [78], and

$$V = \Lambda \sqrt{\beta^2 - \beta_{cl}^2} \quad (2.10)$$

is the effective V parameter of the PCF [84]. The propagation constant  $\beta$  is defined as

$$\beta = \frac{2\pi n_{eff}}{\lambda} \quad (2.11)$$

where  $n_{eff}$  is the effective index of the fundamental mode.

### 2.5.7 Power Fraction

The power fractions of the mode power in the fiber core which consists of the polymer material and some air holes can be defined as follows [85]:

$$F_x = \frac{\int x S_z dA}{\int all S_z dA} \quad (2.12)$$

where is the time average pointing vector in the z direction, the subscript x represents the calculated region (polymer material i.e. HDPE and cladding air-holes), and all refers to the region of all the parts of the THz PCF.

# CHAPTER 3

## MODAL ANALYSIS OF POLYMER PCF

### 3.1 Structural Details

The cross section of a triangular THz PCF is shown in Fig.3.1. Small circles denote air holes and except the circles the whole region is the background material, high density polyethylene (HDPE) of which the refractive index is 1.528 in THz frequency region. It contains 4 rings, each having  $6 \times n$  number of air holes (where  $n=1, 2, 3, 4$  introduces number of rings). The period and the diameter of holes are represented by  $\Lambda$  and  $d$ , respectively.

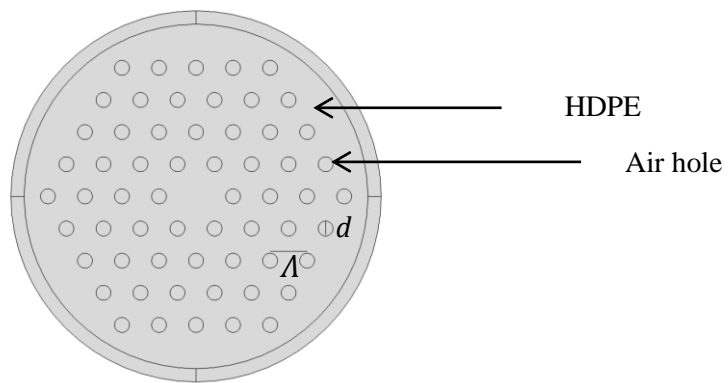


**Fig. 3.1** Cross sectional view THz PCF.

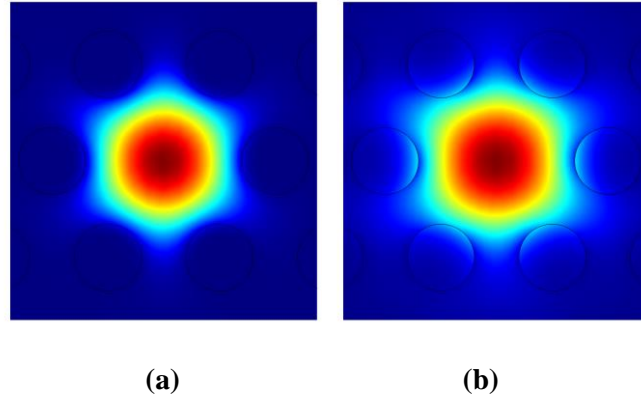
### 3.2 Methods Adopted

A single mode polymer PCF having four rings of air holes in the cladding in a triangular lattice will be designed using COMSOL Multiphysics version 4.2 for THz guidance. The diameter of all air holes in different rings will be kept equal for the simplicity of design. A full vector finite element method will be used to analyze various modal properties as functions of frequency. In all the calculations, anisotropic perfectly matched layer (PML) will be assumed outside the outermost ring of the air holes to reduce reflections. Solutions of fundamental space filling (FSM) mode, loss characteristics, nonlinearity and effective area, power fraction in different regions of the PCF with the variation of

different structural parameters will be investigated. The proposed structure will be analyzed for polymer material high density polyethylene (HDPE) due to its broad transparency window and mature fabrication technology.

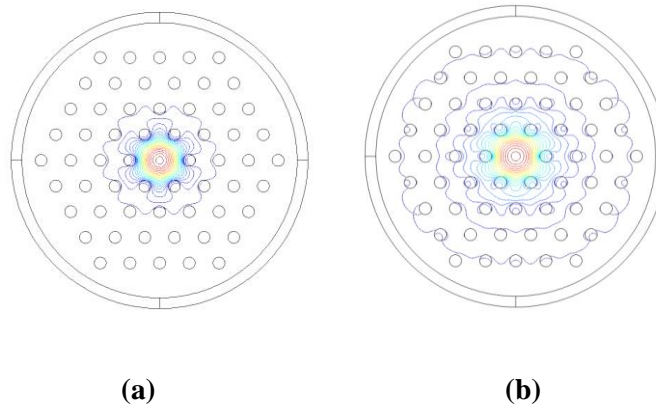
### 3.3 Mode Details and Properties

#### 3.3.1 Field Distribution of Core Mode



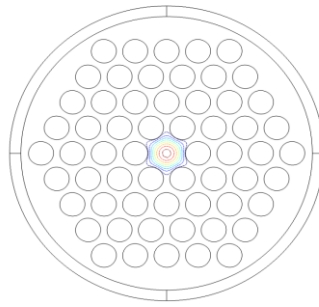
**Fig. 3.2** Electric field distribution of the fundamental mode of the THz PCF for  $d/\Lambda = 0.4$ , (a) for 1 THz (b) for 0.6 THz.

Figure 3.2 shows the dominant electric-field distribution of the fundamental mode for frequencies 1 THz and 0.6 THz respectively when  $d/\Lambda = 0.4$ . The light is more strongly confined in the core region of the THz PCF when the frequency is 1 THz. Further increase in frequency enhances the modal confinement. The obtained phenomenon is same as reported in [56].

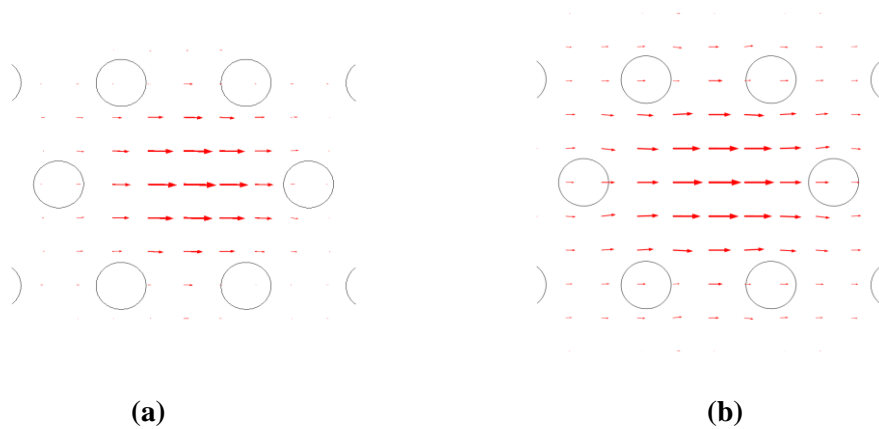


**Fig. 3.3** Contour plot of the electric field pattern of the fundamental mode of the THz PCF for  $d/\Lambda = 0.4$ , (a) for 1 THz (b) for 0.6 THz.

From figure 3.3 it is evident that the field pattern is dominated by minima occurring at the six nearest air holes but spreads out from the defect (core) and slightly interacts with the second ring of air holes when the frequency is 1 THz. At 0.6 THz, field spreads out and interacts with the polymer (HDPE) cladding in the region beyond the first ring of air holes and the interaction is visible up to the fourth ring of the air holes. The calculate field pattern for 1 THz is in good argument with the measurement [9]. Further increase in frequency and  $d/\Lambda$  ratio confine the light absolutely in the defect (core), which is shown in Figure 3.4.

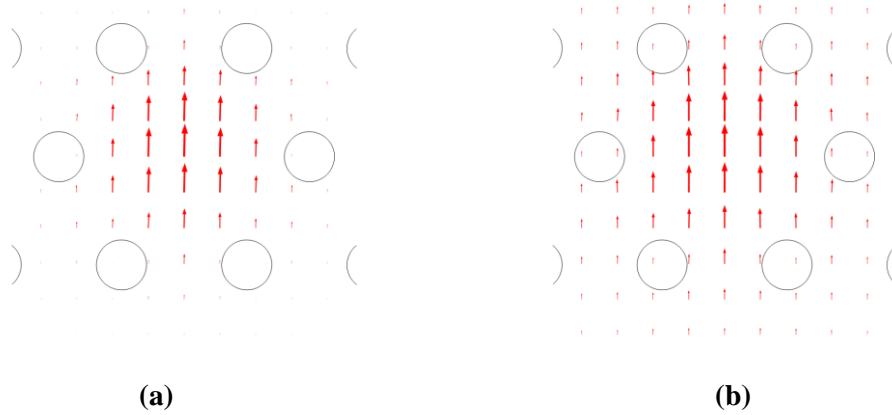


**Fig. 3.4** Contour plot of the electric field pattern of the fundamental mode of the THz PCF for  $d/\Lambda = 0.8$  at 10 THz.



**Fig. 3.5** Transverse electric field vector distributions of fundamental of the THz PCF for  $d/\Lambda = 0.4$ , (a) for 1 THz (b) 0.6 THz.

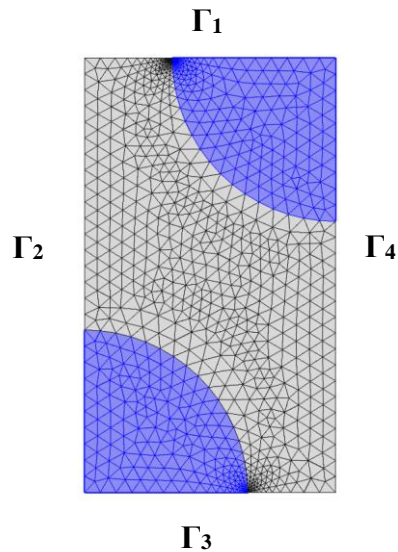
Transverse electric field vector distributions of the fundamental mode of the THz PCF are presented in Figure 3.5 for frequencies 1 THz and 0.6 THz respectively, when  $d/\Lambda = 0.4$ . A more uniform vector pattern is noted in case of 1 THz frequency. The corresponding magnetic field vector distributions for the same parameters are shown in Figure 3.6.



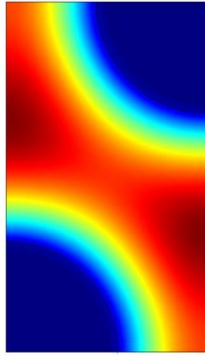
**Fig. 3.6** Transverse magnetic field vector distributions of fundamental of the THz PCF for  $d/\Lambda = 0.4$ , (a) for 1 THz (b) 0.6 THz.

### 3.3.2 Fundamental Space filling mode (FSM)

According to sub-section 2.5.1, values of fundamental space-filling mode can be determined by applying the full-vector finite element method (FEM) and conditions for Perfectly Magnetic Conductor (PMC) and Perfectly Electric Conductor (PEC) as presented in Table 2.1 to the so-called elementary piece of cladding that acts like a boundless propagation medium [76]. Figure 3.7 shows an element division profile of the elementary piece.



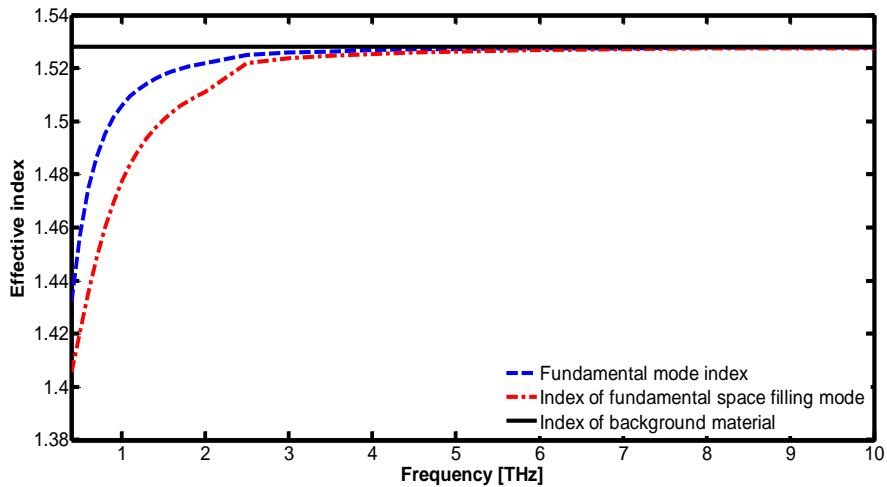
**Fig. 3.7** Element division of the elementary piece.



**Fig. 3.8** Normalized electric field for fundamental space-filling mode at 2 THz and  $d/\Lambda = 0.55$ .

Figure 3.8 shows the simulated normalized electric field distribution for fundamental space filling mode at 2 THz. As it is clear that the light is guided by the higher index portion i.e. HDPE and there is no light in the air hole portions of the elementary piece.

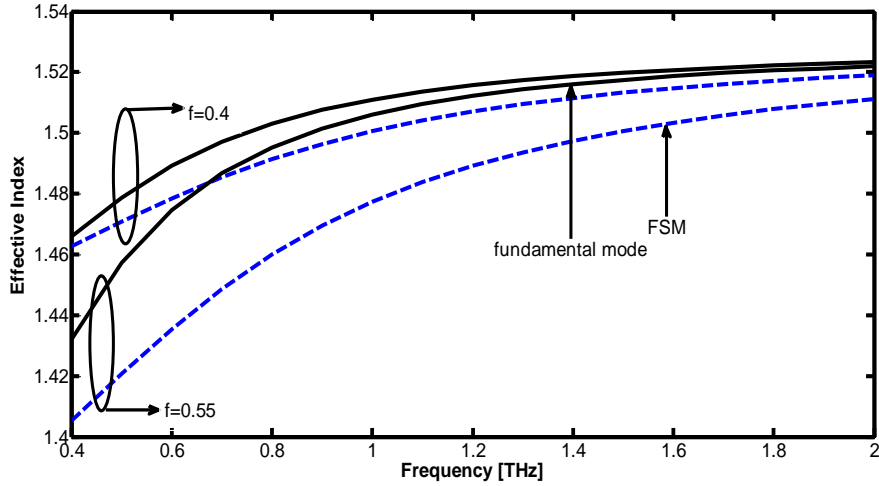
### 3.3.3 Structural dependence of modal properties



**Fig. 3.9** Effective mode indices as a function of frequency for filling factor,  $f = 0.4$ .

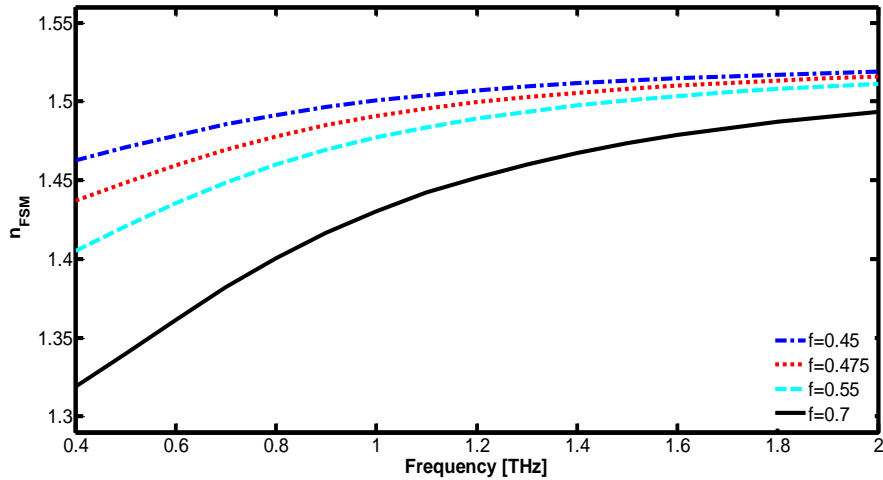
Variations in structural parameters, especially the air hole pitch  $\Lambda$  and the air hole diameter  $d$  affect the properties of the THz PCF. The ratio of  $d/\Lambda$  is also known as the air filling factor,  $f$  or simply filling factor. Variations of the effective indices for a wide frequency range up to 10 THz for both the fundamental mode and fundamental space filling mode for  $d/\Lambda = 0.4$  are shown in Figure 3.9. It can be noted that for both the modes the effective indices increase monotonically as the frequency increases and the effective index of the fundamental mode is greater than that of the space filling mode.

This satisfies the condition [76]  $n_{core} > n_{eff} = \frac{\beta}{k_0} > n_{FSM}$  for the propagation of light in an index-guided PCF.



**Fig. 3.10**  $n_{eff}$  and  $n_{FSM}$  for different filling factors,  $f$ .

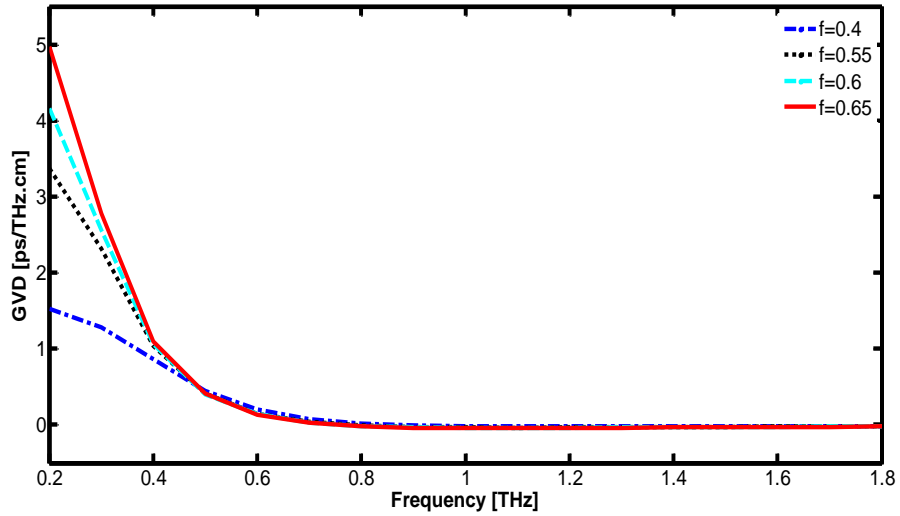
From the earlier figure it is evident that, for a specific  $d/\Lambda$  i.e. filling factor the effective index of the fundamental mode is greater than that of the space filling mode. In this case, varying filling factor i.e. 0.4 and 0.55 the same result is obtained and it is shown in fig. 3.10. Hence a conclusion can be drawn that the effective index of the fundamental mode is greater than that of the space filling mode, regardless to the fiber parameters. The results obtained are same as [86].



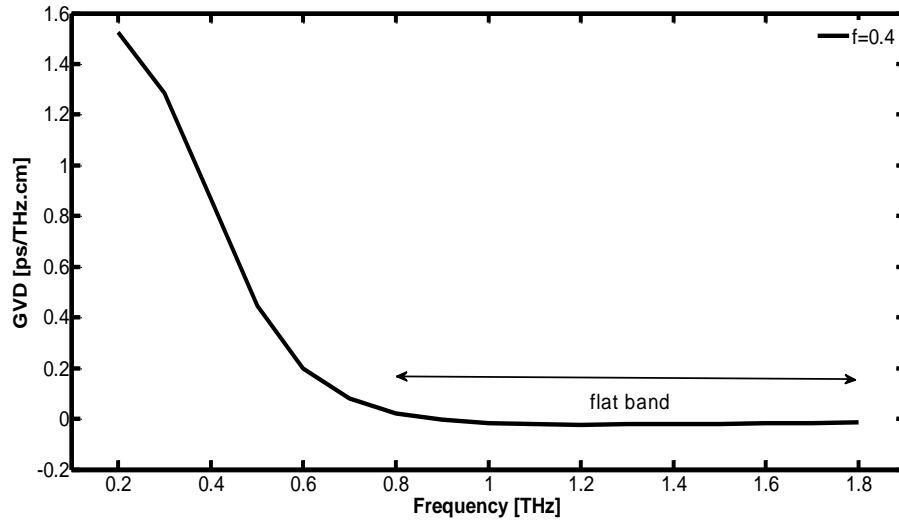
**Fig. 3.11** Effective index of the Fundamental space filling mode for the THZ PCF with different filling factors,  $f$ .



In Figure 3.11, we report the curves of indices of fundamental space filling mode ( $n_{FSM}$ ) as a function of frequency for different filling factors. Values of  $n_{FSM}$  are determined by applying the full-vector finite element method (FEM) to the so-called elementary piece in the cladding region [76]. It is known from [86] that, the effective indices of the space filling mode decrease by increasing filling factor or increasing the wavelength. In this case, as the frequency increases indices of the space filling mode increases and decreases as filling factor increases.

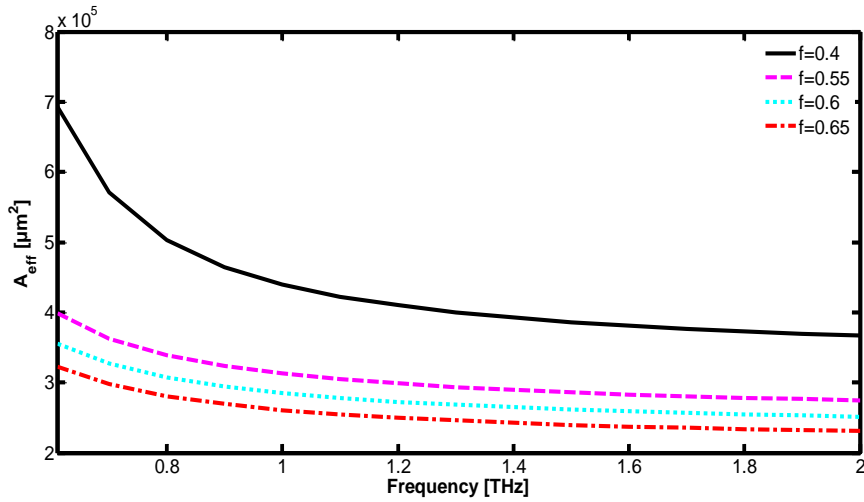


**Fig. 3.12** Dispersion as a function of frequency for various filling factors,  $f$ .

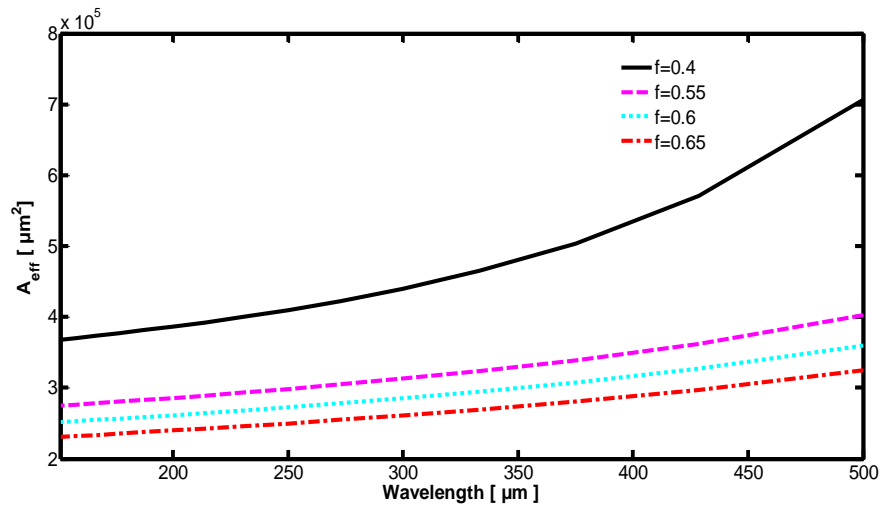


**Fig. 3.13** Dispersion profile for the THz PCF with  $\Lambda = 500 \mu\text{m}$  and filling factor,  $f = 0.4$ .

Figure 3.12 shows the curves of dispersion parameter  $\beta_2$  (ps/THz.cm) of the fundamental mode of the THz PCF for various  $d/\Lambda$  with same pitch,  $\Lambda = 500 \mu\text{m}$ . As it can be observed, with the increase of filling factor i.e.  $d/\Lambda$  the positive peak increases and a flat dispersion profile is noticed when  $d/\Lambda$  decreases. Above the ZDF each figure shows a flat dispersion property in the high frequency range and below the ZDF,  $\beta_2$  increases sharply as the frequency decreases and maximum reaches to near 4.975 ps/THz.cm when the frequency is lowest i.e. 0.2 THz. Moreover, the demonstrated curves indicate that  $\beta_2$  is negative i.e. anomalous dispersion and close to zero at broad band. The above observations are fairly matched with [77], [87-89]. The flattened dispersion behavior of the THz PCF is presented by figure 3.13 which is comparable to [77].

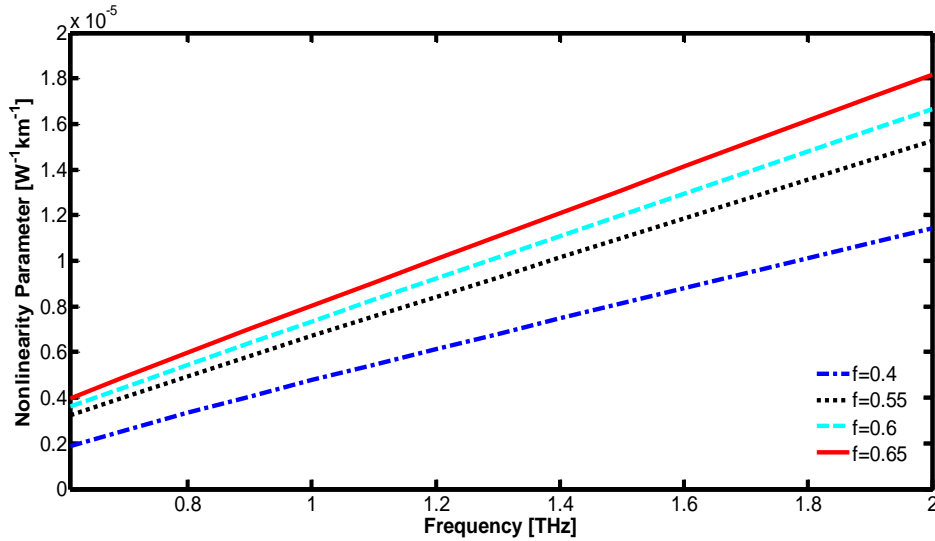


**Fig. 3.14** Effective Area as a function of frequency for different filling factors,  $f$ .



**Fig. 3.15** Effective area as a function of wavelength for different filling factors,  $f$ .

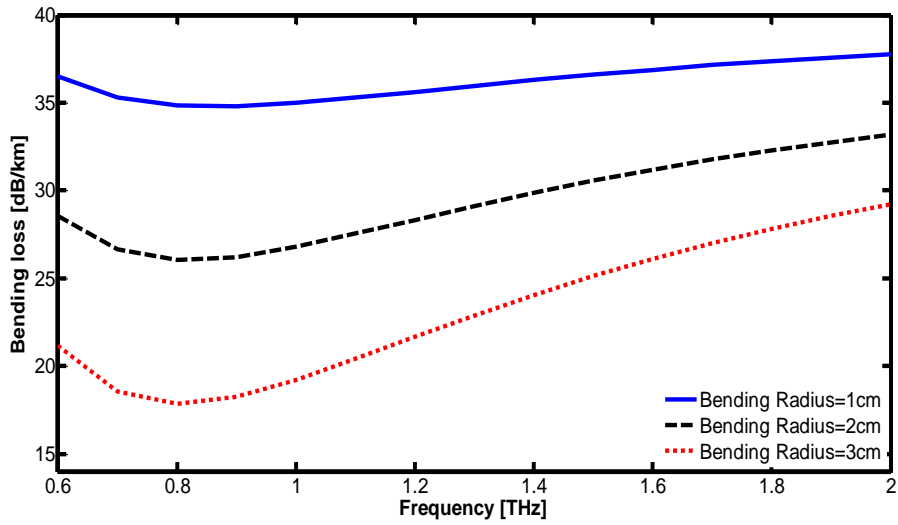
Figure 3.14 and 3.15 show the effective mode area of the fundamental mode of the THz PCF as a function of both frequency and wavelength for different filling factors,  $f$ . It can be noted that the effective mode area steadily decreasing with the increment of frequency. Since the confinement of fundamental mode increases as the frequency increases [56] the effective mode area decreases. Analyzing the effect of filling factor i.e.  $d/\Lambda$  on effective mode area it is worth mentioning that with the increase of filling factor effective mode area further decreased. Increase of filling factor means increasing the air hole size since  $\Lambda$  is restricted to  $500 \mu\text{m}$ , the mode becomes more confined, and hence the effective area reduces [90]. The calculated  $A_{eff}$  of the THz PCF are comparable to those in [91].



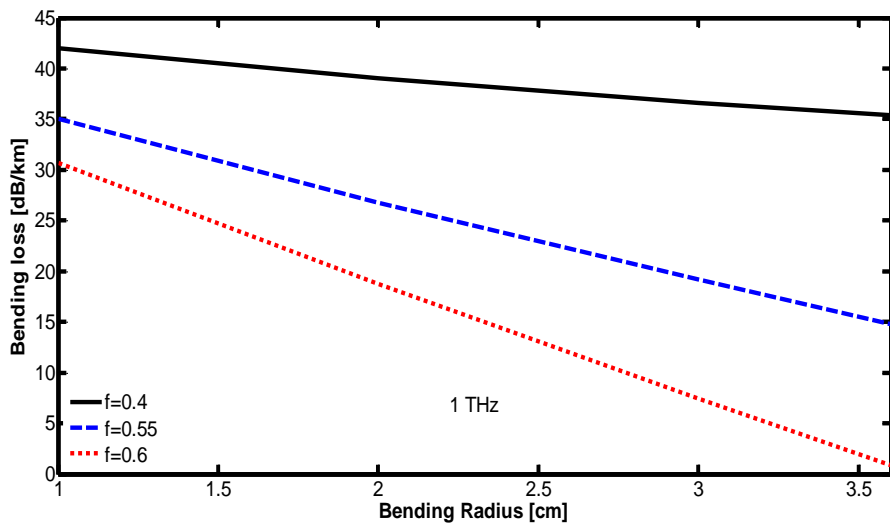
**Fig. 3.16** Nonlinearity parameter as a function of frequency for various filling factors,  $f$ .

Variation of nonlinear coefficient as a function of frequency is presented in figure 3.16. As showed in Equation (2.8) the nonlinear coefficient is inversely proportional to the effective area, large effective mode area leads to small nonlinear coefficient [92]. The numerically calculated values of nonlinearity parameter of the THz PCF are close enough to [93].

The frequency dependence of the bending loss is also calculated and shown in Figure 3.17. For a small bending radius the loss is high, while it is reduced for increased bending radius. This is because, when the bending is increased, radius of the curvature of the bent portion is reduced [94]. Therefore, bending loss should be high at the lower values of bending radius.



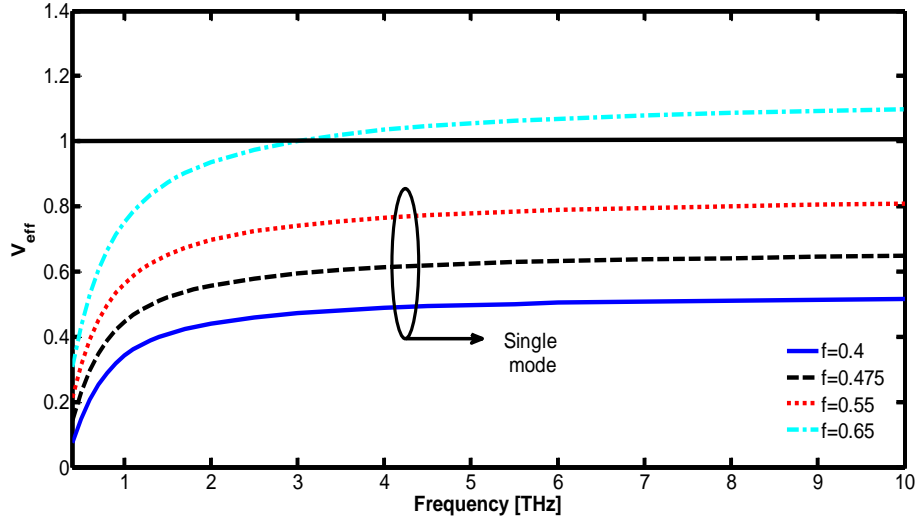
**Fig. 3.17** Bending Loss as a function of frequency for filling factor,  $f = 0.55$ .



**Fig. 3.18** Bending loss as a function of bending radius for different filling factors,  $f$  when frequency is restricted to 1 THz.

Figure 3.18 is presented in favor of this argument as a function of bending radius for different filling factors when the frequency is restricted to 1 THz. The obtained curves are comparable to [95]. It is also noted that with the increase of filling factor bending loss tends to decrease. Increasing of filling factor means to increase the air hole diameter, since pitch is fixed to 500  $\mu\text{m}$ . Hence confinement of mode power increased and therefore the loss reduces.

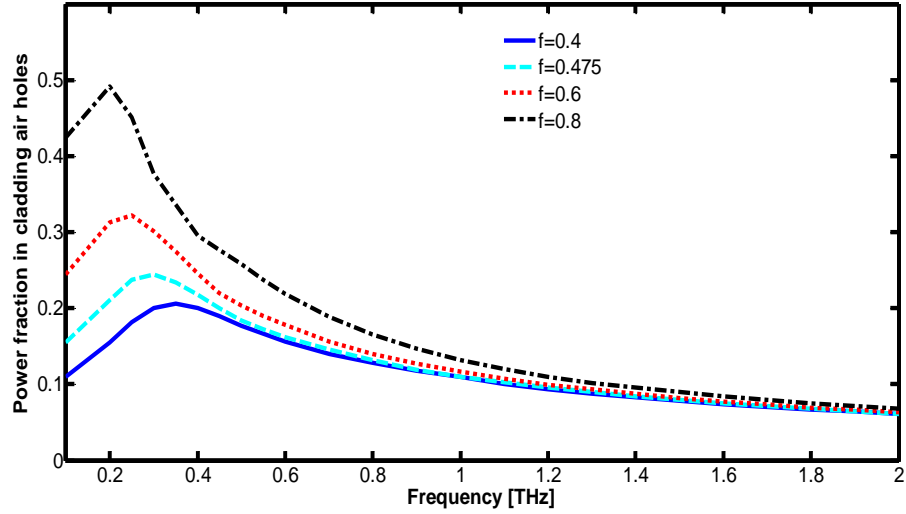
By introducing a modified V parameter [77] the endlessly single-mode property for the THz PCF is determined. Values of fundamental space-filling mode are determined by applying the full-vector finite element method (FEM) to the so-called elementary piece in the cladding region [76]. Effective core radius  $a_{eff}$  is taken as  $\Lambda/\sqrt{3}$  [76].



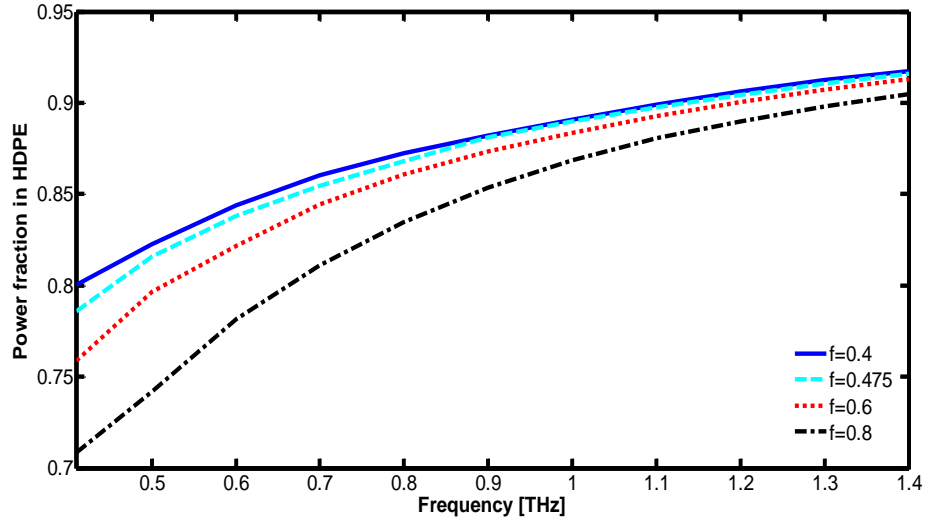
**Fig. 3.19** Normalized V parameters of the THz PCF for various filling factors,  $f$ .

Figure 3.19 shows the results obtained from numerical simulations of V parameter for various filling factors when  $\Lambda = 500 \mu\text{m}$ . The inset shows the values of filling factor  $f$ .  $V_{eff}$  is normalized to  $\pi$ . The proposed THz PCF is an endlessly single mode waveguide up to 3 THz and when filling factor is less than 0.65, a single-mode property up to 10 THz is noticed. The THz PCF can support only a single mode over a broad spectral range that can be used in situations where several wavelengths are required in the same fiber, such as in frequency-doubling applications [9]. In simulation it is noticed that, even for larger values of  $d/\Lambda > 0.65$ , the fiber behaves as endlessly single moded, and this is for two reasons. First, the cut-off wavelength of the second mode can be shorter than any realistic wavelength that will be used in the fiber. Second, even when there are a few higher-order modes, in many circumstances their propagation constants are substantially different from those of the fundamental mode, meaning coupling between fundamental and higher-order modes due to micro-bends or other perturbations is close to impossible. This means that if light is injected in the fundamental mode of the fiber it will stay in the fundamental mode, which is not the case for lower contrast index fibers. Experimentally,

it is relatively easy to couple most of the light into the fundamental mode rather than higher-order modes.



**Fig. 3.20** Power fraction in cladding air-holes as a function of frequency for different filling factors,  $f$ .



**Fig. 3.21** Power fraction in HDPE as a function of frequency for different filling factors,  $f$ .

The power fraction of the mode power in the fiber core which consists of the polymer material and some air holes is determined using Equation (2.12). Figure 3.20 and 3.21 illustrate the fractional power in the cladding air holes and in the polymer material i.e. HDPE respectively as a function of frequency for different filling factors. As it is noted that, power fraction in cladding air-holes is reducing slowly with the increase of

frequency, while the opposite case occur for polymer material. In case of cladding air-holes power fraction increase as the filling factor increases. Since increment in filling factor means the diameter of air-hole is increased, and comparatively more power will be available in the air-holes. More power in air-holes confirms lower power in polymer material. Hence, again an opposite scenario in case of increasing filling factor is noticed. Both the effects are demonstrated in Figure 3.22.

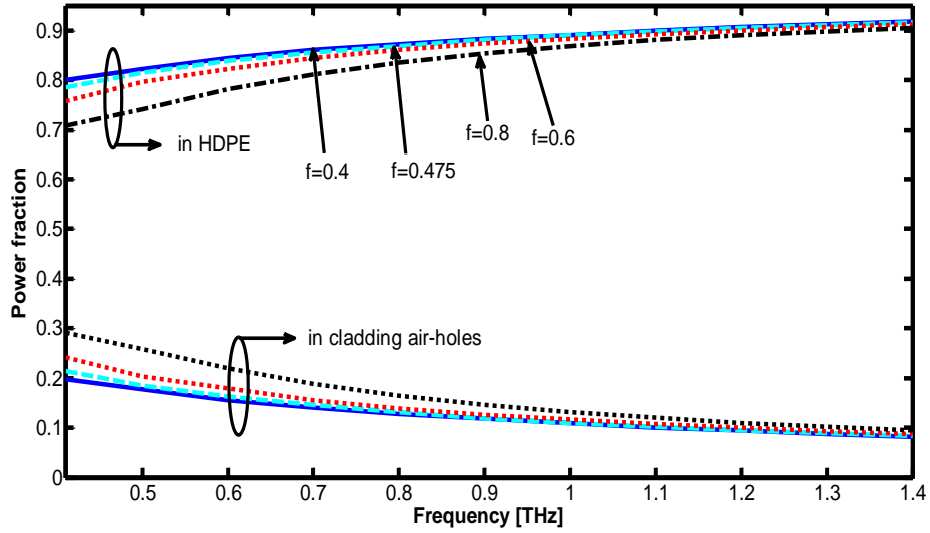


**Fig. 3.22** Power fraction in both HDPE, and cladding air-holes as a function of frequency for different filling factors,  $f$ .

## **CHAPTER 4**

### **THEORIES OF SUPERCONTINUUM GENERATION**

Supercontinuum (SC) generation in photonic crystal fiber (PCF) is a very hot research topic, and quite a number of theoretic and experimental investigations have been reported in recent years [20], [96, 97]. The interaction of intense (high power) pulses with a nonlinear optical medium such as Photonic Crystal Fiber (PCF) with high nonlinearity and suitable dispersion characteristics can lead to considerable broadening of the pulse spectrum at the end of the medium. The resulting spectrum can exceed several hundreds of nanometers, which is commonly referred to as supercontinuum (SC). When a pump laser with defined initial characteristics propagates through a length of fiber, the nonlinear processes in an optical fiber occur. The main nonlinear effects involved in the SC generation process include self-phase modulation (SPM), four-wave-mixing (FWM) or modulation instability (MI), Raman scattering, and the Soliton related effects (Soliton formation, Soliton propagation and break-up, Soliton self-frequency shift (SSFS), dispersive wave generation, Soliton or dispersive wave trapping. The parameters of the input pump laser and the properties of the fiber itself determine what kind of nonlinear effect would take place and the form of the output. Different conditions would result in distinct SC generation processes. In order to control the SC generation progress, not only the parameters of the pump source (pump wavelengths, pulse duration, and the pump power level) but also the properties of fiber (the material of fiber, geometry parameters) should be carefully considered. The conjunction of an optimized pump source with the matched fiber could yield the desired SC. Theoretically there are countless lasers that could be used as the pump sources. However, the available pump lasers are limited in practice, especially for the purpose of engineering. While the properties of the fiber, especially the dispersion property, also have notable influence on the SC generation progress. Thus designing a fiber to match a given pump source is more like a feasible solution [98].

Up to now, femtosecond, picosecond or even the continuous wave (CW) lasers have been used as the SC pumps. The femtosecond laser-pumped SC usually exhibits a broadband continuum range due to the high pulse peak power and short pulse duration,



while the system of the femtosecond pump source itself is complex [99]. The CW-pumped SC could obtain a high average power and high spectral power density output [40]. However, compared with the pulse-pumped SC, the CW-pumped SC has a relatively narrow spectral range. In fact, the picosecond fiber laser is an ideal SC pump source. On the one hand its high pulse peak power is helpful for exciting the nonlinear effects [101, 101]. The widest spectra are obtained when the pump pulses are launched close to the zero-dispersion wavelength. Supercontinuum generation, first observed in 1970 by Alfano and Shapiro in bulk borosilicate glass [13, 14]. The characteristics of PCFs that have made it a potential candidate for SC generation relate to their freedom in design, guidance properties that yield single-mode propagation over broad wavelength ranges sometimes referred to as endlessly single mode operation, their enhanced modal confinement i.e. small effective area, and therefore elevated nonlinearity, and the ability to engineer their group velocity dispersion.

#### **4.1 Conventional light source and Supercontinuum Source**

Supercontinuum light can be best described as ‘broad as a lamp, bright as a laser’. Incandescent and fluorescent lamps, such as those made from tungsten halogens or xenon, provide a very broad spectrum, typically 400 nm to 1700 nm, but the intensity is limited to the quality of the filament or the efficiency of the gas excitation. Furthermore, as the light is not spatially coherent, coupling the light into the fiber is a challenging affair, resulting in a low-power, and low brightness source with mediocre beam quality. Lasers on the other hand have high spatial coherence and very high brightness, which enables optimum coupling to a fiber and outstanding single-mode beam quality. However, lasers are usually monochromatic, and thus if more than one wavelength is required extra lasers a specific wavelengths are required to cover a broad spectrum. A supercontinuum source bridges this gap, providing an ultra-broadband white-light spectrum but with single mode beam characteristics and excellent pointing stability and the brightness of a laser.

#### **4.2 Applications of Supercontinuum Source**

1. The most straight-forward application for supercontinuum sources is a replacement for the common, and often tungsten-based, white-light sources used

in many characterizations setups like interferometer-based dispersion measurements, broadband attenuation characterization and numerous spectroscopy and microscopy setups. The major disadvantage to all incandescent sources is the low brightness, which is determined by the filament temperature (black body radiation). Sources with higher output power utilize larger filaments with same brightness and the power that can be coupled to a single-mode fiber is therefore the same. Moreover, the efficiency of light coupling from the filament to the fiber is generally low, resulting in only a small fraction of the light being available in the fiber. The supercontinuum source solves both the brightness and coupling issue and it is possible to create sources with the spectral width of a tungsten lamp and the intensity of a laser.

2. One of the most important applications of the SC sources is the optical coherence tomography (OCT). OCT requires has smooth spectra that variations of less than 10 dB since spectral gap can affect the image quality and the measurement precision. The spectral region between 1200 and 1500 nm is particularly important for the OCT as they provide high penetration depth in the biological tissue. The SC source obtained in PCFs with slow pulses around 1060 nm are particularly promising for the OCT, because the large flat spectrum mainly generated by SRS is very stable and can be filtered in order to select the desired wavelength range. Furthermore, high-output power density enables the ability to measure reflections from very weak reflectors.
3. One of the most important applications of SC to the field of telecommunications is the design of multi-wavelength sources for ultra-broadband wavelength-division-multiplexed (WDM) systems based on spectral slicing of SC generated by a single laser. By slicing the broad spectrum of the supercontinuum into hundreds of channels, and utilizing an optical time domain multiplexing (OTDM) technique for each channel, transmission bandwidth of terahertz can be achieved [101].
4. Another applied field of SC is pulse compression and short pulse generation. When a fiber is pumped in the anomalous dispersion regime with a narrow-spectrum laser, a series of short, low intensity solitons generated. On the other hand, nonlinear temporal compression has been for a long time a well-known technique for generating ultra-short pulses [102]. In this technique, the spectrum

of the signal is first nonlinearly broadened, and the chirp is then eliminated by a dispersion-compensating element.

### **4.3 Physics of Spectral Broadening**

The techniques to generate supercontinuum in optical fibers are roughly divided into two categories. One is spectrum broadening by the pulse compression using soliton effects in an anomalous dispersion fiber. Another is the spectrum broadening by the accumulation of frequency chirping caused by optical Kerr effects in a normal dispersion fiber.

The most common way to generate broadband SC in PCF using femtosecond pump pulses is to select a PCF with a zero dispersion wavelength (ZDW) which falls just below the laser wavelength. Because the dispersion is anomalous at the pump wavelength, the supercontinuum is dominated by soliton dynamics i.e. soliton-related propagation effects. The most importance of these in the initial stages is the soliton fission process, whereby a pulse with sufficient peak power to constitute a higher-order soliton is perturbed and breaks up into a series of lower-amplitude sub-pulses. Each of these pulses is, in fact, a constituent fundamental soliton. A higher-order soliton is a particular class of solution of the non-linear Schrodinger equation (NLSE) representing a bound state of  $N$  fundamental solitons [12, 103]. Such solutions propagate in a complex manner consisting of both spectral and temporal variations. The process is then followed by the Raman shifting of solitons and the associated generation of dispersive waves from each ejected fundamental soliton due to the effect of higher-order dispersion. It is the phase-matching condition that determines the spectral position of dispersive wave. Afterwards, the soliton self-frequency shift extends the broadening to the infrared side of the spectrum while trapped dispersive waves into short-wavelength region. Recent numerical studies by Travers et al. [103, 104], and Mussot et al. [105] have provided further insight into this dynamics, and explicitly demonstrated that four-wave mixing and/or Raman scattering dominate the initial steps of SC generation with long pulses, leading to symmetrical broadening of the pump spectrum. Subsequent soliton formation and breakup which are subject to the peak power and dispersion values takes place, and Raman self-scattering can then lead to a long-wavelength soliton continuum. However, soliton dynamics are extremely sensitive to pump pulse fluctuations. Small fluctuations in the pump amplitude or phase from shot to shot can cause significant fluctuations in

spectral intensity and phase of the resulting supercontinuum. These fluctuations are averaged out over thousands of pulses when viewing the spectrum on a spectrometer, so the spectrum may appear smooth, but in reality there may be large deviations from this average in each pulse. This fluctuation in spectral intensity and phase translates into loss of spectral coherence. Spatial coherence is usually found to be very high, particularly when the source involves a single-mode fiber. On the other hand, the high spectral bandwidth suggests the very low nature of the temporal coherence [106].

## 4.4 Mechanisms responsible for Supercontinuum Generation

The physical processes behind the supercontinuum generation in fibers can be very complex, depending particularly upon the chromatic dispersion and length of the fiber which we are using, the pulse duration, the initial peak power and wavelength of the pump. When the femtosecond pulses are used, the spectral broadening can be caused by self-phase modulation. In the dispersion the combination of self-phase modulation and dispersion can lead to Soliton solution dynamics, including the split-up of higher-order solitons into large number of multiple fundamental solitons (soliton fission). For pumping with picoseconds, ultra shot or nanosecond pulses, Raman scattering and four-wave mixing can be important. Supercontinuum generation is even possible with continuous-wave beams, when using small laser beams in long fibers; Raman scattering and four-wave mixing are very important in that regime.

### 4.4.1 Self-Phase Modulation

An interesting manifestation of the intensity dependence of the refractive index in nonlinear optical media occurs through self-phase modulation (SPM), a phenomenon that leads to spectral broadening of optical pulse [12] arising from the intensity dependent refractive index.

$$n = n_0 + n_2 I \quad (4.1)$$

where  $n_0$  the linear refractive index and  $n_2$  is the nonlinear index. The higher intensity portions of the optical pulse gives a higher refractive index when compared with that of the lower intensity portions when it travels through the fiber. In fact time varying signal intensity produces a time varying refractive index in the medium that has an intensity

dependent refractive index. The leading edge will experience a positive refractive index gradient ( $dn/dt$ ) and trailing edge a negative index gradient ( $-dn/dt$ ). This temporal variation in refractive index changes results in a temporally varying phase change. Since this nonlinear phase change is self-induced and the nonlinear phenomenon responsible for it called as the self-phase modulation (SPM). Different parts of the pulse undergo different phase shift because of the intensity dependence of phase fluctuations. This results in the frequency chirping. The rising edge of the pulse finds that the frequency shift in the upper side whereas the trailing edge of the pulse finds that the frequency shift in the lower side. Hence the effect of the self-phase modulation is to broaden the spectrum of the pulse, keeping the temporal shape (time domain) unchanged. The broadening of the spectrum without any change in temporal distribution in case of self-phase modulation while in case of dispersion, there is broadening of the pulse in time domain and spectral contents are unaltered. In other words the SPM by itself leads only to chirping, regardless of the pulse shape. It is the dispersion that is responsible for pulse broadening. The SPM induced chirp modifies the pulse broadening effect of dispersion after propagating a distance  $L$  can be written as follows [12].

$$\Phi_{NL}^{SPM} = \frac{2\pi L}{\lambda} n_2 I(t) \quad (4.2)$$

The corresponding phase shift is [12]

$$\delta_{NL}^{SPM} = -\frac{d}{dt}(\Phi_{NL}^{SPM}) = -\frac{2\pi L}{\lambda} n_2 \frac{dI(t)}{dt} \quad (4.3)$$

## 4.4.2 Soliton formation

### 4.4.2.1 Fundamental Soliton

Soliton refers to the special kinds of wave packets that can propagate undistorted over long distances i.e. invariance along fiber length or follow a periodic evolution pattern. A fundamental soliton is an optical pulse which can propagate in a dispersive medium with a constant shape of the temporal intensity profile without any temporal broadening as is usually caused by dispersion. There are four parameters determine the nature of soliton. They are amplitude, frequency, position, and phase. In case of fundamental (first-order soliton) soliton the phase term can be dropped because a constant absolute phase has no physical significance. If a hyperbolic secant pulse, whose width  $T_0$  and the peak power  $P_0$

is launched inside an ideal lossless fiber, the pulse will propagate undistorted without change in shape for arbitrarily long distance. It is the feature of the fundamental soliton that makes them attractive for optical communication system [12]. The peak power  $P_0$  required to support the fundamental soliton is

$$P_0 = \frac{|\beta_2|}{\gamma T_0^2} \approx \frac{3.11|\beta_2|}{\gamma T_{FWHM}^2} \quad (4.4)$$

where the full width half maximum (FWHM) of the soliton is defined using  $T_{FWHM} = 1.76T_0$ , and  $\beta_2$  is the GVD parameter.

#### 4.4.2.2 Higher-Order Soliton

Whereas fundamental solitons are usually fairly stable, higher-order solitons can break up into fundamental solitons under the influence of various effects, such as higher-order dispersion, Raman scattering etc. As the pulse propagate along the longitudinal direction (z-direction) of the fiber, it first contracts to a fraction of its original width, splits into two distinct pulses after some interval, and finally merges again to recover the shape at the end of the soliton period. The temporal and spectral changes result from an interplay between the SPM and GVD effects. The SPM generates a frequency chirp such that the leading edge of the pulse is red-shifted (a spectral shift towards higher wavelengths i.e. lower energy and frequency), while its trailing edge is blue shifted (a spectral shift towards lower wavelengths i.e. higher energy and frequency) from the central frequency.

Anomalous GVD contracts the pulse as the pulse if positively chirped. Only the central portion of the pulse contracts because the chirp is nearly linear only over that part. However, as a result of substantial increase in the pulse intensity near the central part of the pulse, the spectrum changes significantly. Newly generated frequencies move towards the pulse center, so the pulse is compressed [12, 107]. In the case of a fundamental soliton ( $N=1$ ), GVD and SPM balance each other in such a way that neither the pulse shape nor the pulse spectrum changes along the fiber length. The soliton order is given by  $N^2 = L_D/L_{NL}$  where  $L_D$  and  $L_{NL}$  are the characteristic dispersive and nonlinear length scales. A fundamental soliton has soliton order  $N = 1$ , the dispersion length and nonlinear length are equal.

In the case of higher-order solitons, SPM dominates initially but GVD soon catches up and leads to pulse contraction. Higher order solitons have  $N > 1$ , and in that case SPM

and dispersion are not exactly balanced. Unlike fundamental solitons they do not maintain their temporal and spectral shape during propagation, and instead periodically split and recombine over a distance known as the soliton period  $z_0 = (\pi/2)L_D$ . The splitting of higher-order solitons is known as soliton fission. Such soliton fission process plays a crucial role in the process of supercontinuum generation in PCFs.

### 4.4.3 Stimulated Raman scattering

Stimulated Raman scattering (SRS) is an important nonlinear process that can turn optical fibers into broadband Raman amplifiers and tunable Raman lasers. It can also severely limit the performance of multichannel lightwave systems by transferring energy from one channel to the neighboring channels. Stimulated Raman Scattering is a photon-phonon interaction. The energy from an intense pump beam is shifted to lower frequencies (Stokes waves) through scattering from vibrational modes of the material molecules. Shifting of energy to higher frequencies (anti-Stokes waves) can also occur but is less efficient. It can be described quantum mechanically as scattering of a photon of energy  $\hbar\omega_p$  by a molecule to a lower frequency photon with energy  $\hbar\omega_{st}$ .

$$2\omega_p \rightarrow \omega_{as} + \omega_{st} \quad (4.5)$$

where  $\omega_p$ ,  $\omega_{as}$  and  $\omega_{st}$  being the frequency of the pump, anti-Stokes, and Stokes photons, respectively. In silica glass Raman scattering can occur over a broad range of frequency shifts, because the amorphous nature of the material means the molecular vibrational frequencies form a continuum.

### 4.4.4 Four wave-mixing (FWM)

In the anomalous GVD region of the material, a nonlinear effect called four wave mixing (FWM) can occur. It is the general name for many different processes arising from the interplay of dispersion and third order nonlinearity where frequency components  $\omega_1$ ,  $\omega_2$ , and  $\omega_3$  existing in the pulse interaction with each other generating new frequencies  $\omega_4 = \pm\omega_1 \pm \omega_2 \pm \omega_3$ . Four-wave mixing processes are important in supercontinuum generation. One special case of four-wave mixing processes is modulation instability (MI) [12], where Waves with frequencies  $\omega$  and  $\omega \pm \phi$  interact producing spectral sidebands. Temporarily this corresponds to a break up of wave-form into train of pulses.

#### 4.4.5 Higher Order Dispersion Parameter

It's well known that dispersion has a major impact in the performance of optical fiber systems, particularly when femtosecond pulses are propagated in the fiber core. For such ultrashort pulses, it has been recognized that the exact evaluation of the higher order dispersion coefficients is very important for the correct modeling. The dispersion coefficient is related to the refractive index and group velocity,  $v_g$  through the relation [107]:

$$D(\lambda) = \frac{d\beta_1}{d\lambda} \quad (4.6)$$

where  $\beta_1 = n_g/c$ , is the inverse group velocity,  $n_g$  the group index,  $\lambda$  the wavelength, and  $c$  the speed of light. It is known that [12]

$$\beta_1 = \frac{1}{v_g} = \frac{n_g}{c} = \frac{1}{c} \left( n + \omega \frac{dn}{d\omega} \right) \quad (4.7)$$

now,

$$\frac{dn}{d\omega} = \frac{dn}{d\lambda} \frac{d\lambda}{d\omega} \quad (4.8)$$

and

$$\omega = \frac{2\pi c}{\lambda}$$

therefore,

$$\frac{d\omega}{d\lambda} = \frac{d}{d\lambda} \left( \frac{2\pi c}{\lambda} \right) = -\frac{2\pi c}{\lambda^2} \quad (4.9)$$

Using (4.9) in Equation (4.8)

$$\frac{dn}{d\omega} = \frac{dn}{d\lambda} \frac{d\lambda}{d\omega} = \frac{dn}{d\lambda} \left( -\frac{\lambda^2}{2\pi c} \right) = -\frac{\lambda^2}{2\pi c} \frac{dn}{d\lambda} \quad (4.10)$$

then from Equation (4.7), we get,

$$\beta_1 = \frac{1}{c} \left( n + \omega \frac{dn}{d\omega} \right) = \frac{1}{c} \left( n - \omega \frac{\lambda^2}{2\pi c} \frac{dn}{d\lambda} \right) \quad (4.11)$$

Thus, using (4.11) in (4.6) we have,

$$D(\lambda) = \frac{d\beta_1}{d\lambda} = \frac{d}{d\lambda} \left[ \frac{1}{c} \left( n - \omega \frac{\lambda^2}{2\pi c} \frac{dn}{d\lambda} \right) \right] = \frac{1}{c} \left[ \frac{d}{d\lambda} \left( n - \lambda \frac{dn}{d\lambda} \right) \right]$$



$$\begin{aligned}
&= \frac{1}{c} \left[ \frac{dn}{d\lambda} - \frac{d}{d\lambda} \left( \lambda \frac{dn}{d\lambda} \right) \right] \\
&= \frac{1}{c} \left[ \frac{dn}{d\lambda} - \left( \lambda \frac{d^2n}{d\lambda^2} + \frac{dn}{d\lambda} \right) \right] \\
&= \frac{1}{c} \left[ \frac{dn}{d\lambda} - \lambda \frac{d^2n}{d\lambda^2} - \frac{dn}{d\lambda} \right] \\
D(\lambda) &= \frac{d\beta_1}{d\lambda} = -\frac{\lambda}{c} \frac{d^2n}{d\lambda^2} \tag{4.12}
\end{aligned}$$

Equation 4.12 is strictly valid for a material medium; however, it is a common approach to substitute the material refractive index by the effective index for a non-homogeneous medium to calculate dispersion parameter. However, even if the material dispersion is taken into account during the calculation of the effective index at each wavelength, different results are obtained if the dispersion coefficient is calculated by substituting the material index by the effective index, as expressed by the formula [90]:

$$D(\lambda) = -\frac{\lambda}{c} \frac{d^2 \text{Re}(n_{eff})}{d\lambda^2} \tag{4.13}$$

where  $\text{Re}[n_{eff}]$  is the real part of the effective refractive index. The dispersion obtained using Equation 4.13 is comprised of both material and waveguide dispersion since Sellmeier's equation is considered while calculating of the effective refractive index of the propagating mode.

In this work, using Equation 4.13, we calculate the dispersion and obtained the zero dispersion wavelength, and used these calculated values to obtain higher order dispersion coefficients that are used in the nonlinear Schrödinger equation for the simulation of the supercontinuum evolution. After calculating the dispersion curve, the group velocity dispersion parameter and higher order dispersion terms, we use the calculated data to model the supercontinuum generation using the generalized nonlinear Schrödinger equation (GNLS). Since the inclusion of higher-order derivatives coming from the Taylor expansion of the propagation constant may lead to instabilities for some particular choice of the fiber and pulse parameters, we also investigated how the inclusion of higher order dispersion coefficients affect the evolution of the supercontinuum spectrum. In case of propagation of ultra-short pulses higher order dispersion terms are also needed in order to have a more accurate model, in particular, those concerning with supercontinuum generation.

The higher order dispersion terms are calculated from [12, 107]:

$$\beta_n = \frac{d\beta_{n-1}}{d\omega} \quad (4.14)$$

Second order dispersion can be calculated using Equation 4.14:

$$\begin{aligned} \beta_2 &= \frac{d\beta_1}{d\omega} = \frac{d}{d\omega} \left[ \frac{1}{c} \left( n + \omega \frac{dn}{d\omega} \right) \right] \\ &= \frac{1}{c} \left( \frac{dn}{d\omega} + \omega \frac{d^2n}{d\omega^2} + \frac{dn}{d\omega} \right) \\ &= \frac{1}{c} \left( 2 \frac{dn}{d\omega} + \omega \frac{d^2n}{d\omega^2} \right) \end{aligned}$$

Using Equation 4.10:

$$\begin{aligned} &= \frac{1}{c} \left( -2 \frac{\lambda^2}{2\pi c} \frac{dn}{d\lambda} + \omega \left( -\frac{\lambda^2}{2\pi c} \frac{dn}{d\lambda} \right)^2 \right) \\ &= \frac{1}{c} \left( -2 \frac{\lambda^2}{2\pi c} \frac{dn}{d\lambda} + \omega \frac{\lambda^4}{(2\pi c)^2} \frac{d^2n}{d\lambda^2} \right) \\ &= \frac{1}{c} \left( -2 \frac{\lambda^2}{2\pi c} \frac{dn}{d\lambda} + \frac{\lambda^3}{2\pi c} \frac{d^2n}{d\lambda^2} \right) \\ &= -2 \frac{\lambda^2}{2\pi c^2} \frac{dn}{d\lambda} + \frac{\lambda^3}{2\pi c^2} \frac{d^2n}{d\lambda^2} \\ \beta_2 &= -\frac{\lambda^2}{2\pi c^2} \left( 2 \frac{dn}{d\lambda} - \lambda \frac{d^2n}{d\lambda^2} \right) \quad (4.15) \end{aligned}$$

Similarly, the third order dispersion (TOD) can be obtained as [108]

$$\begin{aligned} \beta_3 &= \frac{d\beta_2}{d\omega} = \frac{d}{d\omega} \left[ \frac{1}{c} \left( 2 \frac{dn}{d\omega} + \omega \frac{d^2n}{d\omega^2} \right) \right] \\ &= \frac{1}{c} \left[ \frac{d}{d\omega} \left( 2 \frac{dn}{d\omega} + \omega \frac{d^2n}{d\omega^2} \right) \right] \\ &= \frac{1}{c} \left( 2 \frac{d^2n}{d\omega^2} + \omega \frac{d^3n}{d\omega^3} + \frac{d^2n}{d\omega^2} \right) \\ &= \frac{1}{c} \left( 3 \frac{d^2n}{d\omega^2} + \omega \frac{d^3n}{d\omega^3} \right) \end{aligned}$$

Using Equation 4.10

$$\begin{aligned}
&= \frac{1}{c} \left[ 3 \left( -\frac{\lambda^2}{2\pi c} \frac{dn}{d\lambda} \right)^2 + \omega \left( -\frac{\lambda^2}{2\pi c} \frac{dn}{d\lambda} \right)^3 \right] \\
&= \frac{1}{c} \left[ 3 \frac{\lambda^4}{4\pi^2 c^2} \frac{d^2 n}{d\lambda^2} - \omega \frac{\lambda^6}{8\pi^3 c^3} \frac{d^3 n}{d\lambda^3} \right] \\
&= \frac{1}{c} \left[ 3 \frac{\lambda^4}{4\pi^2 c^2} \frac{d^2 n}{d\lambda^2} - \frac{\lambda^5}{4\pi^2 c^2} \frac{d^3 n}{d\lambda^3} \right] \\
\beta_3 &= -\frac{\lambda^4}{4\pi^2 c^3} \left[ -3 \frac{d^2 n}{d\lambda^2} + \lambda \frac{d^3 n}{d\lambda^3} \right] \tag{4.16}
\end{aligned}$$

The terms  $\beta_4$  and higher orders can be likewise determined simply by taking the first derivative of the immediate previous value of  $\beta$  with respect to  $\omega$ .

#### 4.4.6 Nonlinearity Coefficient

Nonlinear coefficient of PCF represents very important parameter during SCG analysis. Nonlinear coefficient ( $\gamma$ ) is directly proportional to nonlinear refractive index ( $n_2$ ) and inversely proportional to the effective area ( $A_{eff}$ ). Non-linear coefficient of the analyzed PCF is evaluated based on the following equations [81]:

$$\gamma = \frac{2\pi n_2}{\lambda A_{eff}} \tag{4.17}$$

where  $\lambda$  is the pumping wavelength and it is taken as 1100 nm,  $n_2$  is the nonlinear refractive index and it is  $2.7 \times 10^{-20}$  m<sup>2</sup>/W for silica, and for polymer Topas  $15 \times 10^{-20}$  m<sup>2</sup>/W [109]. The effective mode area is expressed as [78]

$$A_{eff} = \frac{(\iint |E|^2 dx dy)^2}{\iint |E|^4 dx dy} \tag{4.18}$$

where  $E$  is the electric field amplitude. The integration is done not only over the core area, but over the whole cross-sectional domain. An important consequence of a small effective mode area is that the optical intensities for a given power level are high, so that nonlinearities become important. Also, small mode areas are usually the consequence of strong guiding, where bend losses and other effects of external disturbances are weak. The non-linearity can be achieved in any fiber is limited by its mode confinement. Significant higher values of  $\gamma$  can be achieved by combining tight mode confinement with the use of non-silica glasses with greater intrinsic material non-linearity coefficients than silica.

## 4.5 Numerical Model of Supercontinuum

The supercontinuum generation process can be studied by solving the generalized nonlinear Schrodinger equation (GNLSE). It is important to incorporate dispersive effects and Raman scattering as accurately as possible. After generalizing it further including higher order dispersion parameters, the resulting equation can be expressed as [38]

$$\begin{aligned} \frac{\partial A(z, t)}{\partial z} + \frac{\alpha}{2} A(z, t) - \sum_{k \geq 2} i^{k+1} \frac{\beta_k}{k!} \frac{\partial^k A(z, t)}{\partial t^k} \\ = i\gamma \left( 1 + \frac{i}{\omega_0} \frac{\partial}{\partial t} \right) \\ \times \left[ A(z, t) \left( \int_{-\infty}^{\infty} R(t') |A(z, t - t')|^2 dt' \right) \right] \end{aligned} \quad (4.19)$$

where  $A(z, t)$  is the slowly varying envelope of the electric field of the optical pulse,  $\alpha$  represents the photonic crystal fiber loss which can be neglected since only a short length of PCF is used,  $\beta_k$  are the fiber dispersion coefficients at carrier frequency (center frequency)  $\omega_0$ , and  $\gamma$  is the nonlinear coefficient and  $A_{eff}$  is the fiber effective area.  $k$  represents the order up to which dispersive effects are included. In this work we determine dispersion parameters from  $\beta_2$  to  $\beta_{12}$  at pumping wavelength. The nonlinear response function can be written as [38]

$$R(t) = (1 - f_R) \delta(t) + f_R h_R(t) \quad (4.20)$$

which includes both instantaneous electronic and delayed Raman contributions, with  $f_R$  is the experimentally evaluated contribution of the molecular resonances to the nonlinear refractive index  $n_2$  known as fractional Raman contribution and  $h_R(t)$  is the analytical form of response function termed as the delayed Raman response function and can be expressed as [38]

$$h_R(t) = \frac{\tau_1^2 + \tau_2^2}{\tau_1 \tau_2^2} e^{-\frac{t}{\tau_2}} \sin \frac{t}{\tau_1} \quad (4.21)$$

$\tau_1$  and  $\tau_2$  are Raman period and Raman lifetime and the inverse of these parameters give the phonon frequency and bandwidth of the Lorentzian line, respectively. As an example, parameters ( $\tau_1, \tau_2$ , and  $f_R$ ) of Silica PCF are summarized in Table 4.1.

**Table 4.1**

Parameters of Silica PCF [12], [38]

|          |         |
|----------|---------|
| $\tau_1$ | 12.2 fs |
| $\tau_2$ | 32 fs   |
| $f_R$    | 0.18    |

Supercontinuum generation dynamics can be roughly divided in four categories depending on the properties of the input pulse [12]. The first distinction is between pumping in the anomalous or normal GVD regime of the fiber. Typically the pulses are created in the anomalous GVD regime since it produces the broadest bandwidth [12]. The second distinction is between short and long input pulses. In this context, short means shorter than a picosecond pulse and long pulses can be in the range of picoseconds to nanoseconds or even a continuous wave.

If we consider the anomalous GVD regime and short pump pulses, the spectral broadening arises from soliton dynamics. If  $N \geq 1$ , the high-order solitons are first broadened spectrally and compressed temporally. Then perturbations such as high-order dispersion and stimulated Raman scattering break the pulse into  $N$  distinct solitons. Similarly, a dispersive wave is generated through resonant transfer of energy across the zero-dispersion wavelength. As the fundamental solitons propagate, they shift to longer wavelengths through the Raman soliton self-frequency shift. The bandwidth of the pulse can still be broadened when the generated Raman soliton and dispersive waves couple through cross-phase modulation, which results in additional frequency components. Regarding pulses in the anomalous dispersion regime but with longer duration, the dominating effect in the pulse broadening is modulation instability which corresponds to the generation of spectral four-wave mixing parametric sidebands. The modulation instability breaks the initial pulse into many temporal sub-pulses. After that, the spectral broadening happens in the same way as with the fundamental solitons. However, if the pump pulse is too far in the anomalous GVD regime, the spectral broadening is reduced because the modulation instability dynamics do not generate wide enough bandwidth to seed dispersive wave transfer into the normal GVD regime.

For short subpicosecond pulses in the normal GVD regime, the spectral broadening arises from the interaction of self-phase modulation and the normal GVD of

the fiber. That process leads to significant temporal broadening and thus a decrease of the peak power of the pulse, and therefore nonlinear effects only occur at the first few centimeters of propagation in the fiber. However, if the pump pulse is near the anomalous GVD regime, spectral content can be transferred into the anomalous region after the initial broadening. Following that the broadening is affected by soliton dynamics. Longer pump pulses and continuous radiation in the normal GVD regime broaden mostly through four-wave mixing and Raman scattering. The pumping wavelength affects the emphasis of these two mechanisms. Near the zero-dispersion wavelength four-wave mixing becomes more important, and if the broadening overlaps with the zero-dispersion wavelength, soliton dynamics can again contribute to the spectral broadening. The main mechanisms in the supercontinuum pulse creation with different types of input pulses are summarized in Table 4.2.

**Table 4.2**

Main processes affecting the supercontinuum generation with short and long input pulses in the normal and anomalous GVD regimes

| GVD       | Pulse | Processes                                     |
|-----------|-------|---|
| anomalous | Short | Soliton dynamics, dispersive waves            |
| anomalous | long  | Modulation Instability (MI), Soliton dynamics |
| normal    | Short | SPM, Soliton dynamics                         |
| normal    | long  | FWM, Raman scattering, Soliton dynamics       |

In the simulations used in this thesis, the input pulses are of the form of

$$A(0, t) = N\sqrt{P_0} \operatorname{sech}\left(\frac{t}{T_0}\right)$$

where  $P_0$  is the peak power of the input pulse and  $T_0$  is the pulse width related to the full width at the half maximum of the pulse through  $T_{FWHM}/1.763$ . In addition to  $P_0$  and  $T_0$ , the propagation distance in the fiber has been varied. The order of the solitons

$$N = \frac{\gamma P_0 T_0^2}{|\beta_2|}$$

is determined by both fiber and pulse parameters. If  $N > 1$ , the higher order soliton dynamics determine the pulse broadening [12].

The photonic crystal fiber loss which can be neglected since only a short length of PCF is used. Thus we have:

$$\begin{aligned}
\frac{\partial A(z, t)}{\partial z} - \sum_{k \geq 2} i^{k+1} \frac{\beta_k}{k!} \frac{\partial^k A(z, t)}{\partial t^k} \\
= i\gamma \left( 1 + \frac{i}{\omega_0} \frac{\partial}{\partial t} \right) \\
\times \left[ A(z, t) \left( \int_{-\infty}^{\infty} R(t') |A(z, t - t')|^2 dt' \right) \right] \quad (4.22)
\end{aligned}$$

## 4.6 Solution of Generalized Nonlinear Schrodinger Equation Using Split Step Fourier Method

The GNLS Equation 4.22 is a nonlinear partial differential equation that does not generally have any analytic solutions except for some specific case. A numerical approach is therefore often necessary for an understanding of the nonlinear effects in optical fibers. Split-Step Fourier Method is an extensive way to solve the pulse propagation problem in nonlinear dispersive media. This method is based around separating the dispersive and nonlinear components of the equation from one another. This assumes that over a very small distance these components may be assumed to be independent. So the nonlinear Schrödinger equation, including higher order dispersion, self-steepening, and Raman scattering, is expressed as:

$$\begin{aligned}
\frac{\partial A(z, t)}{\partial z} = \sum_{k \geq 2} i^{k+1} \frac{\beta_k}{k!} \frac{\partial^k A(z, t)}{\partial t^k} + i\gamma \left( 1 + \frac{i}{\omega_0} \frac{\partial}{\partial t} \right) \\
\times \left[ A(z, t) \left( \int_{-\infty}^{\infty} R(t') |A(z, t - t')|^2 dt' \right) \right] \quad (4.23)
\end{aligned}$$

Writing the Eq. (4.23) in the following form:

$$\frac{\partial A(z, t)}{\partial z} = (\widehat{D} + \widehat{N})A(z, t) \quad (4.24)$$

where

$$\widehat{D} = \sum_{k \geq 2} i^{k+1} \frac{\beta_k}{k!} \frac{\partial^k A(z, t)}{\partial t^k} \quad (4.25)$$

$$\widehat{N} = \frac{i}{A(z, t)} \gamma \left( 1 + \frac{i}{\omega_0} \frac{\partial}{\partial t} \right) \times \left[ A(z, t) \left( \int_{-\infty}^{\infty} R(t') |A(z, t - t')|^2 dt' \right) \right] \quad (4.26)$$

$\widehat{D}$  is a differential operator that accounts for dispersion and absorption and  $\widehat{N}$  is a nonlinear operator that governs the effect of fiber nonlinearities on pulse propagation. In

general, dispersion and nonlinearity act together along the fiber length. But, following approximation is made in the split-step Fourier method: Within a small propagation distance, the dispersive and nonlinear effects act on the pulse independently. In the simulations presented in this work, we take three steps to describe the pulse propagation over one segment from  $z$  to  $z + h$ . In the first step, dispersion effects act alone from  $z$  to  $z + h/2$  and  $\hat{N} = 0$ ; in the second step, the nonlinear effects are included in the middle of the segment, and they act alone from  $z$  to  $z + h$ ; in the third step, dispersion effects act alone from  $z + h/2$  to  $z + h$ . Mathematically this procedure can be expressed by Eq. (4.27):

$$A(z + h, t) \approx \exp\left(\frac{h}{2}\hat{D}\right) \exp\left(\int_z^{z+h} \hat{N}(z') dz'\right) \exp\left(\frac{h}{2}\hat{D}\right) A(z, t) \quad (4.27)$$

Under further simplification of the integral, Eq. (4.27) is replaced by

$$A(z + h, t) \approx \exp\left(\frac{h}{2}\hat{D}\right) \exp\left(\frac{h}{2}[\hat{N}(z) + \hat{N}(z + h)]\right) \exp\left(\frac{h}{2}\hat{D}\right) A(z, t) \quad (4.28)$$

To evaluate the exponential operator  $\exp\left(\frac{h}{2}\hat{D}\right)$  we apply the following formula:

$$\exp\left(\frac{h}{2}\hat{D}\right) A(z, h) = F_T^{-1} \left\{ \exp\left[\frac{h}{2}D(-i\omega)\right] F_T[A(z, h)] \right\} \quad (4.29)$$

where  $F_T$  stands for Fourier-transform operation,  $D(-i\omega)$  is the Fourier transform of  $\hat{D}$ , and  $\omega$  is the frequency in the Fourier domain. Using the same method, we obtain the electric field  $A(z + h, t)$  at propagation distance  $z + h$  as Eq. (4.30)

$$A(z + h, t) = F_T^{-1} \left\{ \exp\left[\frac{h}{2}D(-i\omega)\right] F_T[X(z, h)] \right\} \quad (4.30)$$

where

$$X(z, h) = \exp\left(\frac{h}{2}[\hat{N}(z) + \hat{N}(z + h)]\right) F_T^{-1} \left\{ \exp\left[\frac{h}{2}D(-i\omega)\right] F_T[A(z, h)] \right\} \quad (4.31)$$

Two difficulties arise when we evaluate the electric field  $A(z + h, t)$ . First,  $\hat{N}(z + h)$  in the expression of  $X(z, h)$  is unknown, since it is a function of electric field  $A(z + h, t)$ . Second, the integral term in Eq. (4.26), which represents the delayed Raman scattering, is hard to evaluate directly. To solve the first problem, we employ an iterative method  $\hat{N}(z + h)$  in the expression of  $X(z, h)$  is initially replaced by  $\hat{N}(h)$  to estimate  $A(z + h, t)$ , which can be used to evaluate  $\hat{N}(z + h)$ . Knowing the value of  $\hat{N}(z + h)$ , we can calculate the new value of  $A(z + h, t)$ . The second problem can be settled by using convolution theory. The integral term in Eq. (4.26) is therefore expressed as:



$$\begin{aligned}
\int_{-\infty}^{\infty} R(t')|A(z, t - t')|^2 dt' &= \int_0^t R(t')|A(z, t - t')|^2 dt' \\
&= R(t) * |A(z, t)|^2 \\
&= F_T^{-1}\{F_T[R(t)].F_T[|A(z, t)|^2]\}
\end{aligned}$$

where  $R(t) * |A(z, t)|^2$  is convolution of  $R(t)$  ,  $|A(z, t)|^2$  called Raman convolution.

## Chapter 5

# SUPERCONTINUUM GENERATION IN HYBRID POLYMER PCF

### 5.1 Design of Hybrid Polymer PCF

Though the combination of glasses with polymer photonic crystal fibers (PCFs) is a difficult and challenging task due to their different thermo-mechanical material properties [116], in this work we, make an endeavor for the supercontinuum generation in polymer photonic crystal fiber based on simulation technique for the first time to the best of knowledge. We report a hybrid polymer PCF with integrated silica glass layers of few nanometers at the outer surface of the air-holes. The integration of silica glass with polymer makes the polymer PCF nonlinear and provides a possibility to study the nonlinear pulse propagation in fiber and also to generate supercontinuum pulse.

We investigated supercontinuum generation using a hexagonal PCF structure. Figure below illustrates the cross sectional view of the hybrid PCF (H-PCF). It contains 4 rings, each having  $6 \times n$  number of air holes (where  $n=1, 2, 3, 4$  introduces number of rings).

The parameters used for the PCF are: pitch  $\Lambda = 2.1 \mu\text{m}$ , and different  $d/\Lambda$  ratios i.e. 0.5, 0.6, and 0.7 that give air hole diameters  $d=1.05 \mu\text{m}$ ,  $1.26 \mu\text{m}$ , and  $1.47 \mu\text{m}$  respectively. It will be later clear that, with the increase in filling factor i.e.  $d/\Lambda$  the mode confinement enhanced and hence modal effective area decrease significantly and corresponding nonlinearity parameter increased. Since highly nonlinear medium is the prime requirement for supercontinuum generation, we make the selection of  $d/\Lambda$  ratio such that maximum nonlinearity is achieved. For this case, the maximum nonlinearity can be obtained selecting  $d/\Lambda$  ratios as 0.7 and for this specific ratio diameter of all air holes in different rings kept equal throughout the simulation process for supercontinuum generation, which makes the design simple and will reduce fabrication complexity.

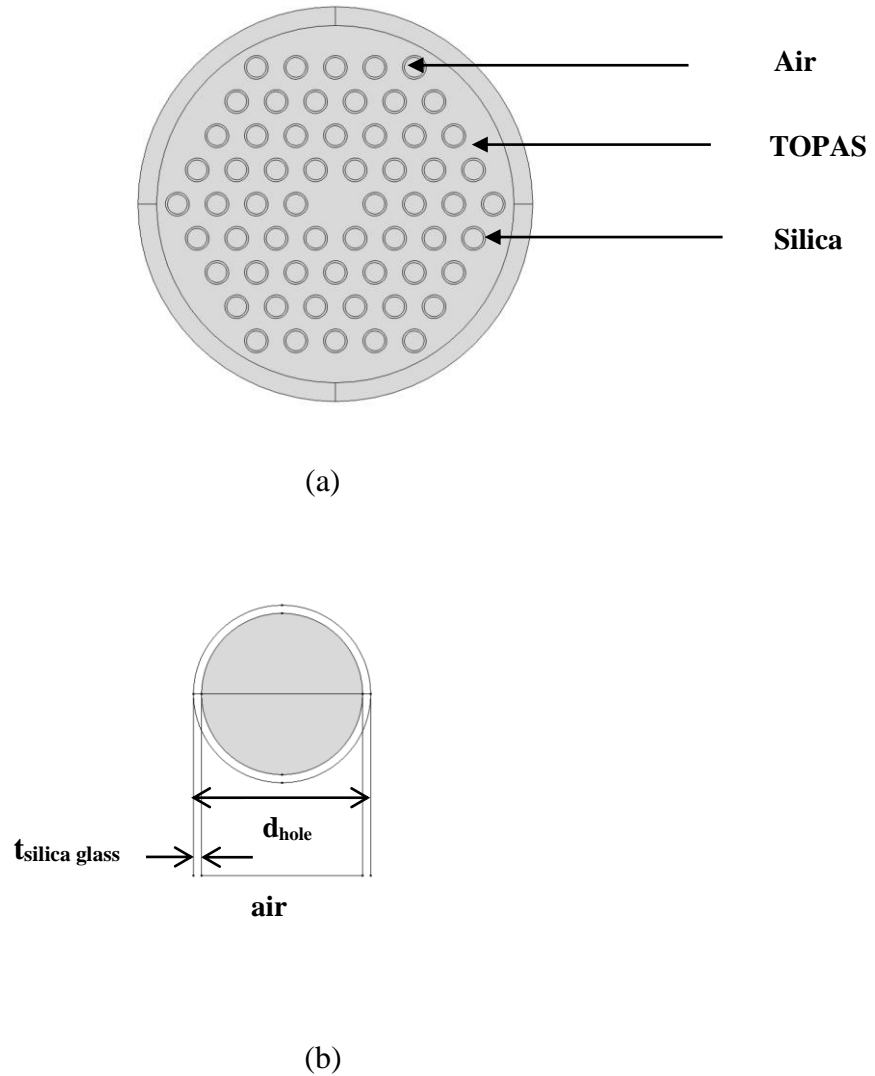


**Fig. 5.1** (a) Cross sectional view of hybrid polymer PCF (HP-PCF), (b) A single air hole with silica glass layer.

## 5.2 Results and Discussion

For the proposed hybrid polymer PCF structure wavelength dependent dispersion, corresponding zero dispersion wavelength, effective mode area, nonlinearity parameter, and higher order dispersion coefficients are calculated. From the dispersion curve shown in Figure 5.2, it can be seen that the two zero dispersion wavelengths are found for each curve having a peculiar  $d/\Lambda$  ratio. It is also noticeable that, zero dispersion wavelengths are completely at different locations. For higher  $d/\Lambda$  the zero dispersion wavelengths shift broader both in left and right positions and provides a flat region where the slope variation is negligible. The zero dispersion wavelengths for  $d/\Lambda = 0.7$ , found at 960 nm

and 1750 nm for this structure and the pumping wavelength is chosen in the anomalous dispersion region in between two zero dispersion wavelengths and that is 1100 nm.

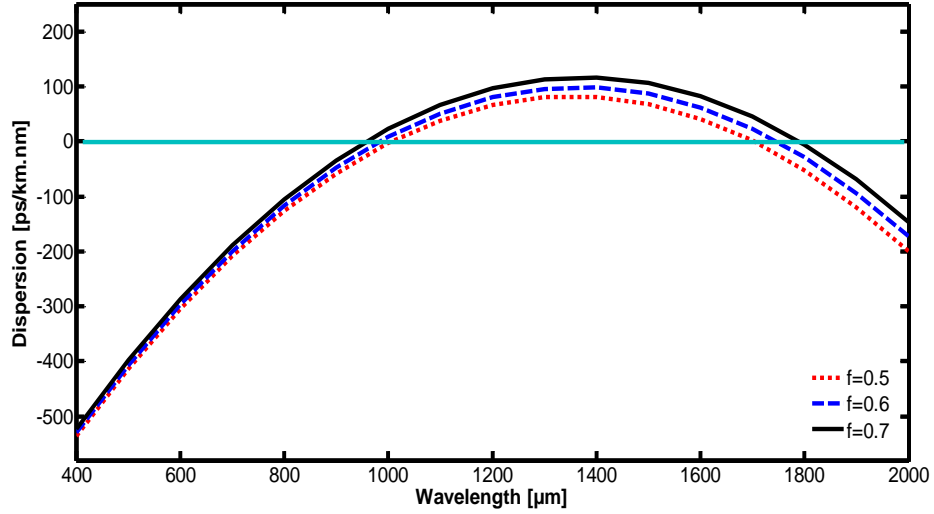


**Fig. 5.2** Dispersion as a function of wavelength for different filling factors,  $f$ .

As it can be observed, the zero dispersion wavelength is different from [107]. However, since even a slight change in the hole size and the lattice pitch lead to significant changes in the dispersion, we did not make any attempt to match the data from the [107] by adjusting the fiber structural dimensions.

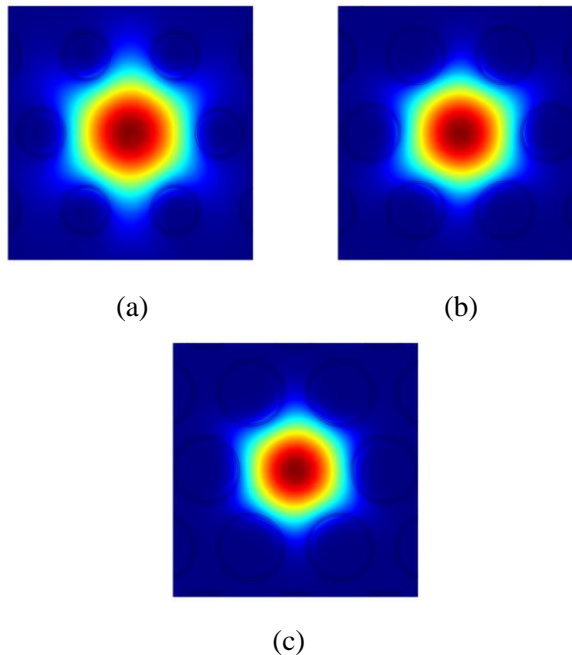


**Fig. 5.3** Electric field distributions at 1100 nm when filling factor (a) 0.5 (b) 0.6 (c) 0.7.

Figure 5.3 shows the dominant electric-field distribution of the fundamental mode at the pumping wavelength i.e. 1100 nm for different  $d/\Lambda$  ratios. The light is more strongly confined in the core region of the hybrid polymer PCF when the filling factor i.e.  $d/\Lambda = 0.7$ .

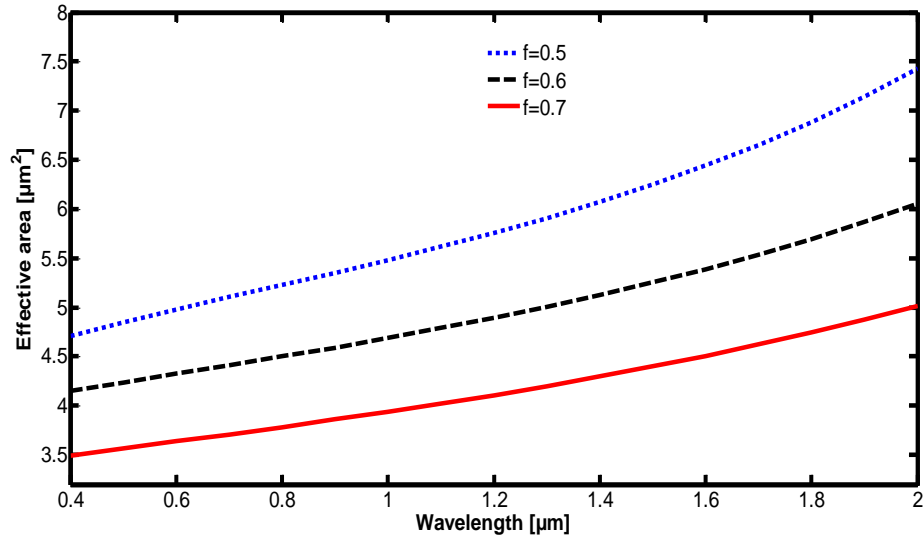


**Fig. 5.4** Effective area as a function of wavelength for different filling factors,  $f$ .

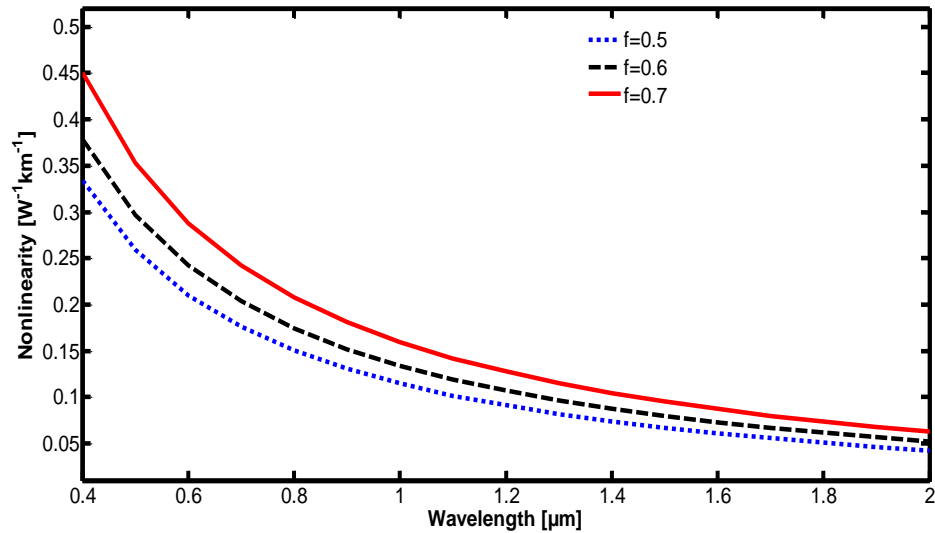


**Fig. 5.5** Nonlinearity parameter as a function of wavelength for different filling factors,  $f$ .

The effective area and the corresponding nonlinearity parameter are displayed in Figure 5.4 and 5.5. As it can be observed, with the increase in filling factor i.e.  $d/\Lambda$  the modal effective area decrease significantly and corresponding nonlinearity parameter increased, and maximum nonlinearity is achieved when the filling factor is 0.7.

By taking 1100 nm as the pumping wavelength, we calculate higher order dispersion parameters. Fig. 5.6 to Fig. 5.16 show the calculated GVD dispersion parameters starting from  $\beta_2$  to  $\beta_{12}$ . It is clear that the values that increase as the order of the dispersion parameter is higher [107].

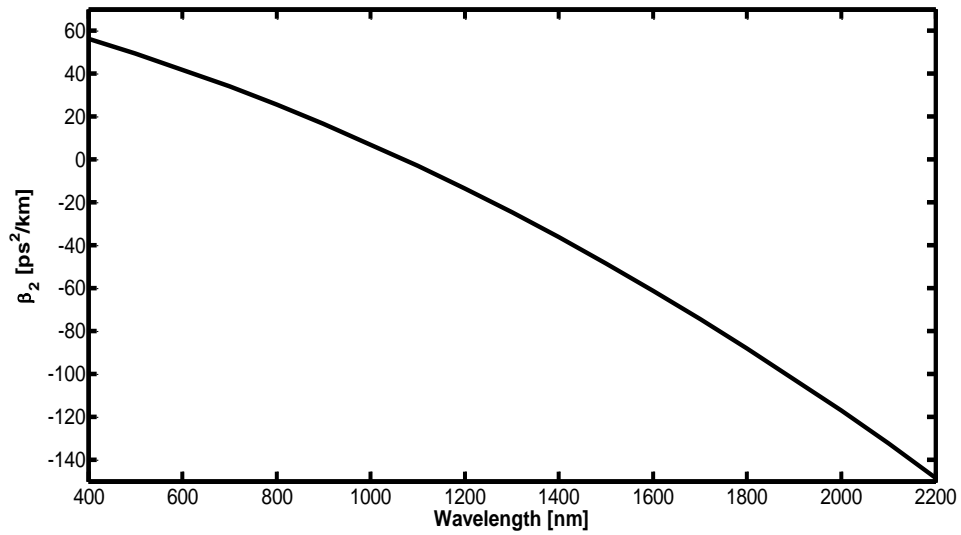


**Fig.5.6** 2<sup>nd</sup> order dispersion (GVD) parameter.

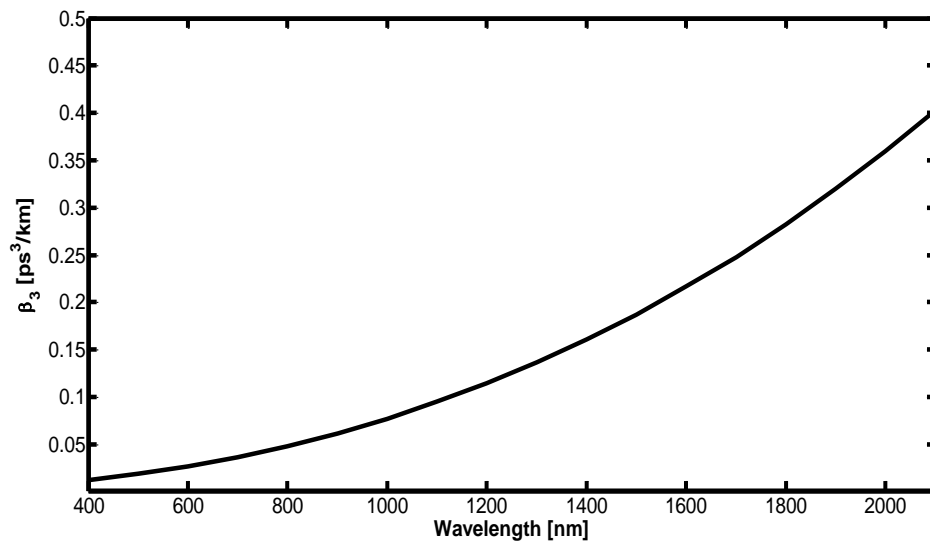


**Fig.5.7** 3<sup>rd</sup> order dispersion parameter.

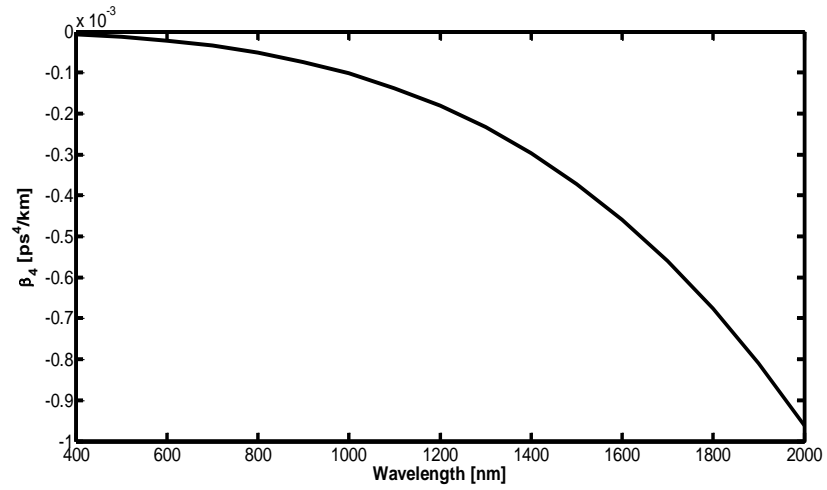


**Fig. 5.8** 4<sup>th</sup> order dispersion parameter.

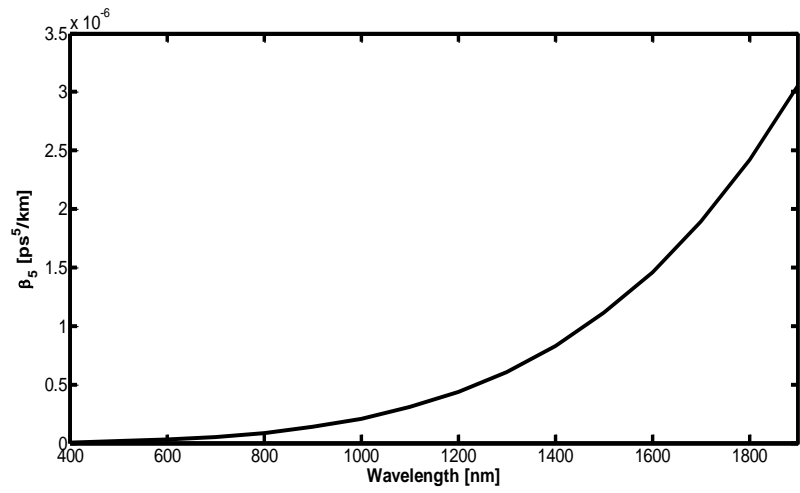


**Fig. 5.9** 5<sup>th</sup> order dispersion parameter.

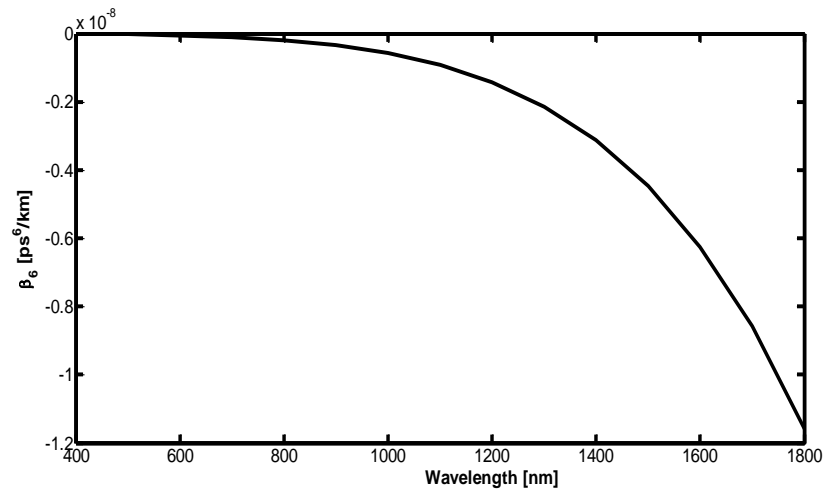


**Fig. 5.10** 6<sup>th</sup> order dispersion parameter.

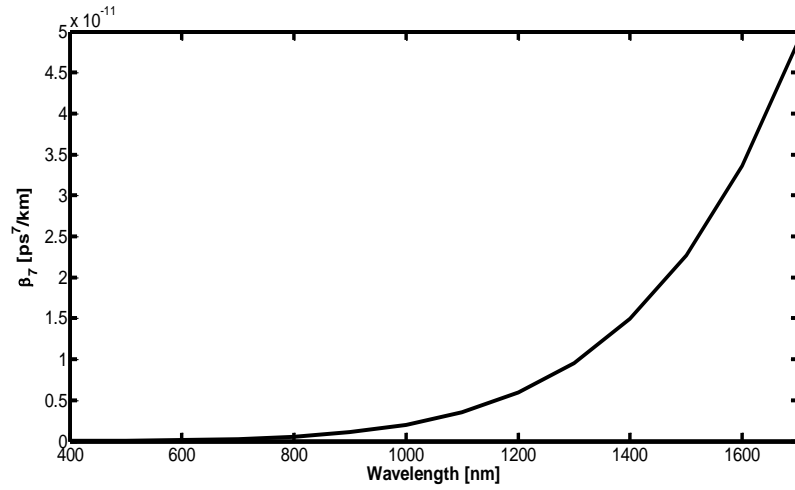


**Fig. 5.11** 7<sup>th</sup> order dispersion parameter.

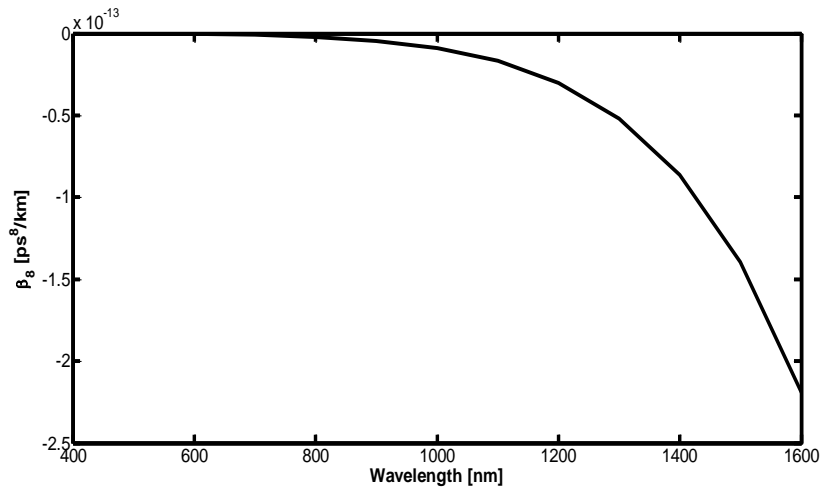


**Fig. 5.12** 8<sup>th</sup> order dispersion parameter.

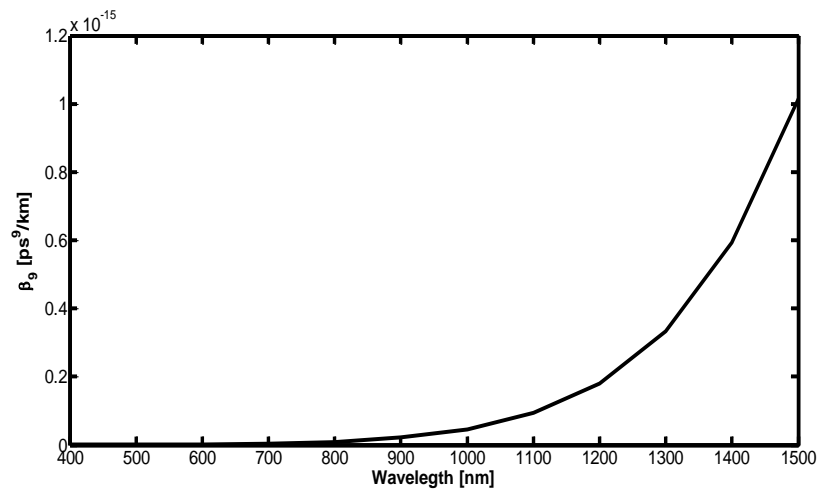


**Fig. 5.13** 9<sup>th</sup> order dispersion parameter.



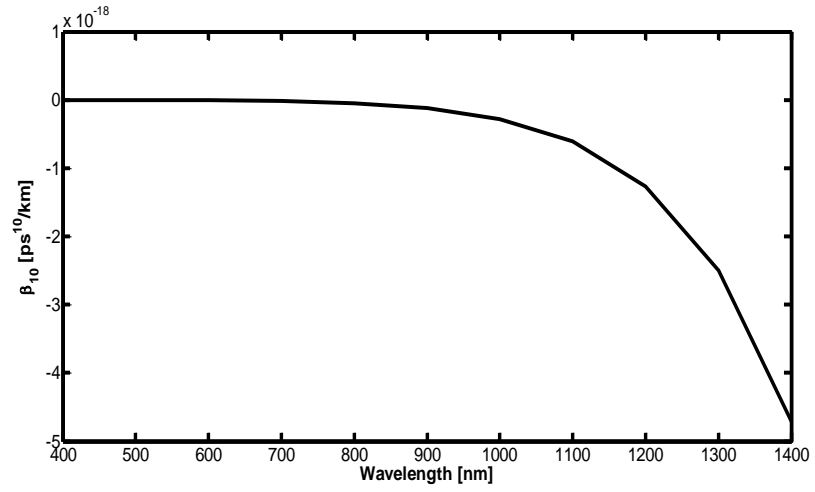


**Fig. 5.14** 10<sup>th</sup> order dispersion parameter.

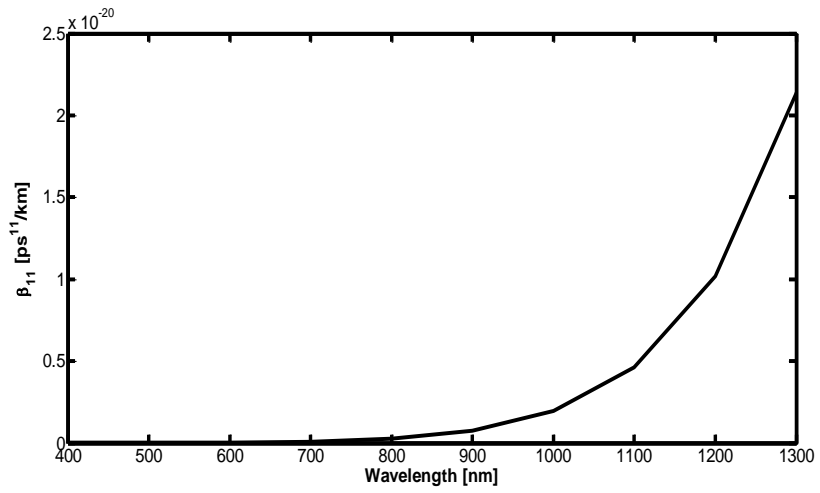


**Fig. 5.15** 11<sup>th</sup> order dispersion parameter.

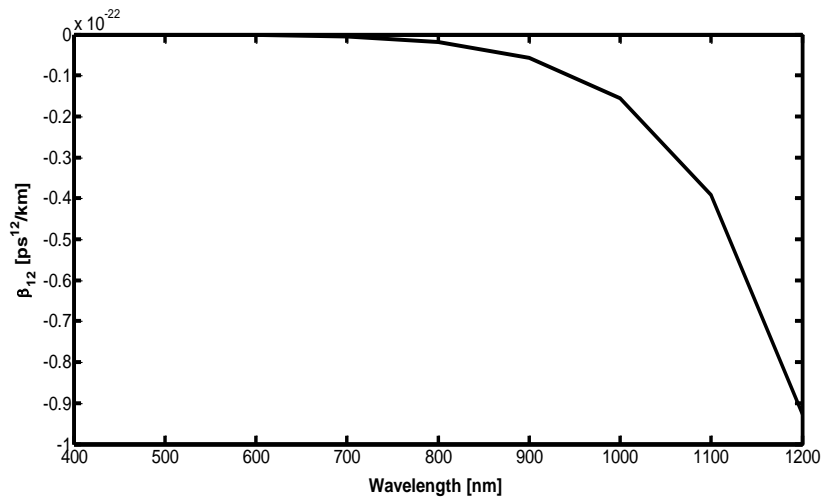


**Fig. 5.16** 12<sup>th</sup> order dispersion parameter.

The values used in simulation process are summarized in Table 5.1 and 5.2.

**Table 5.1**

Simulation parameters for proposed hybrid polymer PCF

| Parameters                                  | Value                               | Remarks  |
|---|-------------------------------------|--|
| Zero dispersion wavelengths                 | 960 nm & 1750 nm                    | Using eq. (4.13)   |
| Pumping Wavelength                          | 1100 nm                             | Is arbitrarily chosen in between zero dispersion wavelengths and at anomalous dispersion regime  |
| Effective area at 1100 nm, $A_{\text{eff}}$ | $4.002 \mu\text{m}^2$               | Using eq. (4.18)   |
| Nonlinearity parameter at 1100 nm, $\gamma$ | $0.142 \text{ W}^{-1}\text{m}^{-1}$ | Using eq. (4.17)   |
| Length of fiber                             | 5 cm, 10 cm, 30 cm                  | Chosen such that fiber length must be larger than dispersion length $L_D$ , and nonlinear length $L_{NL}$ , in order for the dispersive and nonlinear effects to broaden the inlet pulse [66]  |
| FWHM of the input pulse, $T_{FWHM}$         | 50 fs, 100 fs, 150 fs               | we have used hyperbolic secant pulse as input pulse. The envelope of the input pulse is $A(0, t) = N\sqrt{P_0} \text{sech}(t/T_0)$ , where $P_0$ is the peak power of the input pulse and $T_0$ is the pulse width related to the full width at the half maximum of the pulse through $T_{FWHM}/1.763$ . |
| Peak power of the input pulse               | 5 kW, 10 kW, 20 kW                  | we have used hyperbolic secant pulse as input pulse with peak power of 1 kW, 5 kW, 10 kW, and 20 kW respectively.  |

**Table 5.2**

Higher order dispersion coefficients for proposed hybrid polymer PCF at pumping wavelength,  $\lambda=1100$  nm

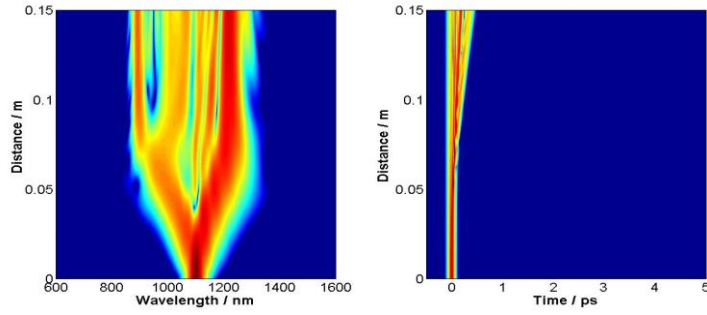
| Dispersion Coefficients | Value   | Remarks                     |
|-------------------------|---|-----------------------------|
| $\beta_2$               | $-3.09 \times 10^{-3} \text{ ps}^2/\text{m}$      | Calculated using eq. (4.14) |
| $\beta_3$               | $0.09469 \times 10^{-3} \text{ ps}^3/\text{m}$    |                             |
| $\beta_4$               | $-0.0001375 \times 10^{-3} \text{ ps}^4/\text{m}$ |                             |
| $\beta_5$               | $3.05 \times 10^{-10} \text{ ps}^5/\text{m}$      |                             |
| $\beta_6$               | $-9.2 \times 10^{-13} \text{ ps}^6/\text{m}$      |                             |
| $\beta_7$               | $3.538 \times 10^{-15} \text{ ps}^7/\text{m}$     |                             |
| $\beta_8$               | $-1.666 \times 10^{-17} \text{ ps}^8/\text{m}$    |                             |
| $\beta_9$               | $9.344 \times 10^{-20} \text{ ps}^9/\text{m}$     |                             |
| $\beta_{10}$            | $-6.115 \times 10^{-22} \text{ ps}^{10}/\text{m}$ |                             |
| $\beta_{11}$            | $4.597 \times 10^{-24} \text{ ps}^{11}/\text{m}$  |                             |
| $\beta_{12}$            | $-3.921 \times 10^{-26} \text{ ps}^{12}/\text{m}$ |                             |

In simulation we have used hyperbolic secant pulse as input pulse with peak power of 1 kW, 5 kW, 10 kW, and 20 kW respectively. The envelope of the input pulse is  $A(0, t) = N\sqrt{P_0} \text{sech}\left(\frac{t}{T_0}\right)$ , where  $P_0$  is the peak power of the input pulse and  $T_0$  is the pulse width related to the full width at the half maximum of the pulse through  $T_{FWHM}/1.763$ . The order of the solitons is determined by both fiber and pulse parameters [12].

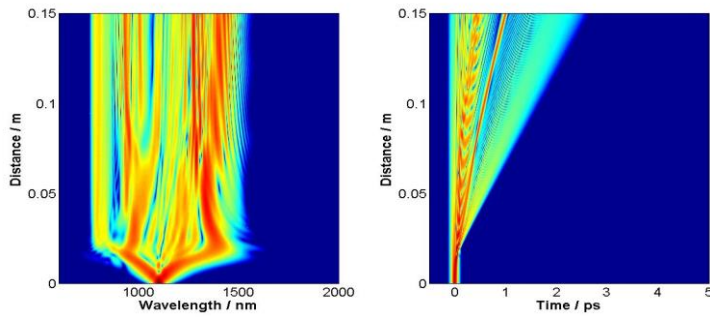
$$N^2 = \frac{\gamma P_0 T_0^2}{|\beta_2|}$$

If  $N > 1$ , the higher order soliton dynamics determine the pulse broadening [12].

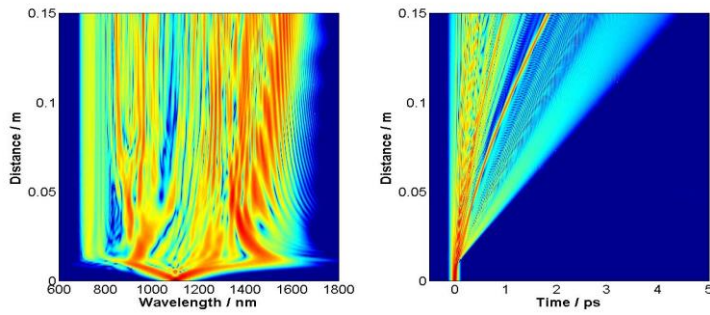
From Figure 5.17 (d), it is seen that by using peak power 20 kW and  $T_{FWHM} = 28.4$  fs observed spectral broadening is about 1666 nm from 499 nm to 2166 nm, and by using peak power of 10 kW, and 5 kW, obtained spectral broadening about 1252 nm (Fig. 5.17c), and 892.8 nm (Fig. 5.17b) respectively. In the above cases, only 15 cm long PCF is employed. From the results it is evident that with the increase of peak power supercontinuum becomes broader.



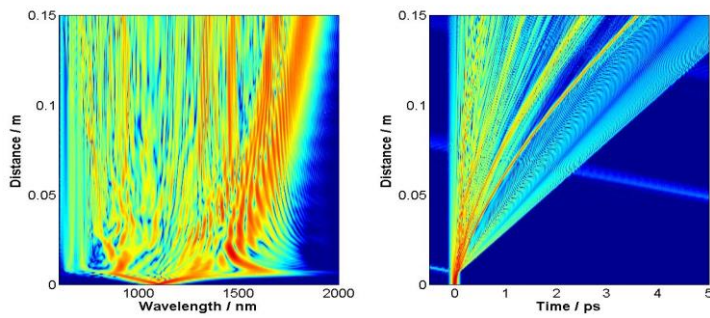
(a)



(b)



(c)



(d)

**Fig. 5.17** Spectral and temporal broadening in 15 cm long HP-PCF with  $T_{FWHM}$  as 28.4 fs, and peak power (a) 1 kW (b) 5 kW (c) 10 kW (d) 20 kW.

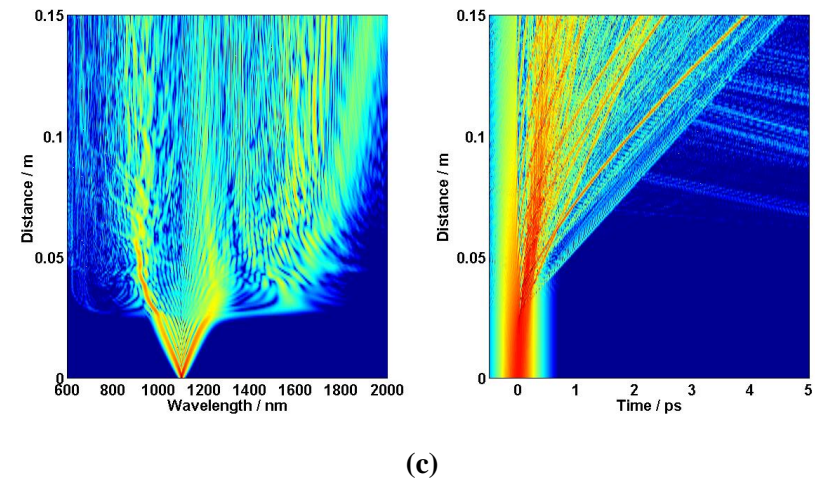
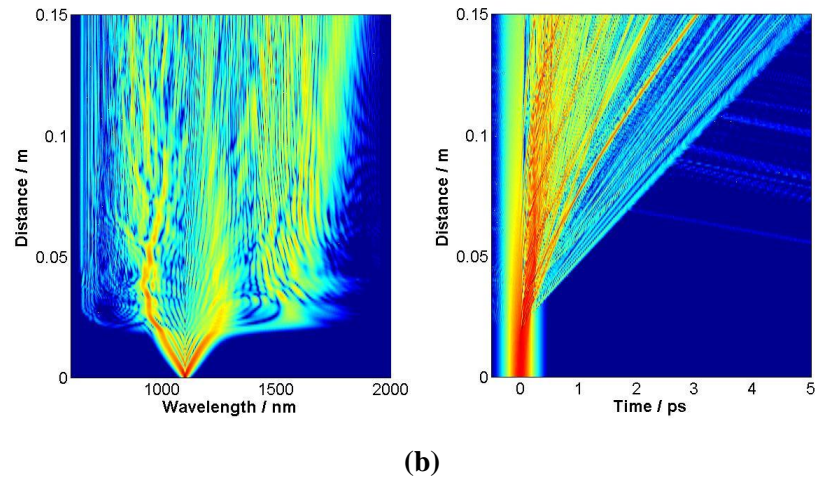
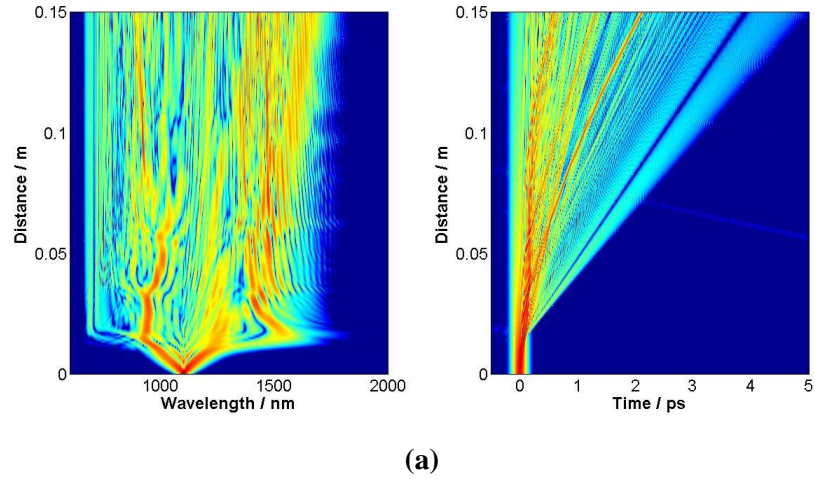
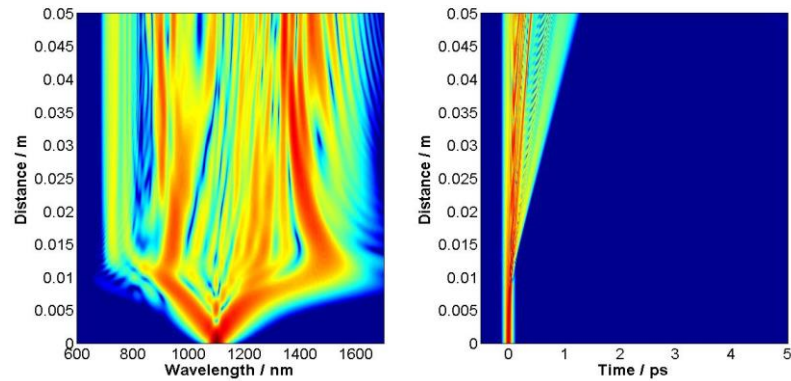


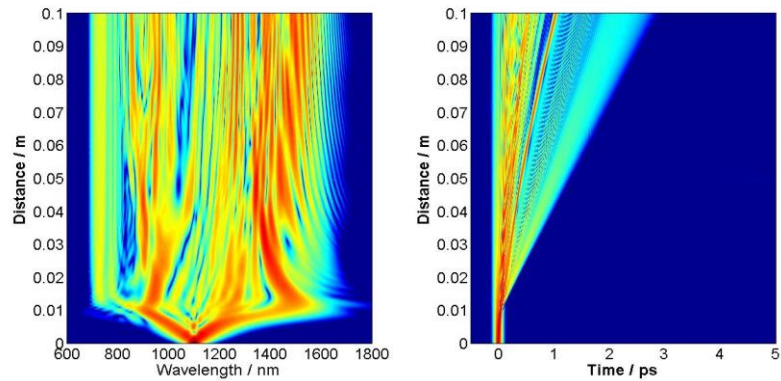
**Fig. 5.18** Spectral and temporal broadening in 15 cm long PCF using peak power as 10 kW and  
 (a)  $T_{FWHM} = 50$  fs (b)  $T_{FWHM} = 100$  fs (c)  $T_{FWHM} = 150$  fs

The effect of varying pulse duration,  $T_{FWHM}$  on broadening is also shown in Figure 5.18 by using peak power of 10 kW and fiber length of 15 cm. We have analyzed spectral broadening by using  $T_{FWHM}$  as 50 fs, 100 fs and 150 fs, respectively. From the results it is

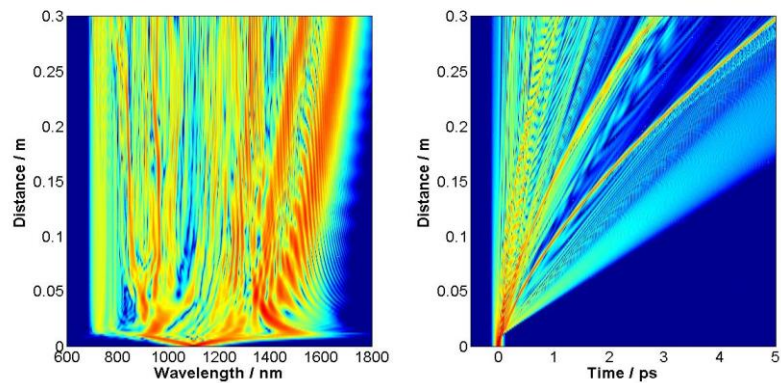
seen that as  $T_{FWHM}$  increases, supercontinua becomes broader. A wide SC spectrum occurs due to combined actions of self-phase modulation, Raman effect, and soliton fission. Broadband SC finds extensive applications in optical sensing, ultrafast pulse generation, spectroscopy, optical coherence tomography etc. [12, 38]. This is summarized in Table 5.3.



(a)



(b)



(c)

**Fig. 5.19** Spectral and temporal broadening using peak power as 10 kW,  $T_{FWHM}$  as 28.4 fs and (a) fiber length = 5 cm (b) fiber length = 10 cm (c) fiber length = 30 cm.

A given N order soliton can be broken up into N fundamental solitons due to different nonlinear processes like higher order dispersion, self-steepening, and stimulated Raman scattering [12]. Centre frequencies of the resulting fundamental solitons continuously shift toward the smaller frequencies i.e. longer wavelengths (red side) of the spectrum as a result of the self-frequency shift induced by Raman scattering process and nonsoliton radiations result in a broadening on the blue side of the spectrum [103]. As a consequence supercontinuum is generated when the nonlinear length ( $L_{NL}$ ) and the dispersion lengths ( $L_D$ ) satisfy the conditions  $L_{NL} < L_D$  and  $L_{NL} < L$  [12]. L is the length of PCF.

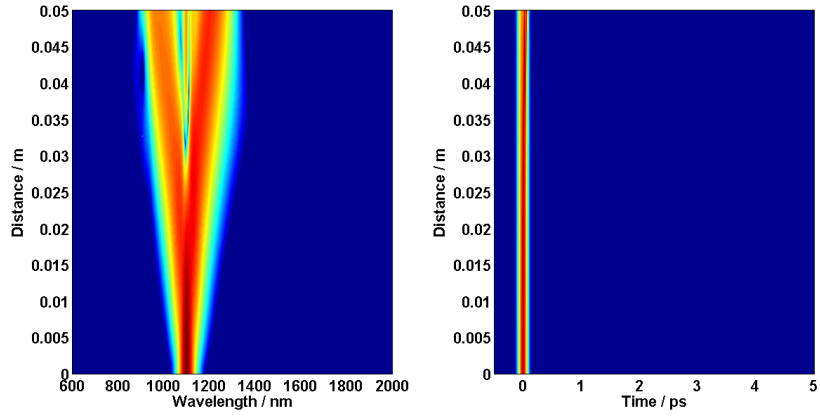
Generally speaking, the longer the fiber length, the broader the supercontinuum generated, so a suitable length is to be chosen. However, the fiber length  $z$  must be larger than dispersion length ( $L_D$ ) and nonlinearity length ( $L_{NL}$ ) in order for the dispersive and nonlinear effects to broaden the inlet pulse [12]. Under such conditions, initially, self-phase modulation leads to a symmetric spectral broadening of the optical pulse, after which the requirement for phase matching conditions is fulfilled, and then soliton fission occurs, and finally, the self-frequency shift and nonsoliton radiations processes broaden the spectral components on both sides of the spectrum, as a consequence of which a supercontinuum is generated. Figure 5.19 (a), (b) and (c) satisfies the above statement but an intensity variation is noticed as the fiber length is increasing.

The effects of higher order dispersion coefficients on pulse broadening are also studied. For a certain input power addition of higher order dispersion coefficients makes the supercontinuum broader but further increase in input power makes the supercontinuum much broader when only 2<sup>nd</sup> and 3<sup>rd</sup> order coefficients are added. Hence, it can be concluded that for a wider supercontinuum only the 2<sup>nd</sup> and 3<sup>rd</sup> order dispersion coefficients are significant. The whole scenario is summarized in Table 5.4.

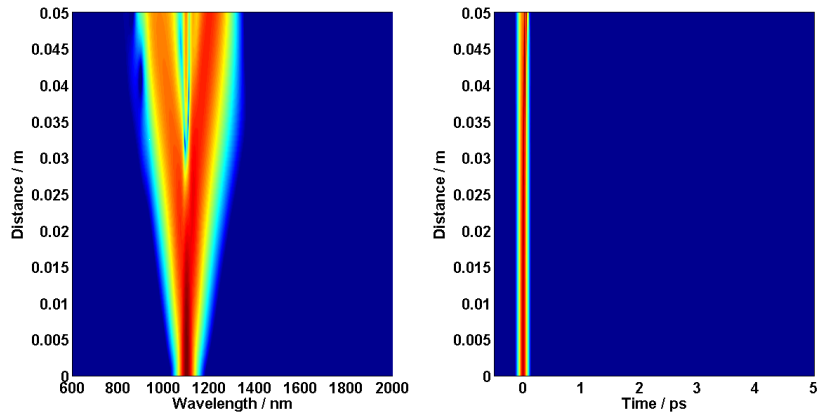
**Table 5.3**  
**Summary of Simulation Results**

| Parameters fixed for simulation               | Varying parameters   | Spectral Broadening |         | Total Broadening | Remarks   |
|---|----------------------|---------------------|---------|------------------|---|
|   |                      | from                | to      |                  |   |
| Fiber length 15 cm and pulse duration 28.4 fs | Input power 1 KW     | 863 nm              | 1370 nm | 506 nm           | with the increase of input power supercontinuum becomes broader       |
|   | 5 KW                 | 727 nm              | 1620 nm | 892 nm           |   |
|   | 10 KW                | 545 nm              | 1797 nm | 1252 nm          |   |
|   | 20 KW                | 499 nm              | 2166 nm | 1666 nm          |   |
| Fiber length 15 cm and input power 10 KW      | Pulse duration 50 fs | 510 nm              | 1800 nm | 1289 nm          | supercontinuum becomes broader as the pulse duration increases        |
|   | 100 fs               | 505 nm              | 2025 nm | 1519 nm          |   |
|   | 150 fs               | 499 nm              | 2128 nm | 1628 nm          |   |
| input power 10 KW and pulse duration 28.4 fs  | Fiber length 5 cm    | 666 nm              | 1711 nm | 1044 nm          | the longer the fiber length, the broader the supercontinuum generated |
|   | 10 cm                | 602 nm              | 1751 nm | 1149 nm          |   |
|   | 30 cm                | 500 nm              | 1882 nm | 1381 nm          |   |

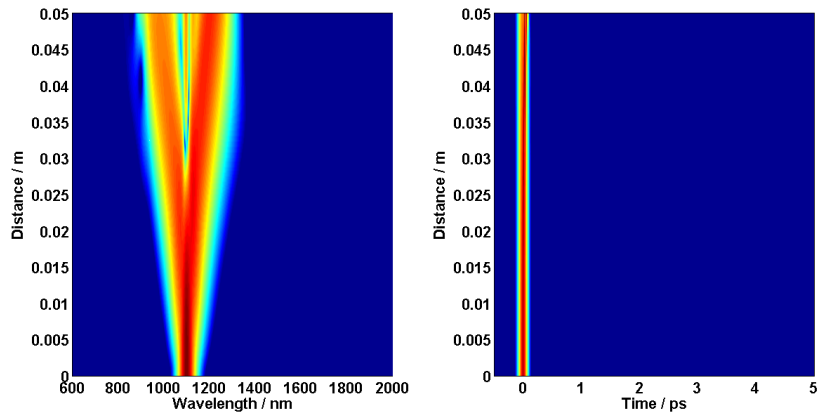




(a)



(b)



(c)

**Fig. 5.20** Spectral and temporal broadening using peak power as 1 kW,  $T_{FWHM}$  as 28.4 fs, fiber length 5 cm and dispersion coefficients including (a) 2<sup>nd</sup> and 3<sup>rd</sup> order (b) 2<sup>nd</sup> order to 6<sup>th</sup> order (c) 2<sup>nd</sup> order to 12<sup>th</sup> order.

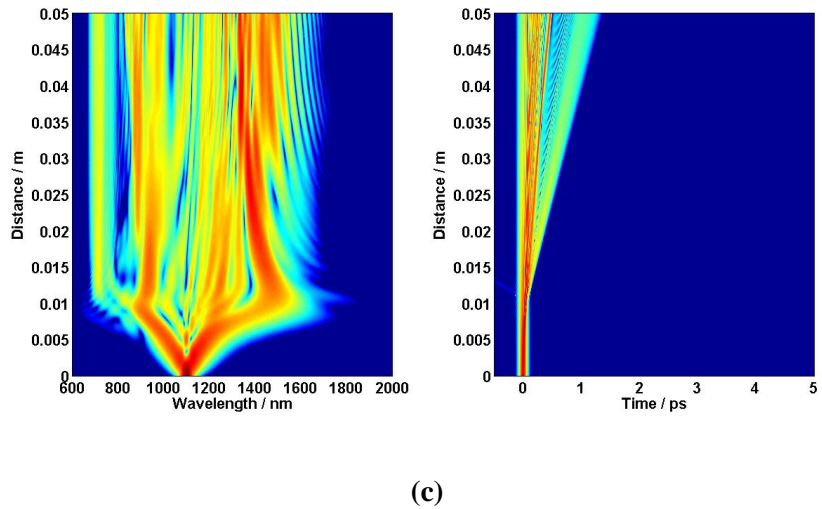
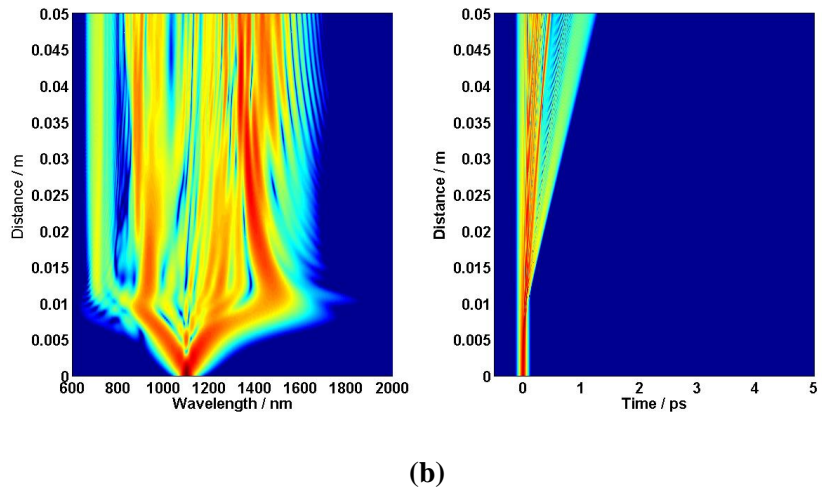
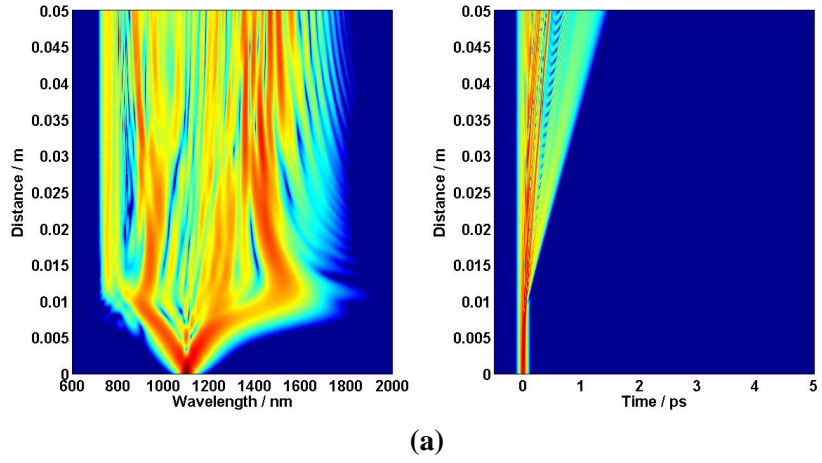


**Fig. 5.21** Spectral and temporal broadening using peak power as 10 kW,  $T_{FWHM}$  as 28.4 fs, fiber length 5 cm and dispersion coefficients including (a) 2<sup>nd</sup> and 3<sup>rd</sup> order (b) 2<sup>nd</sup> order to 6<sup>th</sup> order (c) 2<sup>nd</sup> order to 12<sup>th</sup> order.

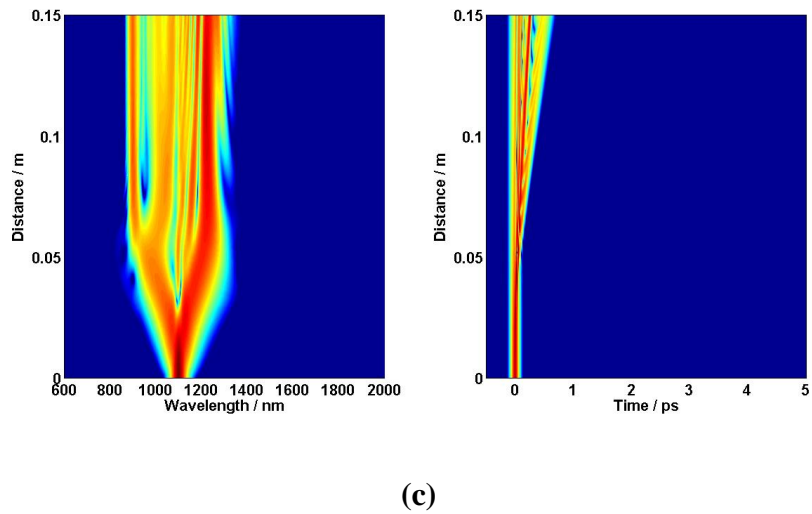
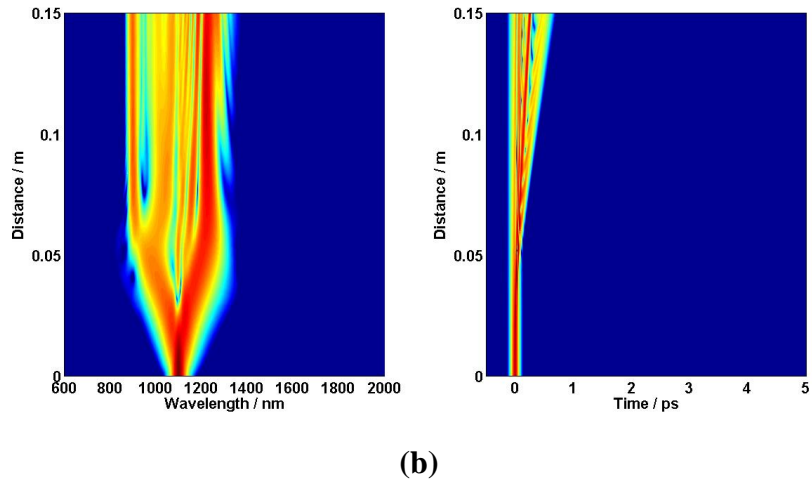
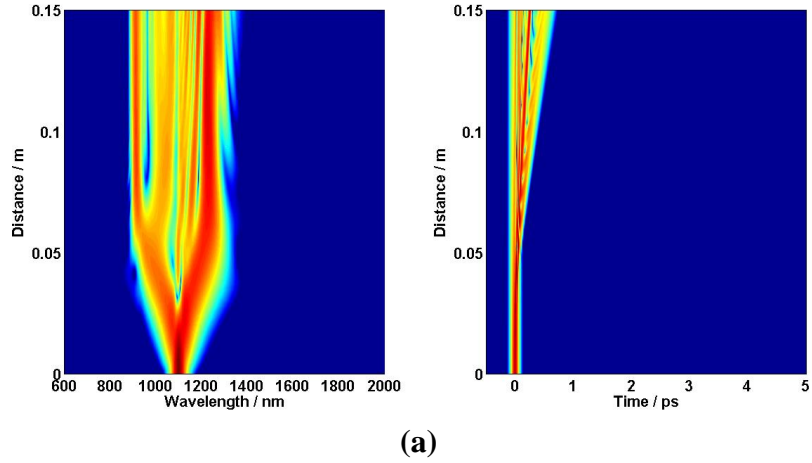


**Fig. 5.22** Spectral and temporal broadening using peak power as 1 kW,  $T_{FWHM}$  as 28.4 fs, fiber length 15 cm and dispersion coefficients including (a) 2<sup>nd</sup> and 3<sup>rd</sup> order (b) 2<sup>nd</sup> order to 6<sup>th</sup> order (c) 2<sup>nd</sup> order to 12<sup>th</sup> order.

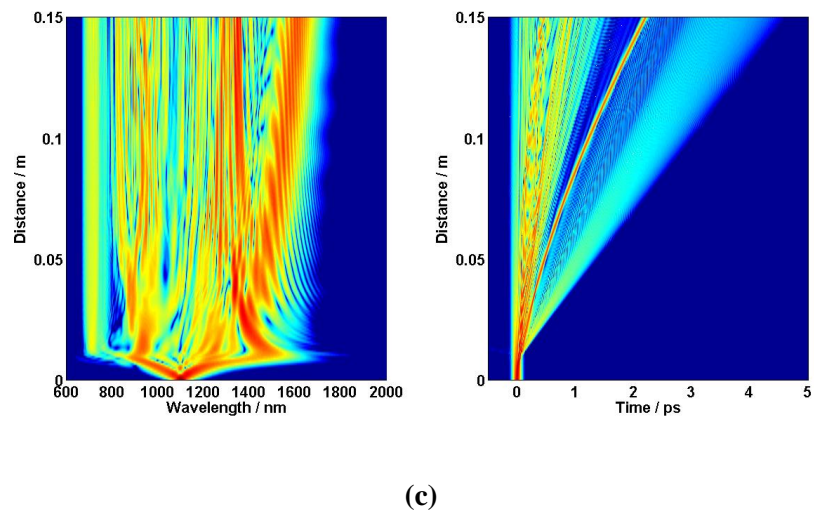
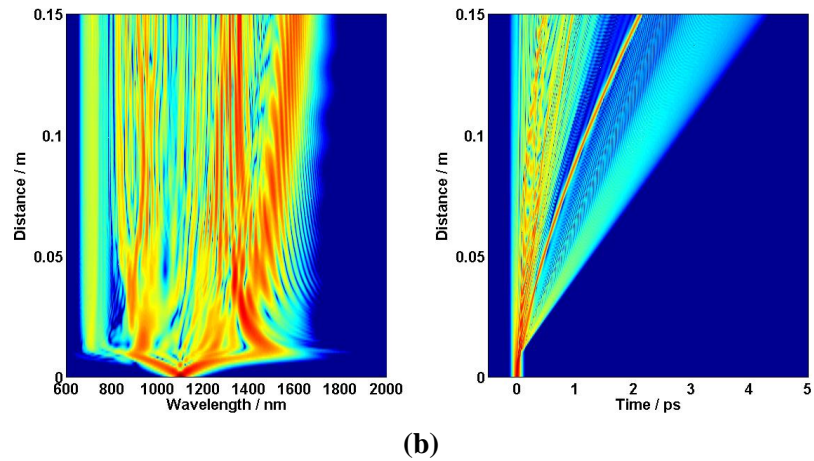
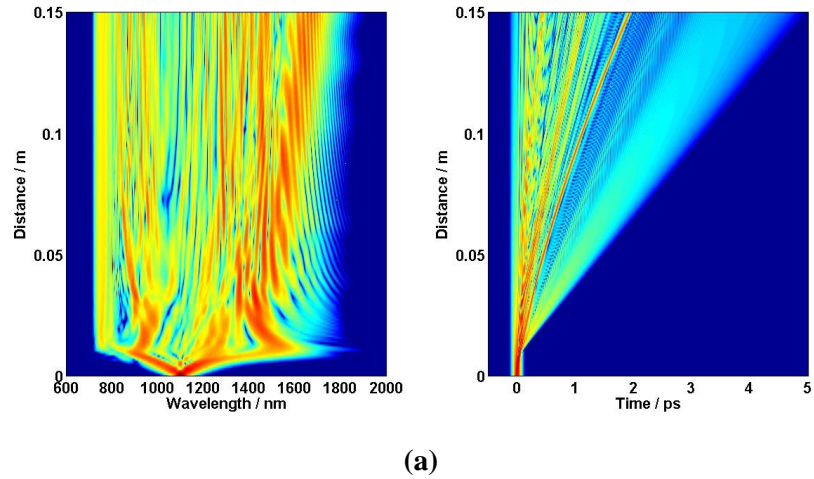


**Fig. 5.23** Spectral and temporal broadening using peak power as 10 kW,  $T_{FWHM}$  as 28.4 fs, fiber length 15 cm and dispersion coefficients including (a) 2<sup>nd</sup> and 3<sup>rd</sup> order (b) 2<sup>nd</sup> order to 6<sup>th</sup> order (c) 2<sup>nd</sup> order to 12<sup>th</sup> order.

**Table 5.4**

**Summary of effects of higher order dispersion coefficients on pulse broadening**

| Parameters fixed for simulation              | Varying parameters   | Spectral broadening when input power 1 KW | Spectral broadening when input power 10 KW | Spectral broadening when input power 20 KW | Remarks  |
|--|--|---|--|--|--|
| Fiber length 5 cm and pulse duration 28.4 fs | When 2 <sup>nd</sup> and 3 <sup>rd</sup> order dispersion coefficients added | 466 nm<br>(from 884 nm to 1351 nm)        | 1092 nm<br>(from 726 nm to 1819 nm)        | 1507 nm<br>(from 670 nm to 2178 nm)        | For a certain input power addition of higher order dispersion coefficients makes the supercontinuum broader but further increase in input power makes the supercontinuum much broader when only 2 <sup>nd</sup> and 3 <sup>rd</sup> order coefficients are added. Hence, it can be concluded that for a wider supercontinuum only the 2 <sup>nd</sup> and 3 <sup>rd</sup> order dispersion coefficients are significant. |
|  | When 2 <sup>nd</sup> to 6 <sup>th</sup> order dispersion coefficients added  | 467 nm<br>(from 879 nm to 1347 nm)        | 1030 nm<br>(from 670 nm to 1700 nm)        | 1382 nm<br>(from 507 nm to 1890 nm)        |  |
|  | When 2 <sup>nd</sup> to 12 <sup>th</sup> order dispersion coefficients added | 471 nm<br>(from 876 nm to 1348 nm)        | 1050 nm<br>(from 670 nm to 1720 nm)        | 1438 nm<br>(from 506 nm to 1995 nm)        |  |

# CHAPTER 6

## CONCLUSIONS

### 6.1 Conclusions of the Work

We have designed and analyzed a novel hybrid polymer PCF which allows us to generate wideband supercontinuum spectra of more than 1600 nm with a pump wavelength of 1100 nm in anomalous dispersion region. We proposed here a non-linear hybrid polymer PCF with integrated silica glass layers of few nanometers at the outer surface of the air holes and optimizes both the parameters of pump source (pump wavelengths, pulse duration, and the pump power level) and fiber properties (the material of fiber, geometry parameters) at chosen pump wavelength by varying the pitch and diameter of air-holes. Using pump pulses at a wavelength of 1100 nm with a peak power and pulse duration of 20 kW and 28.4 fs, respectively, we obtained a supercontinuum spectra covering a wavelength range from 500 nm to beyond 2166 nm. Such an ultra-broadband supercontinuum spectra is expected to have profound applications in high performance optical coherence tomography (OCT) imaging systems where a coherent and broadband light source with sufficient brightness and penetration depth is required.

The evolution of supercontinuum generation was investigated with the variations of fiber length, peak powers, and pulse duration. It has been found that with the increase of peak power supercontinuum becomes broader. An increased spectral broadening can be achieved when an increment in pulse duration is made. The longer the fiber length, the broader the supercontinuum generated but there is a variation in intensity level as the fiber length is increased.

The effects of higher order dispersion coefficients on pulse broadening are also studied. For a certain input power addition of higher order dispersion coefficients makes the supercontinuum broader but further increase in input power makes the supercontinuum much broader when only 2<sup>nd</sup> and 3<sup>rd</sup> order coefficients are added. Adding of 4<sup>th</sup> to upper order coefficients have no effect on supercontinuum at all. Hence, it can be concluded that for a wider supercontinuum only the 2<sup>nd</sup> and 3<sup>rd</sup> order dispersion coefficients are significant.

## **6.2 Future Scope of work**

The next step in this line of research would be mainly experimental. The results from the simulations need to be verified. The numerical model can be improved. A better Raman response function could be employed. Higher order Symmetrized Split Step Fourier Method could be introduced for more accurate results. We have analyzed SC generation by using anomalous dispersion regime. In future it will be of great interest to analysis of SC generation by selecting pumping region at normal dispersion regime. It is also interesting to use other geometry like spiral PCF, square PCF etc. and in the further investigation as a host material different polymers can be used. With the advancements in the fabrication techniques we are quite optimistic that the proposed PCF can be fabricated. After fabricating such structure, the numerical results may be verified experimentally that can strengthen the findings.

## References

- [1] Knight, J. C., “Photonic crystal fibers,” *Nature*, vol. 424, pp. 847–851, 2003.
- [2] Russell, P. St. J., “Photonic crystal fibers,” *Science*, vol. 299, pp. 358–362, Jan. 2003.
- [3] Keiser, G., *Optical Fiber Communications*, Tata McGraw Hill Publications, Second Edition, 1991.
- [4] Mortensen, N. A., Folkenberg, J. R., Nielsen, M. D., and Hansen, K. P., “Modal cutoff and the V parameter in photonic crystal fibers,” *Optics Letters*, vol. 28, pp. 1879–1881, 2003.
- [5] Reeves, W. H., Knight, J. C., Russell, P. St. J., and Roberts, P. J., “Demonstration of ultra-flattened dispersion in photonic crystal fibers,” *Optics Express*, vol. 10, pp. 609–613, 2002.
- [6] Humbert, G., Knight, J. C., Bouwmans, G., Russell, P. St. J., Williams, D. P., Roberts, P. J., and Mangan, B. J., “Hollow core photonic crystal fibers for beam delivery,” *Optics Express*, vol. 12, pp. 1477–1484, Apr. 2004.
- [7] Agrawal, A., Kejalakshmy, N., Chen, J., Rahman, B. M. A., and Grattan, K. T. V., “Soft glass equiangular spiral photonic crystal fiber for supercontinuum generation,” *IEEE Photonics Technology Letters*, vol. 21, no. 22, pp. 1722-1724, Nov. 2009.
- [8] Agrawal, A., Azabi, Y. O., and Rahman, B. M. A., “Stacking the equiangular spiral,” *IEEE Photonics Technology Letters*, vol. 25, no. 3, pp. 291-294, Feb. 2013.
- [9] J. C. Knight, T. A. Birks, P. St. J. Russell, D. M. Atkin, “All-silica single-mode optical fiber with photonic crystal cladding,” *Opt. Lett.*, vol. 19, no. 19, pp. 1547-1549, 1996.
- [10] Tyagi, H. K., Schmidt, M. A., Sempere, L. P., and Russell, P. S., “Optical properties of photonic crystal fiber with integral micron-sized Ge wire,” *Optics Express*, vol. 16, no. 22, pp. 17227-17236, 2008.
- [11] Karim, M. R., Rahman, B. M. A., and Agrawal, G. P., “Dispersion engineered  $\text{Ge}_{11.5}\text{As}_{24}\text{Se}_{64.5}$  nanowire for supercontinuum generation: A parametric study,” *Optics Express*, vol. 22, no. 36, pp. 31029-31040, 2014.
- [12] Agrawal, G. P., *Non-Linear Fiber Optics*, 5<sup>th</sup> edition, Academic, 2013.
- [13] Alfano, R. R., and Shapiro, S. L., “Emission in the region of 4000 to 7000 via four photon coupling in glass,” *Phys. Rev. Lett.*, vol. 24, pp. 584-587, 1970.
- [14] Alfano, R. R., and Shapiro, S. L., “Observation of self-phase modulation and small scale filaments in crystals and glasses,” *Phys. Rev. Lett.*, vol. 24, pp. 592-594, 1970.
- [15] Humbert, G., Wadsworth, W. J., Leon-Saval, S. G., Knight, J. C., Birks, T. A., and Russell, P. St. J., “Supercontinuum generation system for optical coherence tomography based on tapered photonic crystal fibre,” *Optics Express*, Vol. 14, No. 4, pp. 1596-1603, 2006.



- [16] Saghaei, H., Heidari, M. E., and Moravvej-Farshi, M. K., “Midinfrared supercontinuum generation via  $\text{As}_2\text{Se}_3$  chalcogenide photonic crystal fibers,” *Applied Optics*, Vol. 54, pp. 2072-2079, 2015.
- [17] Liu, B. W., Hu, M. -L., Fang, X. H., Wu, Y. -Z., Song, Y. -J., Chai, L., Wang, C. -Y., and Zheltikov, A., “High-power wavelength-tunable photonic-crystal-fiber-based oscillator-amplifier-frequency shifter femtosecond laser system and its applications for material microprocessing,” *Laser Physics Letter*, Vol. 6, No. 1, pp. 44-48, 2009.
- [18] Sharping, J. E., Mark, A., Foster, and Alexander, L. G., “Octave-spanning, high-power microstructure-fiber-based optical parametric oscillators,” *Optics Express*, Vol. 15, No. 4, pp. 1474–1479, 2007.
- [19] Sinobad, M., Monat, C., Luther-Davies, L., Ma, P., Madden, S., Moss, D. J., Mitchell, A., Allieux, D., Orobtcouk, R., Boutami, S., Hartmann, J.-M., Fedeli, J.-M., and Grillet, C., “Mid-infrared octave spanning supercontinuum generation to 8.5  $\mu\text{m}$  in silicon-germanium waveguides,” *Optica*, Vol. 5, No. 4, pp. 360-366, 2018.
- [20] Ranka, J. K., Windeler, R.S., and Stentz, A. J., “Visible continuum generation in air-silica microstructure optical fibers with anomalous dispersion at 800nm,” *Optics Letters*, vol. 25, pp. 25-27, 2000.
- [21] Dudley, J. M., Provino, L., Grossard, N., Maillotte, H., Windeler, R. S., Eggleton, B. J., and Coen, S., “Supercontinuum generation in air–silica microstructured fibers with nanosecond and femtosecond pulse pumping,” *J. Opt. Soc. Am. B*, vol. 19, pp. 765-771, 2002.
- [22] Jain, D., Sidharthan, R., Moselund, P. M., Yoo, S., Ho, D., and Bang, O., “Record Power, ultra-broadband supercontinuum source based on  $\text{GeO}_2$  doped silica fiber,” *Optics Express*, vol. 24, pp. 26667-26677, 2016.
- [23] Town, G. E., Funaba, T., Ryan, T., and Lyytikainen, K., “Optical supercontinuum generation from nanosecond pump pulses in an irregularly microstructured air-silica optical fiber,” *Appl. Phys. B*, vol. 77, pp. 235-238, 2003.
- [24] Ghosh, D., Roy, S., Pal, M., Bhadra, S. K., Bookey, M. H., and Kar, A., “Generation of supercontinuum and its theoretical study in three ring silica microstructured optical fibers ,” *Appl. Opt.*, vol. 48, pp. G12-G20, 2009.
- [25] Hansen, K. P., “Dispersion flattened hybrid-core nonlinear photonic crystal fiber,” *Opt. Express*, vol. 11, pp. 1503–1509, 2003.
- [26] Heidepriem, E. H., Petropoulos, P., Asimakis, S., Finazzi, V., Moore, R. C., Frampton, K., Kpizumi, F., Richardson, D. J., and Monro, T. M., “Bismuth glass holey fibers with high nonlinearity,” *Optics Express*, vol. 12, no. 21, pp. 5082-5087, 2004.
- [27] Petropoulos, P., Heidepriem, E. H., Finazzi, V., Moore, R. C., Frampton, K., Richardson, D. J., and Monro, T. M., “Highly nonlinear and anomalously dispersive lead silicate glass holey fibers,” *Optics Express*, vol. 11, no. 16, pp. 3568-3573, 2003.

- [28] Qin, G., Yan, X., Kito, C., Liao, M., Chaudhari, C., Suzuki, T., and Ohishi, Y., "Ultrabroadband supercontinuum generation from ultraviolet to 6.28 micrometer in a fluoride fiber," *Appl. Phys. Lett.*, vol. 95, no. 16, 2009.
- [29] Domachuk, P., Wolchover, N. A., Cronin-Golomb, M., Wang, A., George, A. K., Cordeiro, C. M. B., Knight, J. C., and Omenetto, F. G., "Over 4000 nm bandwidth of Mid-IR supercontinuum generation in subcentimeter segments of highly nonlinear tellurite PCFs," *Optics Express*, vol. 16, no. 10, pp. 7161-7168, 2008.
- [30] Chaitanya, A. G. N., Saini, T. S., Kumar, A., and Sinha, R. K., "Ultra broadband mid-IR supercontinuum generation in  $\text{Ge}_{11.5}\text{As}_{24}\text{Se}_{64.5}$  based chalcogenide graded-index photonic crystal fiber: design and analysis," *Opt. Soc. Am.*, vol. 55, no. 36, pp. 10138-10145, 2016.
- [31] Chen, L., Gao, W., Chen, L., Wang, P., Ni, C., Chen, X., Zhou, Y., Zhang, W., Hu, J., Liao, M., Suzuki, T., and Ohishi, Y., "Numerical study on supercontinuum generation by different optical modes in  $\text{AsSe}_2\text{-As}_2\text{S}_5$  chalcogenide microstructured fiber," *Opt. Soc. Am.*, vo. 57, no. 3, pp. 382-390, 2018.
- [32] Karim, M. R., and Rahman, B. M. A., "Numerical investigation of mid-infrared supercontinuum generation in GeAsSe based chalcogenide photonic crystal fiber using low peak power," *Applied Physics Research*, vol. 8, no. 4, pp. 29-37, 2016.
- [33] Karim, M. R., Rahman, B. M. A., and Agrawal, G. P., "Mid-infrared supercontinuum generation using dispersion-engineered  $\text{Ge}_{11.5}\text{As}_{24}\text{Se}_{64.5}$  chalcogenide channel waveguide," *Optics Express*, vol. 23, no. 5, pp. 6903-6913, 2015.
- [34] Sharma, M., Konar, S., and Khan, K. R., "Supercontinuum generation in highly nonlinear hexagonal photonic crystal fiber at very low power," *Journal of Nanophotonics*, vol. 9, 2015.
- [35] Saini, T. S., Kumar, A., and Sinha, R. K., "Broadband Mid-infrared supercontinuum spectra spanning 2-15 micrometer using  $\text{As}_2\text{Se}_3$  chalcogenide glass triangular core graded index photonic crystal fiber," *Journal of Lightwave Technology*, vol. 33, no. 18, pp. 3914-3920, 2015.
- [36] Valliammai, M., and Sivabalan, S., "Wide-band supercontinuum generation in mid-IR using polarization maintaining chalcogenide photonic quasi-crystal fiber," *Applied Optics*, vol. 56, no. 16, pp. 4797-4806, 2017.
- [37] Chen, L., Gao, W., Chen, L., Wang, P., Ni, C., Chen, X., Zhou, Y., Zhang, W., Hu, J., Liao, M., Suzuki, T., and Ohishi, Y., "Numerical study on supercontinuum generation by different optical modes in  $\text{AsSe}_2\text{-As}_2\text{S}_5$  chalcogenide microstructured fiber," *Applied Optics*, Vol. 57, pp. 382-390, 2018.
- [38] Dudley, J. M., and Coen, S., "Numerical simulations and coherence properties of supercontinuum generation in photonic crystal and tapered optical fibers," *IEEE J. Sel. Top. Quantum Electron.*, Vol. 8, pp. 651-659, 2002.
- [39] Tiwari, M., and Janyani, V., "Two-Octave Spanning Supercontinuum in a Soft Glass Photonic Crystal Fiber Suitable for 1.55  $\mu\text{m}$  Pumping," *Journal of Lightwave Technology*, Vol. 29, No. 23, pp. 3560-3565, 2011.

- [40] Labat, D., Melin, G., Mussot, A., Fleureau, A., Galkovsky, L., Lempereur, S., and Kudlinski, A., "Phosphorus-Doped Photonic Crystal Fibers for High-Power (36 W) Visible CW Supercontinuum," *IEEE Photonics Journal*, Vol. 3, pp. 815-820, 2011.
- [41] Cherif, R., and Zghal, M., "Ultrabroadband, Midinfrared Supercontinuum Generation in Dispersion Engineered As<sub>2</sub>Se<sub>3</sub>-based Chalcogenide Photonic Crystal Fibers," *International Journal of Optics*, Vol. 2013, 876474, 2013.
- [42] Fang, X., and Kobayashi, T., "Evolution of a super-broadened spectrum in a filament generated by an ultrashort intense laser pulse in fused silica," *Appl. Phys. B*, vol. 77, pp. 167–170, 2003.
- [43] Silva, F., Austin, D., Thai, A., Baudisch, M., Hemmer, D., Faccio, A., Couairon, F., and Biegert, J., "Multi-octave supercontinuum generation from mid-infrared filamentation in a bulk crystal," *Nat. Commun.*, vol. 3, 2012.
- [44] Tortora, A., Corsi, C., and Bellini, M., "Comb-like supercontinuum generation in bulk media," *Appl. Phys. Lett.*, vol. 85, pp. 1113–1115, 2004.
- [45] Kandidov, V. P., Kosareva, O. G., Golubtsov, I. S., Liu, W., Becker, A., Aközbek, N., Bowden, C. M., and Chin, S. L., "Self transformation of a powerful femtosecond laser pulse into a white-light laser pulse in bulk optical media (or supercontinuum generation)," *Appl. Phys. B*, vol. 77, pp. 149–165, 2003.
- [46] Nishioka, H., and Ueda, K., "Super-broadband continuum generation with transient self-focusing of a terawatt laser pulse in rare gases," *Appl. Phys. B*, vol. 77, pp. 171–175, 2003.
- [47] Nagatsuma, T., Nishii, H., and Ikeo, T., "Terahertz imaging based on optical coherence tomography (Invited)," *Photonic Research*, Vol. 2, pp. B64-B69, 2014.
- [48] Han, H., Park, H., Cho, M., and Kim, J., "Terahertz pulse propagation in a plastic photonic crystal fiber," *Applied Physics Letter*, Vol. 80, pp. 2634-2636, 2002.
- [49] Aming, A., Uthman, M., Chitaree, R., Mohammed, W., and Rahman, B. M. A., "Design and Characterization of Porous Core Polarization Maintaining Photonic Crystal Fiber for THz Guidance," *Journal of Lightwave Technology*, Vol. 34, pp. 5583-5590, 2016.
- [50] Cunningham, P. D., Valdes, M. N., Vallejo, F. A., Hayden, L. M., Polishak, B., Zhou, X., Luo, J., Jen, A. K. Y., Williams, J. C., and Twieg, R. J., "Broadband terahertz characterization of the refractive index and absorption of some important polymeric and organic electro-optic materials," *Journal of Applied Physics*, Vol. 109, 043505, 2011.
- [51] Markos, C., Kubat, I., and Bang, O., "Hybrid polymer photonic crystal fiber with integrated chalcogenide glass nanofilms," *Scientific Reports*, Vol. 4, pp. 1-7, 2014.
- [52] Baker, C., and Rochette, M., "Highly nonlinear hybrid AsSe-PMMA microtapers," *Optics Express*, Vol. 18, pp. 12391-12398, 2010.
- [53] Markos, C., Yannopoulos, S. N., and Vlachos, K., "Chalcogenide glass layers in silica photonic crystal fibers," *Optics Express*, Vol. 20, pp. 14814-14824, 2012.

- [54] Siegel, P., "Terahertz technology in biology and medicine," *IEEE Transactions on Microwave Theory and Techniques*, vol. 52, pp. 2438 – 2447, 2004.
- [55] Hoshina, H., Hayashi, A., Miyoshi, N., Miyamaru, F., and Otani, C., "Terahertz pulsed imaging of frozen biological tissues," *Applied Physics Letters*, vol. 94, no. 123901, 2009.
- [56] Han, H., Park, H., Cho, M. and Kim, J., "Terahertz pulse propagation in a plastic photonic crystal fiber," *Applied Physics Letter*, vol. 80, no. 15, pp. 2634-2636, 2002.
- [57] McGown, R. W., Gallot, G., and Grischkowsky, D., "Propagation of ultrawideband short pulses of terahertz radiation through submillimeter-diameter circular waveguides," *Optics Letter*, vol. 24, no. 20, pp. 1431-1433, 1999.
- [58] Mendis, R. and Grischkowsky, D., "Plastic ribbon THz waveguides," *J. Appl. Phys.*, vol. 88, no. 7, pp. 4449-4451, 2000.
- [59] Gallot, G., Jamison, S. P., McGowan, R. W., and Grischkowsky, D., "Terahertz waveguides," *J. Opt. Soc. Am. B*, vol. 17, no. 5, pp. 851-863, 2000.
- [60] Birks, T. A., Knight, J. C., and Rusell, P. J., "Endlessly Single-mode photonic crystal fiber," *Optics Letter*, vol.22, no. 13, pp. 961-963, 1997.
- [61] Chen, L. J., Chen, H. W., Kao, T. F., Lu, J. Y., and Sun, C. K., "Low-loss subwavelength plastic fiber for terahertz waveguiding," *Opt. Lett.*, vol. 31, no. 3, pp. 308-310, 2006.
- [62] Poli, F., Cucinotta, A., Selleri, S., and Bouk, A. H., "Tailoring of flattened dispersion in highly nonlinear photonic crystal fibers," *IEEE Photon. Technol. Lett.*, vol. 16, no. 4, pp. 1065-1067, 2004.
- [63] Eggleton, B., Kerbage, C., Westbrook, P., Windeler, R., and Hale, A., "Microstructured optical fiber devices," *Opt. Exp.*, vol. 9, no. 13, pp. 698-713, 2001.
- [64] Goto, M., Quema, A., Takahashi, H., Ono, S., and Sarukura, N., "Teflon photonic crystal fiber as terahertz waveguide," *Jpn. J. Appl. Phys.*, vol. 43, no. 2B, pp. L317-L319, 2004.
- [65] Nielsen, K., Rasmussen, H. K., Adam, A. J., Planken, P. C., Bang, O., and Jepsen, P. U., "Bendable, low-loss Topas fibers for the terahertz frequency range," *Opt. Exp.*, vol. 17, no. 10, pp. 8592-8601, 2009.
- [66] Nagel, M., Marchewka, A., and Kurz, H., "Low-index discontinuity terahertz waveguides," *Opt. Exp.*, vol. 14, no. 21, pp. 9944-9954, 2006.
- [67] Hassani, A., Dupuis, A., and Skorobogatiy, M., "Porous polymer fibers for low-loss Terahertz guiding," *Opt. Exp.*, vol. 16, no. 9, pp. 6340-6351, 2008.
- [68] Hassani, A., Dupuis, A., and Skorobogatiy, M., "Low loss porous terahertz fibers containing multiple subwavelength holes," *Appl. Phys. Lett.*, vol. 92, no. 7, pp. 071101-1-3, Feb. 2008.
- [69] Atakaramians, S., Afshar, S., Fischer, V. B. M., Abbott, D., and Monroe, T. M., "Porous fibers: a novel approach to low loss THz waveguides," *Opt. Exp.*, vol. 16, no. 12, pp. 8845-8854, 2008.

- [70] Uthman, M., Rahman, B. M. A., Kejalakshmy, N., Agrawal, A., and Grattan, K. T. V., "Design and characterization of low-loss porous-core photonic crystal fiber," *IEEE Photonics Journal*, vol. 4, no. 6, pp. 2315- 2325, Dec. 2012.
- [71] Eijkelenborg, M. A., Argyros, A., Barton, G., Bassett, I. M., Fellew, M., Henry, G., Issa, N. A., Large, M. C. J., Manos, S., Padden, W., Poladian, L., and Zagari, J., "Recent progress in microstructured polymer optical fibre fabrication and characterization," *Opt. Fiber Technol.*, vol. 9, no. 4, pp. 199-209, 2003.
- [72] Nakao, R., Kondo, A., and Koike, Y., "Fabrication of High Glass Transition Temperature Graded-Index Plastic Optical Fiber: Part 2 - Fiber Fabrication and Characterizations," *Journal of Lightwave Technology*, vol. 30, no. 7, pp. 969-973, 2012.
- [73] Geoff B., Martijn, A., Eijkelenborg, V., Henry, G., Maryanne, C. J., Large, and Zagari, J., "Fabrication of microstructured polymer optical fibers," *Optical Fiber Technology*, vol. 10, no. 4, pp. 325-335, 2004.
- [74] Zhang, Y., Li, K., Wang, L., Ren, L., Zhao, W., and Miao, R., "Casting performs for microstructured polymer optical fiber fabrication," *Optics Express*, vol. 12, no. 12, 2006.
- [75] Large, M. C. J., Blacket, D., Bunge, C. A., "Microstructured polymer optical fibers compared to conventional POF: Novel properties and Applications," *IEEE Sensors Journ.*, vol. 10, no. 7, pp. 1213-1217, 2010.
- [76] Koshiha, M., "Full-Vector Analysis of Photonic Crystal Fibers Using the Finite Element Method," *IEICE Trans. Electron*, vol. E85, no. 4, pp. 881-888, 2002.
- [77] Kim, S., Sik, C., and Lee, J., "Single-mode Condition and Dispersion of Terahertz Photonic Crystal Fiber," *Journal of the Optical Society of Korea*, vol. 11, no. 3, pp. 97-100, 2007.
- [78] Haxha, S., and Ademgil, H., "Novel Design of Photonic Crystal Fibers with Low Confinement Losses, Nearly Zero Ultra-Flatted Chromatic Dispersion, Negative Chromatic Dispersion and Improved Effective Mode Area," *Journal of Optics Communications*, vol. 281, no. 2, pp. 278-286, 2008.
- [79] Yulin, A. V., Skryabin, D. V., and Russell, P. S. J., "Four-wave mixing of linear waves and solitons in fibers with higher-order dispersion," *Opt. Lett.*, vol. 29, pp. 2411-2413, 2004.
- [80] Haxha, S., and Ademgil, H., "Ultrahigh-Birefringent Bending-Insensitive Nonlinear Photonic Crystal Fiber with Low Losses," *IEEE Journal of Quantum Electronics*, vol. 45, no. 4, 2009.
- [81] Saitoh, K., and Koshiha, M., "Highly nonlinear dispersion-flattened photonic crystal fibers for supercontinuum generation in a telecommunication window," *Opt. Exp.*, vol. 12, no. 10, pp. 2027- 2032, 2004.
- [82] Synder, A. W., and Love, J. D., *Optical Waveguide Theory*, Chapman and Hall, New York, 1983.

- [83] Nielsen, M. D., Mortensen, N. A., Albertsen, M., Folkenberg, J. R., Bjarklev, A., and Bonacinni, D., "Predicting macrobending loss for large-mode area photonic crystal fibers," *Optics Express*, vol. 12, no. 8, pp. 1775-1779, 2004.
- [84] Nielsen, M. D., Mortensen, N. A., Albertsen, M., Folkenberg, and K. P. Hansen, "Modal cut-off and the V- parameter in photonic crystal fibers," *Optics Letter*, vol. 28, pp. 1879-1881, 2003.
- [85] Hou, Y., Fan, F., Jiang, Z. W., Wang, X. H., and Chang, S. J., "Highly Birefringent polymer terahertz fiber with honeycomb cladding," *Optik*, vol. 124, pp. 3095-3098, 2013.
- [86] Khadri, D., Belhadj, W., Gamra, D., Malek, F. B., and Bouchriha, H., "On the Validity of the Effective Index Method for Long Period Grating Photonic Crystal Fibers," *Materials Sciences and Applications*, vol. 3, pp. 310-316, 2012.
- [87] Bing, Y. G., Guang, L. S., Yan, W. X., and Shuo, L., "High birefringence, low loss terahertz photonic crystal fibres with zero dispersion at 0.3 THz," *Chin. Phys. B*, vol. 20, no. 9, 2011.
- [88] Shu-Qin, L., Tie-Ying, G., Hong, F., Hong- Lei, L., and Shui-Sheng, J., "A New type of Terahertz Waveguides," *Chinese Physics Letter*, vol. 23, no. 1, 2006.
- [89] Bai, J. J., Li, J. N., Zhang, H., Fang, H., and Chang, S. J., "A porous terahertz fiber with randomly distributed air holes," *Appl. Phys. B*, vol. 103, no. 2, pp. 381-386, 2011.
- [90] Saitoh, K., and Koshiba, M., "Numerical Modeling of Photonic Crystal Fibers," *Journal of Lightwave Technology*, vol. 23, no. 11, 2005.
- [91] Kaijage, S. F., Ouyang, Z., and Jin, X., "Porous-Core Photonic Crystal Fiber for Low Loss Terahertz Guiding," *IEEE Photonics Technology Letters*, vol. 25, no. 15, pp. 1454-1457, 2013.
- [92] Ademgil, H., Haxha, S., and Malek, F. A., "Highly Nonlinear Bending-Insensitive Birefringent Photonic Crystal Fibers," *Engineering*, 2, pp. 608-616, 2010.
- [93] Shou-zhong, H., Shang-lin, H., Yan-jun, L., Dao-bin, W., and Jing-li, L., "Propagation Characteristics of Terahertz Wave Double-cladding Photonic Crystal Fiber," *Chinese Journal of Luminescence*, vol. 37, no. 7, pp. 845-850, 2016.
- [94] Islam, R., Rana, S., Ahmed, R., and Kaijage, S. F., "Bend-Insensitive and Low-loss Porous Core Spiral Terahertz Fiber," *IEEE Photonics Tech. Letters*, vol. 27, no. 21, pp. 2242-2245, 2015.
- [95] Himeno, k., Matsuo, s., and Guan, N., "Low-Bending-Loss Single-Mode Fibers for Fiber-to-the-Home," *Journal of Lightwave Tech.*, vol. 23, no. 11, pp. 3494-3499, 2005.
- [96] Dudley, J. M., and Taylor, J. R., *Supercontinuum Generation in Photonic Crystal Fibers*, Cambridge University Press, New York, 2010.
- [97] Xiao-Yan, W., Shu-Guang, L., Shuo, L., Guo-Bing, Y., and Jian-She, L., "Generation of a mid-infrared broadband polarized supercontinuum in  $As_2Se_3$  photonic crystal fibers," *Chin. Phys. B*, vol. 21, no. 5, 2012.

- [98] Stone, J. M., and Knight, J.C., “From zero dispersion to group index matching: How tapering fibers offers the best of both worlds for visible supercontinuum generation,” *Optical Fiber Technology*, vol. 18, no. 5, pp. 315-321, Sep. 2012.
- [99] Jin-Hui, Y., Xin-Zhu, S., Chong-Xiu, Y., Xiang-Jun, X., Xiang-Wei, S., Jin-Long, Z., Gui-Yao, Z., Shu-Guang, L., and Lan-Tian, H., “Broad and ultra-flattened supercontinuum generation in the visible wavelengths based on the fundamental mode of photonic crystal fibre with central holes,” *Chin. Phys. B*, vol. 20, no. 5, 2011.
- [100] Er-Ming, P., Shuang-Chen, R., Chun-Yu, G., Yun-Cai, W., and Hui-Feng, W., “Supercontinuum Generation with Output Power of 1.7 W Pumped by a Picosecond Laser Pulse,” *Chinese Physics Letter*, vol. 27, no. 10, 2010.
- [101] Takara, H., “More than 1000 channel Optical frequency chain generation from single supercontinuum source with 12.5 GHz channel spacing,” *Electron letter*, vol. 36, no. 25, pp. 2089-2090, 2000.
- [102] Colman, P., Husko, C., Combrie, S., Sagnes, I., Wong, C.W., and Rossi, A. D., “Temporal solitons and pulse compression in photonic crystal waveguides,” *Nature Photonics*, vol. 4, pp. 862-868, 2010.
- [103] Travers, J. C., “Blue extension of optical fibre supercontinuum generation,” *Journal of Optics*, vol. 12, no. 11, 2010.
- [104] Travers, J. C., Taylor, J. R., “Soliton trapping of dispersive waves in tapered optical fibers,” *Optics Letter*, vol. 34, no. 2, pp. 115-117, 2009.
- [105] Mussot, A., Kudlinski, A., Kolobov, M., Louvergnaux, E., Douay, M., Taki, M., “Observation of extreme temporal events in CW-pumped supercontinuum,” *Optics Express*, vol. 17, no. 19, pp. 17010-17015, 2009.
- [106] Dudley, J. M., and Coen, S., “Coherence properties of supercontinuum spectra generated in photonic crystal and tapered optical fibers,” *Optics Letter*, vol. 27, no. 13, pp. 1180-1182, 2002.
- [107] Rios, A. M., Boaz, I., Gómez, I. T., D. Hernandez, M., and Herrera, D. E. C., “Calculation of higher order dispersion coefficients in photonic crystal fibers,” *Proc. of SPIE*, vol. 8011, 2011.
- [108] Maveeran, M., Alagesan, T., Babu, P. R., and Senthilnathan, K., “Supercontinuum generation in low dispersion and highly nonlinear hexagonal photonic crystal fibers,” *Journal of Nanophotonics*, vol. 11, no. 3, 2017.
- [109] Bache, M., “Designing microstructured polymer optical fibers for cascaded quadratic soliton compression of femtosecond pulses,” *J. Opt. Soc. Am. B*, vol. 26, pp. 460-470, 2009.